

**Enhancement in compressive properties of
additive-manufactured metallic lattice structures
through experimental and numerical approaches**

2021

Liu Xiaoyang

Contents

1. Introduction	1
1.1 Background	1
1.2 Cellular structures	1
<i>1.2.1 Designs of unit cell</i>	2
<i>1.2.2 Fabrication of metallic lattice structure</i>	5
<i>1.2.3 Mechanical property</i>	6
1.3 Literature review	8
1.4 Objectives	13
References	13
2. Effect of unit cell type on compressive behavior of lattice structures	21
2.1 Introduction	21
2.2 Materials and methods	22
<i>2.2.1 Manufacture of lattice structures by L-PBF</i>	22
<i>2.2.2 Designs of lattice structure</i>	23
<i>2.2.3 Measurements</i>	23
<i>2.2.4 Finite element method</i>	26
2.3 Results	28
<i>2.3.1 Mechanical property</i>	28
<i>2.3.2 Deformation behavior</i>	30
<i>2.3.3 Static and high-speed indentation test</i>	32
2.4 Discussion	35
<i>2.4.1 Compressive behavior</i>	35
<i>2.4.2 Energy absorption capacity</i>	39
2.5 Conclusions	41
References	41

3. Understanding and suppressing shear band formation	45
3.1 Introduction	45
3.2 Materials and methods	47
3.2.1 <i>Design and manufacturing</i>	47
3.2.2 <i>Mechanical tests and tomography</i>	50
3.2.3 <i>FEM analysis</i>	51
3.3 Results and discussion	52
3.3.1 <i>Formation process of shear band</i>	52
3.3.2 <i>Preferential formation plane and direction of shear band</i>	57
3.3.3 <i>Suppression of shear band formation</i>	62
3.4 Conclusions	74
References	75
4. Lattice structures inspired by crystal structures	79
4.1 Introduction	79
4.2 Materials and methods	80
4.3 Results and discussion	83
4.4 Conclusions	94
References	94
5. Hybrid lattice structures composed of different unit cells	97
5.1 Introduction	97
5.2 Materials and methods	98
5.3 Results and discussion	100
5.4 Conclusions	114
References	115
6. Conclusions and future work	117
6.1 Conclusions	117

6.2 Future work	119
Published journal papers	122
Acknowledgements	123

1. Introduction

1.1 Background

Nowadays, the global consensus on establishing low-carbon economy and society has been made for climate change mitigation. To meet the requirement for sustainable development, the strategies of less material usage, appropriate material choice, and less energy consumption are being promoted. The weights of many current industrial products can be significantly reduced without sacrificing the safety or performance attributes [1]. Therefore, lightweight structures should be optimally and extensively used in engineering and industrial applications. As a typical category of the lightweight structures, cellular materials have attracted considerable interests due to their beneficial properties such as high strength/stiffness-to-weight ratio, excellent energy-absorbing capacity, strong thermal insulation, and superior sound proofing characteristics [2]. Recent advances in additive manufacturing (AM) techniques enable the production of cellular structures with complex geometries, controlled precision, and efficient material use, which offer enormous potential for ultra-light cellular structures utilized in a broad array of applications [3].

1.2 Cellular structures

In nature, cellular structures consisting of continuous solids and voids abundantly exist. Such materials with a porosity are observed (**Fig. 1-1**) in woods [4], honeycombs [5], cork [6], dragonfly wing [7], trabecular bone [8], deep sea sponge [9] and many other organisms. These natural cellular structures possess delicate balance between weight and strength, and provide extensive references of configurations in cellular structures for engineering designers. Basically, human-made cellular structures with diverse topologies are categorized into two main types: stochastic foams and periodic lattice (repeating architected unit cells) [10, 11] (**Fig. 1-2**). Stochastic foams with random distribution of pores are typically divided into open-cell and close-cell structures. These structures are lack in reproducibility and precision due to the difficulty in controlling pore morphology during the fabrication process of stochastic foams. In contrast, periodic lattice structures compose of repetitive arrangement of unit cells, including strut-based, skeletal-based, and sheet/shell-based types depending on different components of unit cell. Various types of unit cells enable many possibilities of structure–property relationships

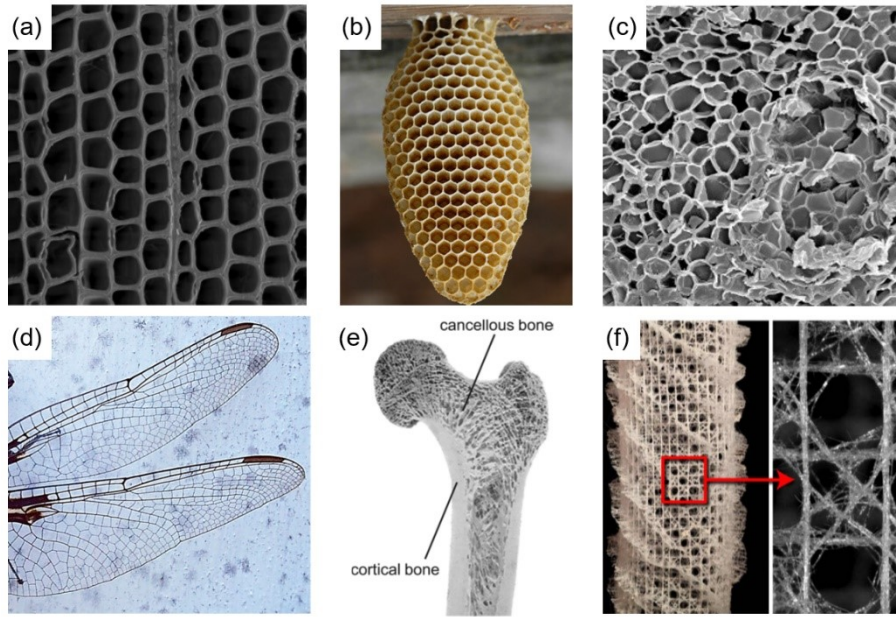


Fig. 1-1 Examples of natural cellular structures. (a) woods [4], (b) honeycombs [5], (c) cork [6], (d) dragonfly wing [7], (e) trabecular bone [8], and (f) deep sea sponge [9]

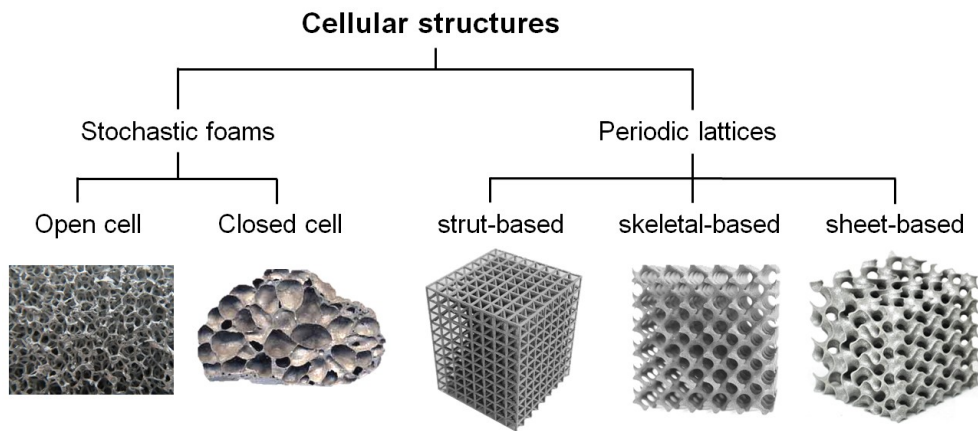


Fig. 1-2 Human-made cellular structures divided into stochastic foams and periodic lattice [10, 11].

of lattice structures.

1.2.1 Designs of unit cell

For strut-based lattice structures, the nodes and struts of unit cells are observed to be analogous to the atom and atomic bond in metallurgical crystal structures. Many lattice structures are designed by imitating crystal structures, for instance, the most common

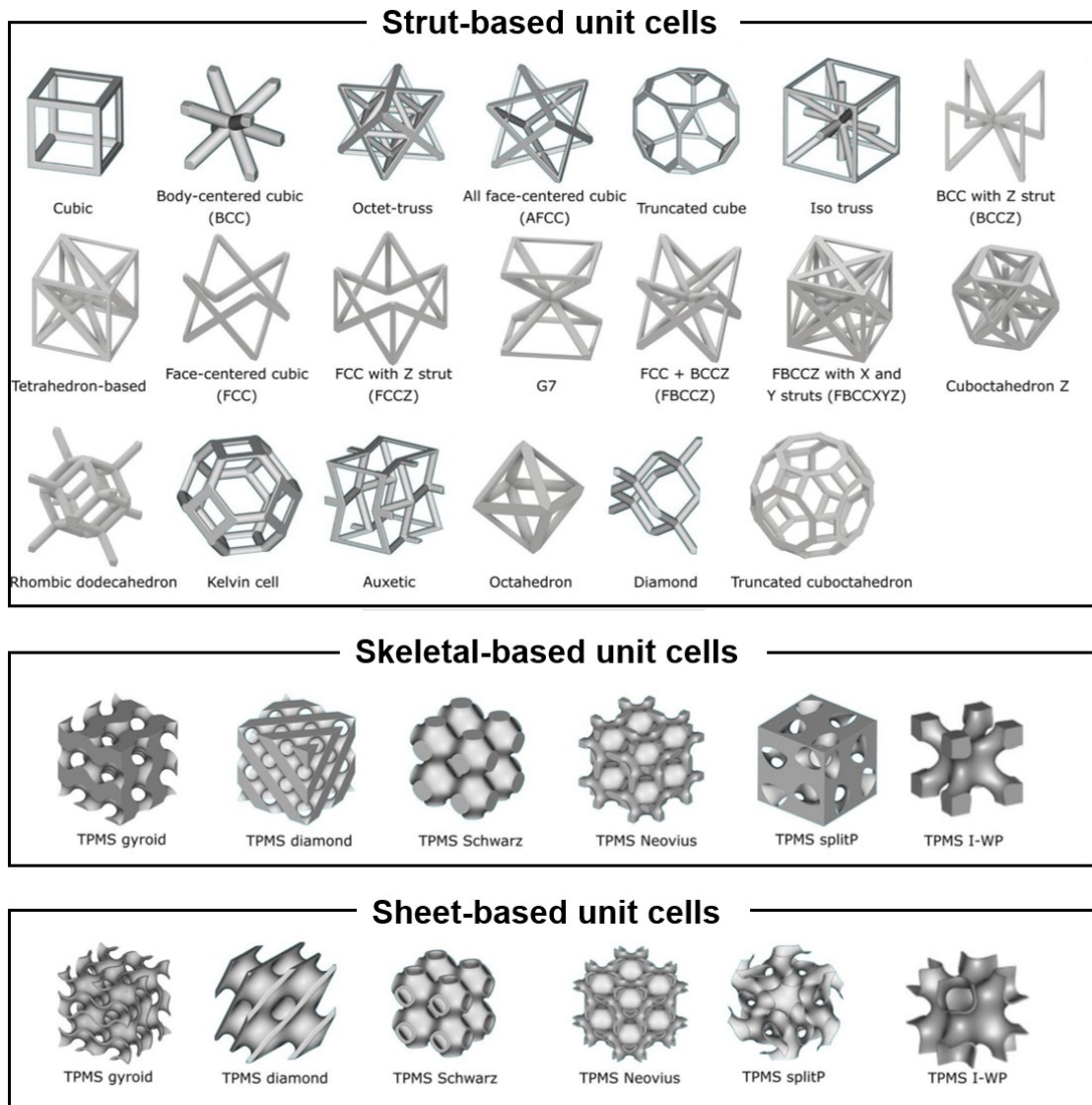


Fig. 1-3 Examples of strut-based, skeletal-based, and sheet-based unit cells [12].

body-centered cubic (BCC), face-centered cubic (FCC), diamond along with their combinations and variations (addition or subtraction of struts). Others from the comprehensive unit cell library such as cubic, octet-truss, rhombic dodecahedron (RD) and truncated octahedron are often found in literatures (**Fig. 1-3**) [12].

Maxwell established a stability criterion using algebraic rule for a three-dimensional frame made up of s struts and n nodes [13], the Maxwell number is,

$$M = s - 3n + 6 \tag{1.1}$$

The deformation behavior of strut-based lattice structures can be roughly predicted according to

the Maxwell stability criterion. As shown in **Fig. 1-4** [14, 15], if $M < 0$, the bending of struts dominantly contributes to the deformation of lattice structures, which is called the bending-dominated behavior, because the nodes in lattice unit cells are constrained or locked and insufficient struts equilibrate bending moments at nodes. If $M = 0$, the struts support tension and compression to equilibrate external load. The deformation behavior of the just-stiff structure becomes stretch-dominated. If $M > 0$, the structure exhibits over-stiff stretch-dominated behavior. Although Maxwell's stability criterion is limited to the strut-based lattice structures under specific loading direction, its simplicity contributes to the design consideration by quickly categorizing the basic deformation mode of bending- or stretch-dominated behavior.

The unit cells of skeletal- and sheet-based lattice structures are derived from the triply periodic minimal surfaces (TPMS) (**Fig. 1-3**), which are created using mathematical formulae. An example of level-set approximation function for TPMS is expressed as

$$\sin x \cos y + \sin y \cos z + \sin z \cos x = t \quad (1.2)$$

where the variable t is the level set constant to control relative density. MSLattice software as a design platform can conveniently create skeletal- and sheet-based lattice structures based on TPMS, from the aspects of types, relative density, cell size, hybrid and gradation [16]. Simple sheet-based lattice structures without curvature arranged along the closest-packed planes of cubic crystal structures are also found in reported study [17].

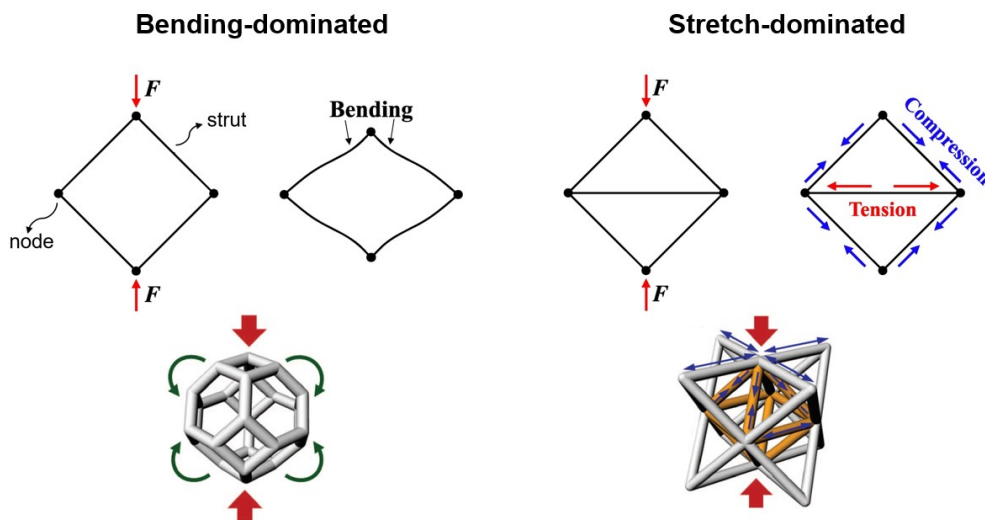


Fig. 1-4 Illustration showing bending- ($M < 0$) and stretch- ($M \geq 0$) dominated structures [14, 15].

Topology optimization is a powerful computational design tool to create optimal lattice structures, which seeks the best distribution of solids and voids that exhibits prescribed properties under given constraints. Lattice structures exhibiting maximum bulk modulus, maximum isotropic thermal conductivity, and negative Poisson's ratio have been designed using the topology optimization. The unit cells of optimized lattice structures normally consist of curved struts or sheets [18, 19].

1.2.2 Fabrication of metallic lattice structure

Metallic lattice structures can be manufactured through many kinds of methods, generally divided into two: conventional machining processes and additive manufacturing. There are four main conventional processing methods, including investment casting, deformation forming, water jet cutting, metallic wire assembly, snap fit method [2]. Compared to additive manufacturing, these conventional machining processes can effectively fabricate large-scale lattice structures. However, there are many disadvantages and limitations when conventional processes applied. For example, casting defects often forms in lattice structures by investment casting method due to the high requirements for the fluidity of liquid metal [20]. The major drawback of conventional processes is the difficulty in manufacturing the lattice structures with high-level complexity and small-scale unit cells. Additionally, it might be impossible to produce skeletal- and sheet-based lattice structure through the conventional processing methods.

Rapid development of additive manufacturing techniques significantly improves product manufacturability and promotes design creativity, representing a breakthrough for lattice structures with highly complex shape for many functionalities. Laser powder bed fusion (L-PBF) is a common metal additive manufacturing which has been widely used. The system of L-PBF manufacturing machine consists of vacuum chamber, powder dispensing apparatus, laser beam, and powder bed preheating system. In the L-PBF process, metal raw powder is bedded in thin layers (layer thickness $< 100 \mu\text{m}$) on a building platform, which is filled with inert gas like argon to avoid oxidation. The layer of the powder is melted and fused by laser irradiation following the exact geometry of computer-generated 3D pattern. The same process is applied repetitively to all the layers of the component until the completion of fabrication. The L-PBF manufacturing process has been utilized for many metal products, such as aluminum alloy, titanium alloy, copper alloy, and stainless steel. It is reported that lattice structure samples

manufactured by L-PBF exhibited good building quality with high relative density ($> 97\%$) at node and strut [21]. Without the limitation of geometry, lattice structures with abundant unit cell topologies are L-PBF manufactured and their mechanical performances are investigated [22]. The L-PBF manufacturing process has disadvantages and limits. Heat-treatment may need to be applied to improve the ductility, owing to the residual stress generated by rapid cooling during manufacturing process. Post surface-treatment may be also required for the removal of un-melted powder attached. L-PBF processing parameters applied for different raw materials should be respectively optimized for the best building quality with high relative density and less internal voids. These kind of drawbacks of L-PBF processing motivate many related investigations to address the problems.

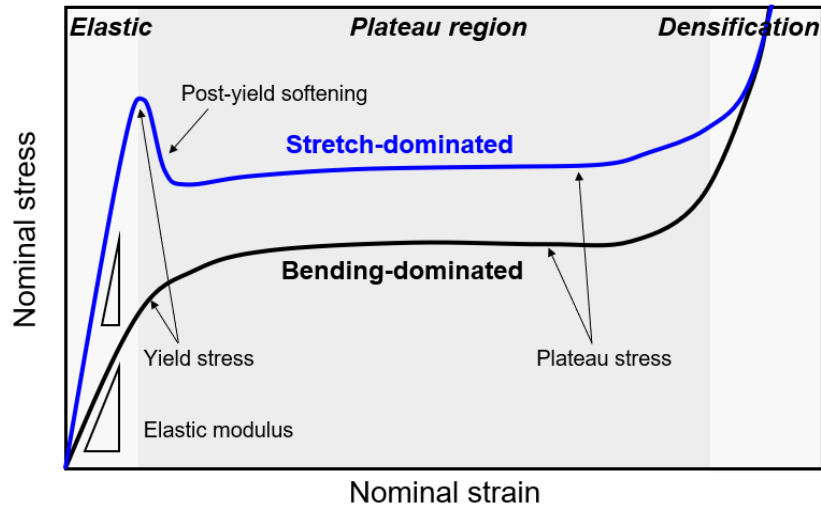


Fig. 1-5 Compressive stress–strain responses of bending-dominated and stretch-dominated lattice structures [20, 22].

1.2.3 Mechanical property

The mechanical responses of lattice structures mainly depend on the properties of the raw material, unit cell topology and relative density [23]. **Figure 1-5** presents the examples of compressive stress–strain response of lattice structures with bending- and stretch-dominated deformation mechanism. It is evident that the deformation behaviors are divided into three distinct stages. Firstly, the lattice structure initially exhibits linear elastic deformation. A plateau region of nearly constant stress emerges after the yield point, as the structure undergoes

non-recoverable plastic or brittle deformation behavior (depending on the ductility of material used). For stretch-dominated lattice structure, a post-yield softening often occur due to fractured or buckled struts. While bending-dominated lattice structure typically exhibits a moderate deformation behavior with bended struts. Finally, the structure enters the densification stage with rapidly increased stress when enough deformed struts contact with each other. Due to the difference of deformation behavior, the elastic modulus and yield strength of stretch-dominated structure are normally greater than those of bending-dominated structure when the relative densities are kept constant, indicating that the former used as lightweight load-carrying component is more weight-efficient and favorable. The existence of long plateau region makes lattice structure desirable for the applications of energy absorber, whose capacity is estimated by integrating the stress–strain curve before densification. The equation showing the absorbed energy per unit volume (W) is given as follows.

$$W = \int_0^{\varepsilon_{den}^*} \sigma^* d\varepsilon^* \quad (1.3)$$

where, σ^* is nominal stress, ε^* is nominal strain, and ε_{den}^* is the initial strain for densification.

To estimate the dependency between the relative densities and the mechanical property of cellular structure, a notable and commonly accepted theoretical model was established by Ashby and Gibson [24]. As expressed in **Eq. (1.3)** and **(1.4)**, the relative elastic modulus E^*/E_s and relative yield strength σ_y^*/σ_s of cellular structures have a positive power law relationship with the relative density ρ^*/ρ_s . Here, E^* and E_s are the elastic modulus of cellular and dense materials, and σ_y^* and σ_s are the yield strength of cellular and dense materials, respectively.

$$\frac{E^*}{E} = C \left(\frac{\rho^*}{\rho_s} \right)^n \quad (1.4)$$

$$\frac{\sigma_y^*}{\sigma_s} = C \left(\frac{\rho^*}{\rho_s} \right)^n \quad (1.5)$$

where C and n are coefficient and exponent derived from experimental results, respectively. The exponent n values for modulus and strength as summarized in **Table 1-1** depend on the stretch- or bending-dominated deformation behavior of lattice structure. Based on extensive experimental and analytical data of metallic cellular structures, the coefficients C are roughly

within the range of 0.1~4.0 and 0.1~1.0 for E^*/E_s and σ^*/σ_s , respectively [25]. Therefore, the Gibson-Ashby plots are often used for the comparison between the predicted and tested results. Some researches focus on reducing the value of exponent for the structure efficiency in a wide range of density [15].

Table 1-1 Exponent value of Ashby and Gibson model for lattice structure with different deformation pattern.

Deformation pattern	Mechanical property	n value
Bending-dominated	Modulus (E)	2
	strength (σ)	1.5
Stretch-dominated	Modulus (E)	1
	strength (σ)	1

1.3 Literature review

The investigations on the AM fabricated lattice structures have been extensively conducted, mainly focusing on the mechanical properties, deformation behaviors and designs. This section is aimed to review the reported literatures for better understanding of state-of-art researches and current issues of lattice structure.

The mechanical performances of lattice structure are generally evaluated by tensile, fatigue, bending, static and dynamic compressive tests. Compression tests are most commonly carried out due to their simplicity and practical load-carrying condition of lattice structures. Cao et al. [26] presented an investigation on the quasi-static and dynamic mechanical property of RD stainless steel lattice structures. The experimental and numerical results indicated that the strength, plateau stress and specific energy absorption were enhanced with the increase of strain rate. Another stainless steel lattice structure with octet truss units was found to exhibit the dependence between strength and strain rate [27]. The study by Xiao et al. [28] suggested that the yield stress of RD Ti6Al4V lattice structures exhibited hardly strain rate sensitivity for 5 mm cell, but certain sensitivity for 3 mm cell. Therefore, the strain rate sensitivity for mechanical properties of lattice structure may relate to the base material, and further investigation on the unit cell dependence is also needed. For the mechanical properties obtained from the stress–

strain responses of static compression tests, the elastic modulus and compressive (yield) strength of lattice structures were evaluated from many aspects, such as load orientation [29], boundary condition [30], layer, type and size variety of unit cell [31-33]. The compressive strength, normally determined by initial peak stress or yield stress, is relevant to the stress level the plateau region and critical for the energy-absorbing capacity of lattice structure. Based on the reported metallic lattice structures with different unit cells made of common copper alloy

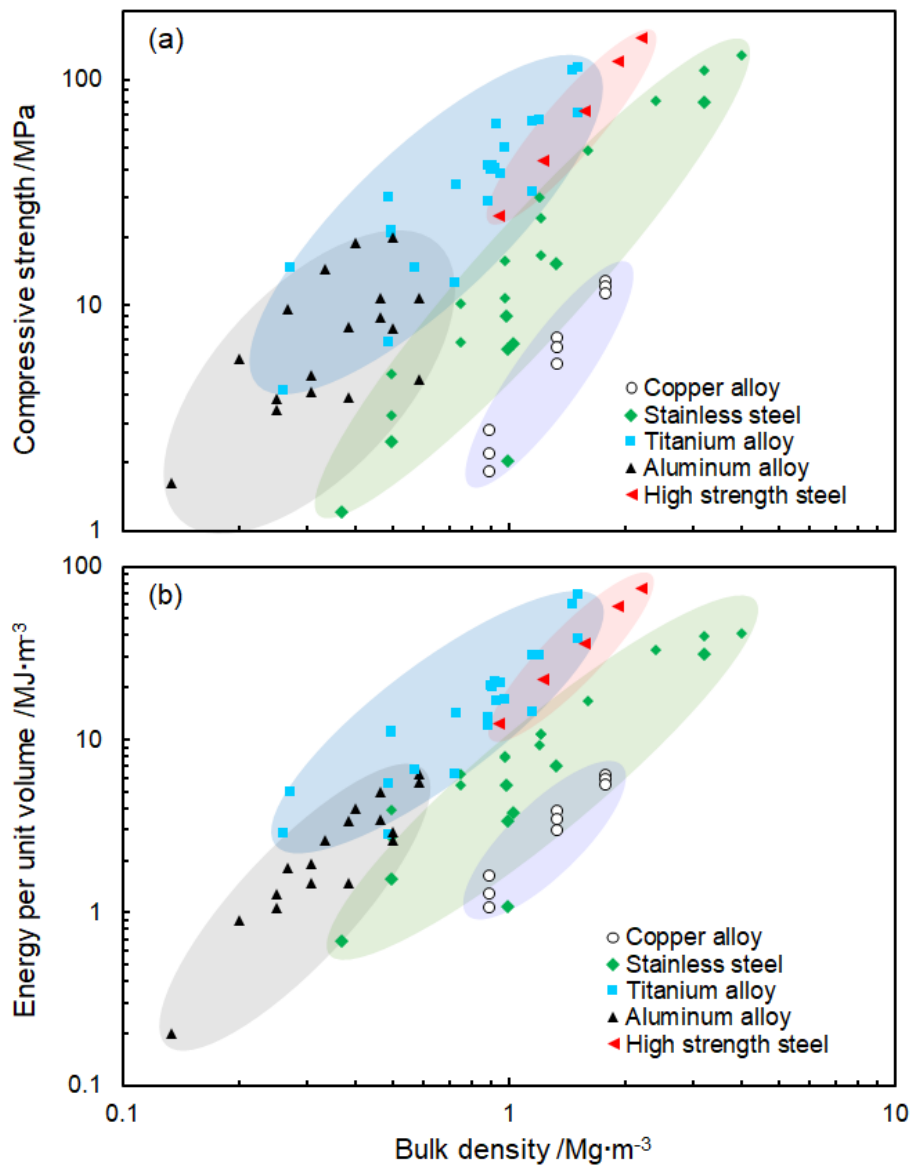


Fig. 1-6 The changes in (a) compressive strength and (b) energy per unit volume as a function of bulk density of metallic lattice structures made of common copper alloy, stainless steel, titanium alloy, aluminum alloy, and high strength steel, as reported in literatures.

[34], stainless steel [35-38], titanium alloy [39-42], aluminum alloy [43-46], and high strength steel [47], the changes in yield strength and energy absorption capacity as a function of bulk density are plotted in **Fig. 1-6**. The compressive strength and energy per unit volume exhibiting similar trends against bulk density reveal their close dependence. The high-strength metal materials used or large density of lattice structure generally result in high energy absorption capacity. The overlapping ranges existing in the plots suggest that the lattice structures made of low-strength materials can also reach the capacity in the range of higher strength material. In other words, the mechanical properties are not only dependent on base materials, but also strongly related to unit cell types. Therefore, the methods, such as appropriately selected type and modification of unit cell, to optimize the mechanical properties of lattice structures with high energy absorption capacity and less material usage need to be explored. In addition, the aluminum alloy lattice structures exhibit the relatively dispersed compressive strength compared to energy absorption capacity. It indicates that the compressive strength of aluminum alloy lattice structures is more sensitive to the unit cell types. However, the systematic investigations on the relationships between unit cell types and mechanical properties of aluminum alloy lattice structure are still insufficient. Especially, the influences of unit cell types on the plateau region (related to strength, deformation and densification behavior) determining the energy absorption capacity should be investigated.

The deformation behavior and failure mode of lattice structures are extensively researched to understand and idealize the mechanism for high-stress and flat plateau. Carlton et al. [48] experimentally and numerically evaluated the local strain and deformation behavior of different unit cells in metal lattice structures. The predictive continuum model indicated failure behavior evolved from buckling to yielding for stretch-dominated octet lattice structure with a relative density range of 10-20%. Koehnen et al. [49] reported that $f2cc,z$ lattice structures exhibited stretching deformation behavior with higher elastic modulus, compressive strength and absorbed energy in comparison to bending-dominated hollow spherical lattice structures. Amani et al. [50] investigated the deformation behavior of FCC lattice structures using in- and ex-situ X-ray tomography, which indicated that the progressive fracture was related to the initial morphologic features. Liu et al. [51] presented a parametric investigation on the dependence between geometry imperfection and compressive behaviors of lattice structures. The elastic modulus and compressive strength were largely deteriorated by the imperfections, and a

transition in deformation mode from diagonal shear failure to horizontal crushing was characterized in octet lattice structures when horizontal struts were oversized. Li et al. [52] explored the deformation process of BCC lattice structures using finite element method (FEM). The plastic stress distributed around nodes formed plastic hinges in unit cells, whereas central region of struts exhibited elastic behavior. The result also revealed that the structure densification was attributed to self-contact interaction of struts. For the BCC-Z lattice structures with the struts along loading direction, the localized buckling of the vertical struts led to the occurrence of a diagonal 45° shear band [53, 54]. The formation of shear band, which could lead to stress fluctuation and deterioration of energy absorption capacity, is commonly found in the deformation behavior of various lattice structures [28, 55-57]. As the test appearance and captured X-ray tomography cross-section of compressed lattice structure shown in **Fig. 1-7** [56], a shear band is developed as a result of highly localized deformation on specific planes with defined directions. Although many studies have focused on the formation mechanism, the formation process and preferential plane and direction of shear band in lattice structures are still not well understood. Moreover, effective methods to suppress the shear band formation need to be explored.

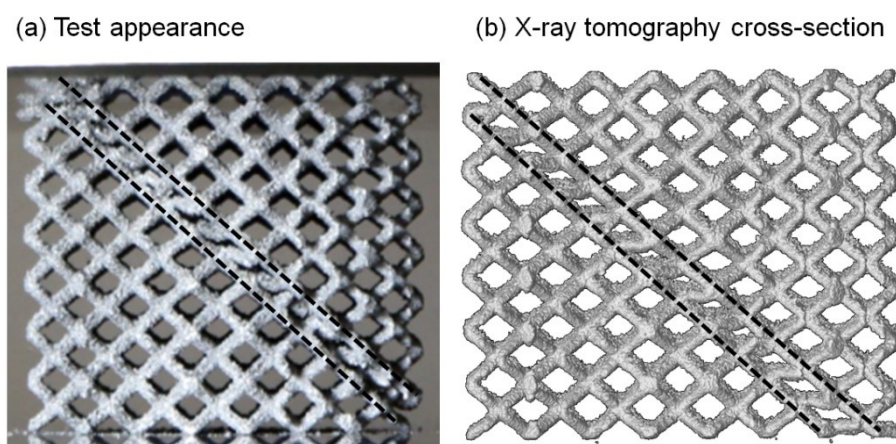


Fig. 1-7 (a) Test appearance and (b) X-ray tomography cross-section showing shear band formation in lattice structure [56].

The studies related to the unit cell design are active and extensive, since comprehensive understanding and desirable properties of lattice structure are often explored by varying the unit cells. For instance, suppression of shear band formation may be achieved by modifying the topology of unit cell or strut. Mazur et al. [40] investigated the mechanical and deformation

behavior of SLM Ti-6Al-4V lattice structures with different type, size, and number of unit cells. A design method considering tight spatial arrangement and manufacturing constraint was proposed by Li et al. [58] to elucidate the effect of node freedom degree on compressive property and energy absorption capacity of lattice structures. Zhou et al. [59] designed self-supporting lattice structures based on multi-fold symmetry operation, which enable the gradual transition from bending-dominated to stretching-dominated behavior. Truss lattice structures exhibiting isotropic elasticity were explored by the topology constraints through combining simple cubic (SC), BCC and FCC unit cells [60]. Modification of struts in lattice unit cells was also adopted in reported studies for improvement of mechanical property. Qi et al. [61] carried out node enforcement by tapering the struts of octet lattice structure, the modulus and isotropy were therefore increased. Similar study on strut modification of RD lattice structure with shape parameters revealed higher energy-absorbing capacity [37]. Anisotropy from the point of view of macro-mechanical property is a common behavior for lattice structure. Cutolo et al. [62] suggested that the unit cell orientation of Ti6Al4V diamond lattice structure significantly affected its mechanical property and failure behavior. Gyroid lattice structures with superior mechanical behavior also exhibited anisotropy of elastic modulus under different load orientations [63]. Another type sheet-based lattice structure exhibited high stiffness and strength reaching upper bound of Hashin-Shtrikman model [15, 64]. The method of topology

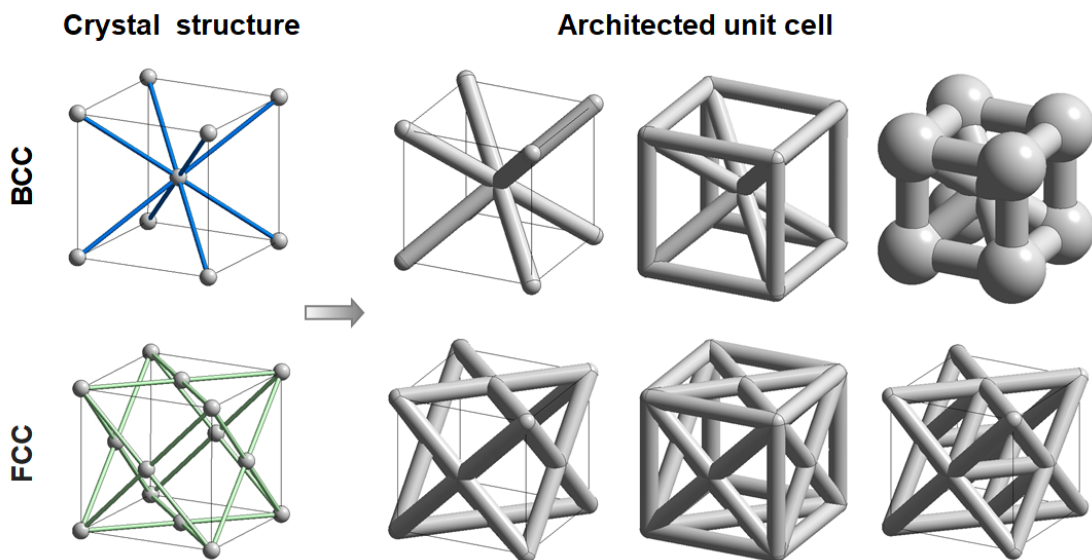


Fig. 1-8 Various reported designs of architected unit cells based on BCC and FCC crystal structure.

optimization is applied to design lattice structures with maximized the bulk or shear modulus, isotropy [65], anisotropy [66], and desired Poisson's ratio [67]. Designs of strut-based lattice structures by imitating crystal structures are also reported [68-71], but those are normally limited to the inspiration from simple BCC and FCC crystal structures as shown in **Fig. 1-8**. More possibilities of unique properties beneficial from creative designs should be explored for lattice structures, for instance, imitating complex crystal structures and combination of different unit cell types.

1.4 Objectives

The purpose of the present study is to understand the mechanical properties and deformation behaviors of metallic lattice structure produced by L-PBF, and to develop desirable lattice structures with high strength, stability and energy absorption for wide industrial applications. In order to achieve this, the following main objectives have been defined:

1. Investigate the effect of unit cell types on the mechanical property and deformation behavior of lattice structure (Chapter 2);
2. Understand the mechanism, process and preferential plane and direction of shear band formation, and propose effective method to suppress the shear band formation (Chapter 3);
3. Develop new lattice structures with high energy absorption and unprecedented properties by imitating crystal structures (Chapter 4);
4. Develop hybrid lattice structures with the combination of bending-dominated and stretch-dominated unit cells to enhance the mechanical performance (Chapter 5).

References

- [1] A. Bandivadekar, K. Bodek, L. Cheah, C. Evans, T. Groode, J. Heywood, E. Kasseris, M. Kromer, M. Weiss, On the Road in 2035: Reducing Transportation's Petroleum Consumption and GHG Emissions. Massachusetts Institute of Technology (2008), Report No. LFEE 2008-05 RP.
- [2] M.G. Rashed, M. Ashraf, R.A.W. Mines, P.J. Hazell, Metallic microlattice materials: A current state of the art on manufacturing, mechanical properties and applications, *Mater. Des.* 95 (2016) 518–533.
- [3] T. D. Ngo, A. Kashani, G. Imbalzano, K. T. Nguyen, D. Hui, Additive manufacturing (3D

- printing): A review of materials, methods, applications and challenges, *Compos. B. Eng.* 143 (2018) 172–196.
- [4] P. Perré, G. Almeida, M. Ayouz, X. Frank, New modelling approaches to predict wood properties from its cellular structure: image-based representation and meshless methods, *Ann. For. Sci.* 73 (1) (2016) 147–162.
- [5] <https://americanbeejournal.com/comb-building-watch-out-for-wrong-turns/>.
- [6] G.S. Mota, C.J. Sartori, J. Ferreira, I. Miranda, T. Quilhó, F.A. Mori, H. Pereira, Cellular structure and chemical composition of cork from *Plathymenia reticulata* occurring in the Brazilian Cerrado, *Ind. Crops. Prod.* 90 (2016) 65–75.
- [7] D. Bhate, C.A. Penick, L.A. Ferry, C. Lee, Classification and selection of cellular materials in mechanical design: Engineering and biomimetic approaches, *Designs* 3 (1) (2019) 19.
- [8] N.M. Willems, G.E. Langenbach, V. Everts, A. Zentner, The microstructural and biomechanical development of the condylar bone: a review, *Eur. J. Orthod.* 36 (4) (2014) 479–485.
- [9] M.C. Fernandes, J. Aizenberg, J.C. Weaver, K. Bertoldi, Mechanically robust lattices inspired by deep-sea glass sponges, *Nat. Mater.* 20 (2) (2021) 237–241.
- [10] O. Al-Ketan, D.W. Lee, R. Rowshan, R.K.A. Al-Rub, Functionally graded and multi-morphology sheet TPMS lattices: Design, manufacturing, and mechanical properties, *J. Mech. Behav. Biomed. Mater.* 102 (2020) 103520.
- [11] A.M. Abou-Ali, O. Al-Ketan, R. Rowshan, R.A. Al-Rub, Mechanical response of 3D printed bending-dominated ligament-based triply periodic cellular polymeric solids, *J. Mater. Eng. Perform.* 28 (4) (2019) 2316–2326.
- [12] M. Benedetti, A. Du Plessis, R. O. Ritchie, M. Dallago, S.M.J. Razavi, F. Berto, Architected cellular materials: A review on their mechanical properties towards fatigue-tolerant design and fabrication, *Mater. Sci. Eng. R Rep.* 144 (2021) 100606.
- [13] J.C. Maxwell, L. on the calculation of the equilibrium and stiffness of frames, *Philos. Mag.* 27 (182) (1864) 294.
- [14] D. Kang, S. Park, Y. Son, S. Yeon, S.H. Kim, I. Kim, Multi-lattice inner structures for high-strength and light-weight in metal selective laser melting process, *Mater. Des.* 175 (2019) 107786.
- [15] X. Zheng, H. Lee, T.H. Weisgraber, M. Shusteff, J. DeOtte, E.B. Duoss, J.D. Kuntz, M.M.

- Biener, Q. Ge, J.A. Jackson, S.O. Kucheyev, N.X. Fang, C.M. Spadaccini, Ultralight, ultrastiff mechanical metamaterials, *Science* 344 (6190) (2014) 1373–1377.
- [16] O. Al-Ketan, R.K. Abu Al-Rub, MSLattice: A free software for generating uniform and graded lattices based on triply periodic minimal surfaces, *Mater. Des. Process. Commun.* (2020) e205.
- [17] T. Tancogne-Dejean, M. Diamantopoulou, M.B. Gorji, C. Bonatti, D. Mohr, 3D Plate-Lattices: An Emerging Class of Low-Density Metamaterial Exhibiting Optimal Isotropic Stiffness, *Adv. Mater.* 30 (45) (2018) 1803334.
- [18] A. Takezawa, K. Yonekura, Y. Koizumi, X. Zhang, M. Kitamura, Isotropic Ti–6Al–4V lattice via topology optimization and electron-beam melting, *Addit. Manuf.* 22 (2018) 634–642.
- [19] C. Yang, P. Xu, S. Xie, S. Yao, Mechanical performances of four lattice materials guided by topology optimization, *Scr. Mater.* 178 (2020) 339–345.
- [20] V.S. Deshpande, M.F. Ashby, N.A. Fleck, Foam topology: Bending versus stretching dominated architectures, *Acta Mater.* 49 (2001) 1035–1040.
- [21] M. Liu, N. Takata, A. Suzuki, M. Kobashi, Development of gradient microstructure in the lattice structure of AlSi10Mg alloy fabricated by selective laser melting, *J. Mater. Sci. Tech.* 36 (2020) 106–117.
- [22] B. Hanks, J. Berthel, M. Frecker, T.W. Simpson, Mechanical properties of additively manufactured metal lattice structures: data review and design interface, *Addit. Manuf.* 35 (2020) 101301.
- [23] M.F. Ashby, The properties of foams and lattices, *Philos. Transact. A Math. Phys. Eng. Sci.* 364 (2006) 15–30.
- [24] M.F. Ashby, Hybrids to fill holes in material property space, *Philos. Mag.* 85(26-27) (2005) 3235–3257.
- [25] T. Maconachie, M. Leary, B. Lozanovski, X. Zhang, M. Qian, O. Faruque, M. Brandt, SLM lattice structures: Properties, performance, applications and challenges. *Mater. Des.* 183 (2019) 108137.
- [26] X. Cao, D. Xiao, Y. Li, W. Wen, T. Zhao, Z. Chen, Y. Jiang, D. Fang, Dynamic compressive behavior of a modified additively manufactured rhombic dodecahedron 316l stainless steel lattice structure, *Thin-Walled Struct.* 148 (2020) 106586.

- [27] T. Tancogne-Dejean, A.B. Spierings, D. Mohr, Additively-manufactured metallic micro-lattice materials for high specific energy absorption under static and dynamic loading. *Acta Mater.* 116 (2016) 14–28.
- [28] L. Xiao, W. Song, C. Wang, H. Tang, Q. Fan, N. Liu, J. Wang, Mechanical properties of open-cell rhombic dodecahedron titanium alloy lattice structure manufactured using electron beam melting under dynamic loading, *Int. J. Impact Eng.* 100 (2017) 75–89.
- [29] A. Cuadrado, A. Yáñez, O. Martel, S. Deviaene, D. Monopoli, Influence of load orientation and of types of loads on the mechanical properties of porous Ti6Al4V biomaterials, *Mater. Des.* 135 (2017) 309–318.
- [30] P. Wang, X. Li, Y. Jiang, M.L.S. Nai, J. Ding, J. Wei, Electron beam melted heterogeneously porous microlattices for metallic bone applications: Design and investigations of boundary and edge effects, *Addit. Manuf.* 36 (2020) 101566.
- [31] H. Lei, C. Li, J. Meng, H. Zhou, Y. Liu, X. Zhang, P. Wang, D. Fang, Evaluation of compressive properties of SLM-fabricated multi-layer lattice structures by experimental test and μ -CT-based finite element analysis, *Mater. Des.* 169 (2019) 107685.
- [32] O. Al-Ketan, R. Rowshan, R.K.A. Al-Rub, Topology-mechanical property relationship of 3D printed strut, skeletal, and sheet based periodic metallic cellular materials, *Addit. Manuf.* 19 (2018) 167–183.
- [33] L. Yang, C. Han, H. Wu, L. Hao, Q. Wei, C. Yan, Y. Shi, Insights into unit cell size effect on mechanical responses and energy absorption capability of titanium graded porous structures manufactured by laser powder bed fusion, *J. Mech. Behav. Biomed. Mater.* 109 (2020) 103843.
- [34] Z. Ma, D.Z. Zhang, F. Liu, J. Jiang, M. Zhao, T. Zhang, Lattice structures of Cu-Cr-Zr copper alloy by selective laser melting: Microstructures, mechanical properties and energy absorption, *Mater. Des.* 187 (2020) 108406.
- [35] S. McKown, Y. Shen, W.K. Brookes, C.J. Sutcliffe, W.J. Cantwell, G.S. Langdon, G.N. Nurick, M.D. Theobald, The quasi-static and blast loading response of lattice structures, *Int. J. Impact Eng.* 2008, 35, 795–810.
- [36] T. Zhong, K. He, H. Li, L. Yang, Mechanical properties of lightweight 316L stainless steel lattice structures fabricated by selective laser melting, *Mater. Des.* 181 (2019) 108076.
- [37] X. Cao, S. Duan, J. Liang, W. Wen, D. Fang, Mechanical properties of an improved

- 3D-printed rhombic dodecahedron stainless steel lattice structure of variable cross section, *Int. J. Mech. Sci.* 145 (2018) 53–63.
- [38] Y. Xu, T. Li, X. Cao, Y. Tan, P. Luo, Compressive Properties of 316L Stainless Steel Topology - Optimized Lattice Structures Fabricated by Selective Laser Melting, *Adv. Eng. Mater.* 23 (3) (2021) 2000957.
- [39] L. Xiao, W. Song, C. Wang, H. Liu, H. Tang, J. Wang, Mechanical behavior of open-cell rhombic dodecahedron Ti–6Al–4V lattice structure, *Mater. Sci. Eng. A* 640 (2015) 375–384.
- [40] M. Mazur, M. Leary, S. Sun, M. Vcelka, D. Shidid, M. Brandt, Deformation and failure behaviour of Ti-6Al-4V lattice structures manufactured by selective laser melting (SLM), *Int. J. Adv. Manuf. Technol.* 84 (5) (2016) 1391–1411.
- [41] S.A. Yavari, S.M. Ahmadi, R. Wauthle, B. Pouran, J. Schrooten, H. Weinans, A.A. Zadpoor, Relationship between unit cell type and porosity and the fatigue behavior of selective laser melted meta-biomaterials, *J. Mech. Behav. Biomed. Mater.* 43 (2015) 91–100.
- [42] L. Xiao, W. Song, Additively-manufactured functionally graded Ti-6Al-4V lattice structures with high strength under static and dynamic loading: Experiments, *Int. J. Impact Eng.* 111 (2018) 255–272.
- [43] D.S. Al-Saedi, S.H. Masood, M. Faizan-Ur-Rab, A. Alomarrah, P. Ponnusamy, Mechanical properties and energy absorption capability of functionally graded F2BCC lattice fabricated by SLM, *Mater. Des.* 144 (2018) 32–44.
- [44] I. Maskery, N.T. Aboulkhair, A.O. Aremu, C.J. Tuck, I.A. Ashcroft, R.D. Wildman, R.J. Hague, A mechanical property evaluation of graded density Al-Si10-Mg lattice structures manufactured by selective laser melting, *Mater. Sci. Eng. A* 670 (2016) 264–274.
- [45] C. Yan, L. Hao, A. Hussein, S.L. Bubb, P. Young, D. Raymont, Evaluation of light-weight AlSi10Mg periodic cellular lattice structures fabricated via direct metal laser sintering, *J. Mater. Process. Technol.* 214 (4) (2014) 856–864.
- [46] A. Alhammadi, O. Al-Ketan, K.A. Khan, M. Ali, R. Rowshan, R.K.A. Al-Rub, Microstructural characterization and thermomechanical behavior of additively manufactured AlSi10Mg sheet cellular materials, *Mater. Sci. Eng. A* 791 (2020) 139714.
- [47] X. Li, Y.H. Tan, H.J. Willy, P. Wang, W. Lu, M. Cagirici, C.Y.A. Ong, T.S. Heng, J. Ding, Heterogeneously tempered martensitic high strength steel by selective laser melting and its

- micro-lattice: Processing, microstructure, superior performance and mechanisms, *Mater. Des.* 178 (2019) 107881.
- [48] H.D. Carlton, J. Lind, M.C. Messner, N.A. Volkoff-Shoemaker, H.S. Barnard, N.R. Barton, M. Kumar, Mapping local deformation behavior in single cell metal lattice structures, *Acta Mater.* 129 (2017) 239–250.
- [49] P. Koehnen, C. Haase, J. Buelmann, S. Ziegler, J.H. Schleifenbaum, W. Bleck, Mechanical properties and deformation behavior of additively manufactured lattice structures of stainless steel, *Mater. Des.* 145 (2018) 205–217.
- [50] Y. Amani, S. Dancette, P. Delroisse, A. Simar, E. Maire, Compression behavior of lattice structures produced by selective laser melting: X-ray tomography based experimental and finite element approaches, *Acta Mater.* 159 (2018) 395–407.
- [51] L. Liu, P. Kamm, F. García-Moreno, J. Banhart, D. Pasini, Elastic and failure response of imperfect three-dimensional metallic lattices: the role of geometric defects induced by Selective Laser Melting, *J. Mech. Phys. Solids.* 107 (2017) 160–184.
- [52] P. Li, Z. Wang, N. Petrinic, C.R. Siviour, Deformation behaviour of stainless steel microlattice structures by selective laser melting, *Mater. Sci. Eng. A* 614 (2014) 116–121.
- [53] M. Smith, Z. Guan, W.J. Cantwell, Finite element modelling of the compressive response of lattice structures manufactured using the selective laser melting technique, *Int. J. Mech. Sci.* 67 (2013) 28–41.
- [54] C.L. Li, H.S. Lei, Y.B. Liu, X.Y. Zhang, J. Xiong, H. Zhou, D.N. Fang, Crushing behavior of multi-layer metal lattice panel fabricated by selective laser melting, *Int. J. Mech. Sci.* 145 (2018) 389–399.
- [55] X. Yan, Q. Li, S. Yin, Z. Chen, R. Jenkins, C. Chen, J. Wang, W. Ma, R. Bolot, R. Lupoi, Z. Ren, H. Liao, M. Liu, Mechanical and in vitro study of an isotropic Ti6Al4V lattice structure fabricated using selective laser melting, *J. Alloys Compd.* 782 (2019) 209–223.
- [56] A. Suzuki, K. Sekizawa, M. Liu, N. Takata, M. Kobashi, Effects of heat treatments on compressive deformation behaviors of lattice-structured AlSi10Mg alloy fabricated by selective laser melting, *Adv. Eng. Mater.* 21 (10) (2019) 1900571.
- [57] L. Yang, C. Yan, W. Cao, Z. Liu, B. Song, S. Wen, C. Zhang, Y. Shi, S. Yang, Compression–compression fatigue behaviour of gyroid-type triply periodic minimal surface porous structures fabricated by selective laser melting, *Acta Mater.* 181 (2019) 49–

66.

- [58] C. Li, H. Lei, Z. Zhang, X. Zhang, H. Zhou, P. Wang, D. Fang, Architecture design of periodic truss-lattice cells for additive manufacturing, *Addit. Manuf.* 34 (2020) 101172.
- [59] H. Zhou, X. Cao, C. Li, X. Zhang, H. Fan, H. Lei, D. Fang, Design of self-supporting lattices for additive manufacturing, *J. Mech. Phys. Solids.* 148 (2021) 104298.
- [60] T. Tancogne-Dejean, D. Mohr, Elastically-isotropic truss lattice materials of reduced plastic anisotropy, *Int. J. Solids. Struct.* 138 (2018) 24–39.
- [61] D. Qi, H. Yu, M. Liu, H. Huang, S. Xu, Y. Xia, G. Qian, W. Wu, Mechanical behaviors of SLM additive manufactured octet-truss and truncated-octahedron lattice structures with uniform and taper beams, *Int. J. Mech. Sci.* 163 (2019) 105091.
- [62] A. Cutolo, B. Engelen, W. Desmet, B. Van Hooreweder, Mechanical properties of diamond lattice Ti–6Al–4V structures produced by laser powder bed fusion: On the effect of the load direction, *J. Mech. Behav. Biomed. Mater.* 104 (2020) 103656.
- [63] L. Yang, C. Yan, H. Fan, Z. Li, C. Cai, P. Chen, Y. Shi, S. Yang, Investigation on the orientation dependence of elastic response in Gyroid cellular structures, *J. Mech. Behav. Biomed. Mater.* 90 (2019) 73–85.
- [64] C. Crook, J. Bauer, A.G. Izard, C.S. de Oliveira, J.M.D. S. e Silva, J.B. Berger, L. Valdevit, Plate-nanolattices at the theoretical limit of stiffness and strength, *Nat. Commun.* 11 (1) (2020) 1–11.
- [65] A. Radman, X. Huang, Y.M. Xie, Topological optimization for the design of microstructures of isotropic cellular materials, *Eng. Optim.* 45 (11) (2013) 1331–1348.
- [66] D. Li, W. Liao, N. Dai, Y.M. Xie, Anisotropic design and optimization of conformal gradient lattice structures, *Comput. Aided Des.* 119 (2020) 102787.
- [67] H. Zong, H. Zhang, Y. Wang, M.Y. Wang, J.Y. Fuh, On two-step design of microstructure with desired Poisson's ratio for AM, *Mater. Des.* 159 (2018) 90–102.
- [68] M.S. Pham, C. Liu, I. Todd, J. Lertthanasarn, Damage-tolerant architected materials inspired by crystal microstructure, *Nature* 565 (2019) 305–311.
- [69] H. Lei, C. Li, X. Zhang, P. Wang, H. Zhou, Z. Zhao, D. Fang, Deformation behavior of heterogeneous multi-morphology lattice core hybrid structures, *Addit. Manuf.* 37 (2021) 101674.
- [70] Y. Liu, J. Zhang, X. Gu, Y. Zhou, Y. Yin, Q. Tan, M. Li, M.X. Zhang, Mechanical

performance of a node reinforced body-centred cubic lattice structure manufactured via selective laser melting, *Scr. Mater.* 189 (2020) 95–100.

- [71] C. Bonatti, Mohr, D, Large deformation response of additively-manufactured FCC metamaterials: From octet truss lattices towards continuous shell mesostructures, *Int. J. Plast.* 92 (2017) 122–147.

2. Effect of unit cell type on compressive behavior of lattice structures

2.1 Introduction

Lattice structures have displayed the huge potential in the application as impact energy absorber. The energy absorption capacity benefits from high-stress, flat and long plateau region of lattice structures as introduced in Chapter 1. The factors that affect the features of plateau region need to be clarified. A high plateau stress is reported to be attributed to good building quality with less geometric imperfections [1], small unit cell size [2, 3], stretch-dominated deformation pattern [4], node reinforcement or tapered strut [5, 6]. Desirable flat plateau region is normally related to the deformation behavior of lattice structures. Localized shear band often forms during compression and leads to the fluctuations of stress–strain curves. Investigation by Suzuki et al. [7] demonstrated that heat treatments on L-PBF produced AlSi10Mg alloy lattice structures resulted in high ductility and relatively stable plateau region. Bonatti et al. [8] investigated the large deformation behavior of solid and hollow octet truss lattice structures, suggesting that the hollow octet truss with uniform deformation behavior exhibited flat plateau region, whereas the solid octet truss with shear band exhibited oscillating stress–strain response. Long plateau region indicating large initial strain for densification is also important for energy absorption capacity. The study conducted by Han et al. [9] revealed that cracking free nickel-based superalloy lattice structure exhibited early densification compared to the lattice structure with cracking. Although the plateau stress was improved by tapering the struts, the plateau region was shorter than the lattice structure with uniform strut [10]. Accordingly, the influence of unit cell type on the plateau region dependent on the mechanical properties and deformation behaviors of lattice structures has been insufficiently studied.

In this chapter, the three different AlSi10Mg lattice structures composed of body-centered cubic (BCC), truncated octahedron (TO) and hexagon (Hexa) unit cells were manufactured via L-PBF process, in order to examine the influence of unit cell type on the mechanical properties and deformation behaviors. Quasi-static compression, static and high-speed indentation tests of lattice structures were carried out. Numerical lattice models were established for FEM analysis. X-ray computed tomography (CT) scanning was also conducted to characterize the interior deformation behaviors of lattice structures.

2.2 Materials and methods

2.2.1 Manufacture of lattice structures by L-PBF

In this study, a nitrogen gas-atomized AlSi10Mg alloy powder (**Fig. 2-1**) with the density of $2.67 \text{ g}\cdot\text{cm}^{-3}$ was used as raw material for L-PBF fabrication of lattice structures. This material was selected since it is one of the most common materials used for the L-PBF process, and its microstructure and mechanical properties of bulk and lattice specimens were clarified in detail [11-13]. In addition, appropriate heat treatments for improving the microstructural homogeneity, isotropy of mechanical properties, and ductility were also clarified [7, 11], which further make AlSi10Mg alloy an appropriate material for investigating the compressive behavior of lattice structure. The chemical composition of the alloy is provided in detail elsewhere [11]. A L-PBF manufacturing system EOSINT M 280 (EOS GmbH, KrailingCity, Germany) equipped with Yb-fiber laser was applied. The used processing parameters were optimized and given in **Table 2-1**. The scanning tracks of laser beam applied in this study is shown schematically in the previous study [11]. The processing was under an argon atmosphere and the temperature of 25° . It is reported that the as-fabricated lattice structure fractured and did not exhibit plateau region under compression due to poor ductility [7]. Therefore, annealing treatment at 300°C for 2 h and subsequent slow furnace cooling were performed to improve the ductility of lattice structures.

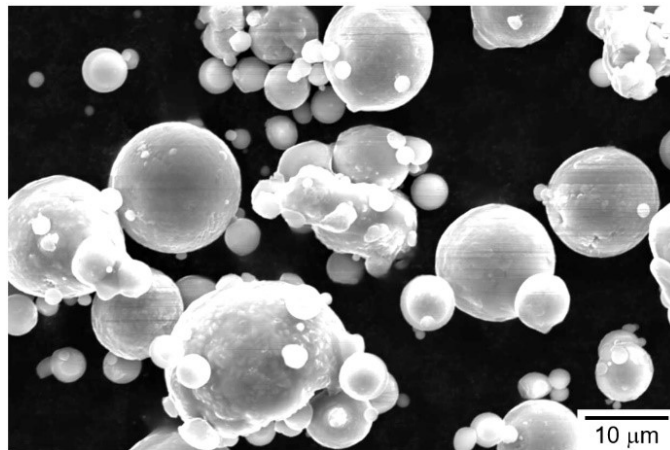


Fig. 2-1 AlSi10Mg gas-atomized powder used in this study

Table 2-1 Applied L-PBF processing parameters

Laser power	380 W
Scan speed	1 m·s ⁻¹
Layer thickness	30 μm
Hatch distance	100 μm
Rotation angle between layers	67°

2.2.2 Designs of lattice structure

As shown in **Fig. 2-2**, the three type lattice structures including BCC, TO, and Hexa were manufactured by building up continuous layers based on 3D computer-aided design (CAD) models. The BCC and TO unit cells have same aspect ratio of 1, but Hexa unit has the aspect ratio of 0.5. The diameter and height of the lattice structures with cylinder outline geometry were 30 mm. The lattice structures with various relative densities (ρ^*/ρ_s) were produced for each type. The measured relative densities (ρ^*/ρ_s) using the Archimedes' method of all the lattice structures were as follows: 0.06, 0.16, 0.27 for the BCC type; 0.07, 0.17, 0.27 for the TO type; and 0.07, 0.18, 0.29 for the Hexa type.

2.2.3 Measurements

The compressive performances of the lattice structures were investigated through quasi-static uniaxial compression experiments. The loading was applied by a hydraulic universal testing machine (capacity: 4.9×10^5 N) along the building direction, according to ISO 13314 [14]. An initial strain rate of 2.2×10^{-3} s⁻¹ was used. Nominal stress was defined as the force divided by the original sectional area. Nominal strain was defined as the value of displacement along the loading direction divided by the original height of lattice structures. When the lattice structures were deformed at the approximately 20% compressive strain, X-ray CT scanning was conducted to characterize the deformation behavior of interior struts. TOSCANER-32252μhd (Toshiba, Tokyo, Japan) at 180 kV voltage and 45 μA current was used for scanning.

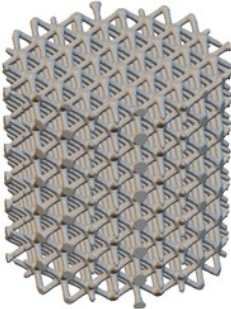
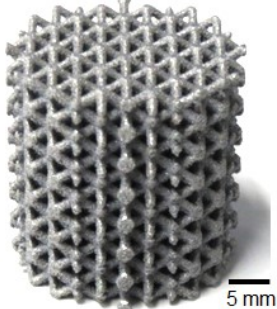
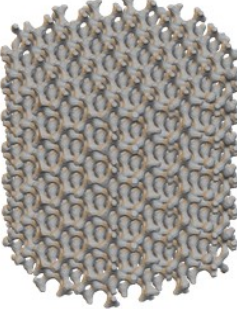
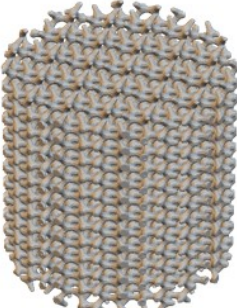
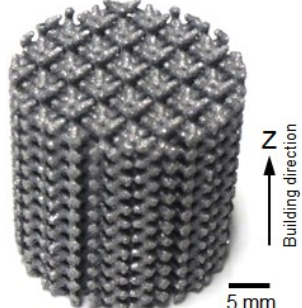
	Unit cell	Lattice model	Lattice structure
BCC	 <p>height: 4.2 mm width: 4.2 mm</p>		 <p>5 mm</p>
TO	 <p>height: 4.7 mm width: 4.7 mm</p>		 <p>5 mm</p>
Hexa	 <p>height: 2.5 mm width: 5.0 mm</p>		 <p>5 mm</p> <p>Z ↑ Building direction</p>

Fig. 2-2 L-PBF produced body-centered cubic (BCC), truncated octahedron (TO), and hexagon (Hexa) lattice structures and corresponding computer-aided design (CAD) lattice models and unit cells.

Lattice structures have been considered to utilize as protection for absorbing impacting energy during spacecrafts landing in the Smart Lander for Investigating Moon (SLIM) project, conducted by Japan Aerospace Exploration Agency (JAXA) [15, 16]. In such case, lattice structures are normally pushed-in by the components of spacecraft at high speed. In order to accurately investigate the compressive behaviors of lattice structures under this loading condition, static and high-speed indentation experiments were carried out. The schematic diagram of the static indentation tests is illustrated in **Fig. 2-3**. Lattice structures with cylinder geometry (diameter: 40 mm, height: 30 mm) were embedded in a die (outer diameter: 60 mm,

inner diameter: 40 mm, height: 31 mm). The lattice structures including BCC, TO, and Hexa types have the same relative density of 0.07. The indenter (diameter: 25 mm, height: 25 mm) was pushed into lattice structures in an initial strain rate of $2.2 \times 10^{-3} \text{ s}^{-1}$. The interfaces between the die and lattice structures were lubricated to decrease the friction, while the indenter contacted lattice structure without lubricating. **Figure 2-4** presents (a-d) the apparatus and lattice structure applied for the high-speed indentation test and (e) illustration of the high-speed indentation test. The lattice structures with cylinder outline (diameter: 40 mm, height: 30 mm) were embedded in the crushable balls (**Fig. 2-4a**), which were ejected by the ballistic range and crashed to the target concrete. The shooting speed of $27.0 \text{ m}\cdot\text{s}^{-1}$ was approximately 4.0×10^5 times faster than the static indentation tests ($6.7 \times 10^{-5} \text{ m}\cdot\text{s}^{-1}$). The high-speed impact between the crushable ball and target imitated the hard landing of spacecraft on moon. The lattice structures in the crushable ball were pushed-in by the payload to provide deformation resistance for deceleration, whose value was record by an accelerometer.

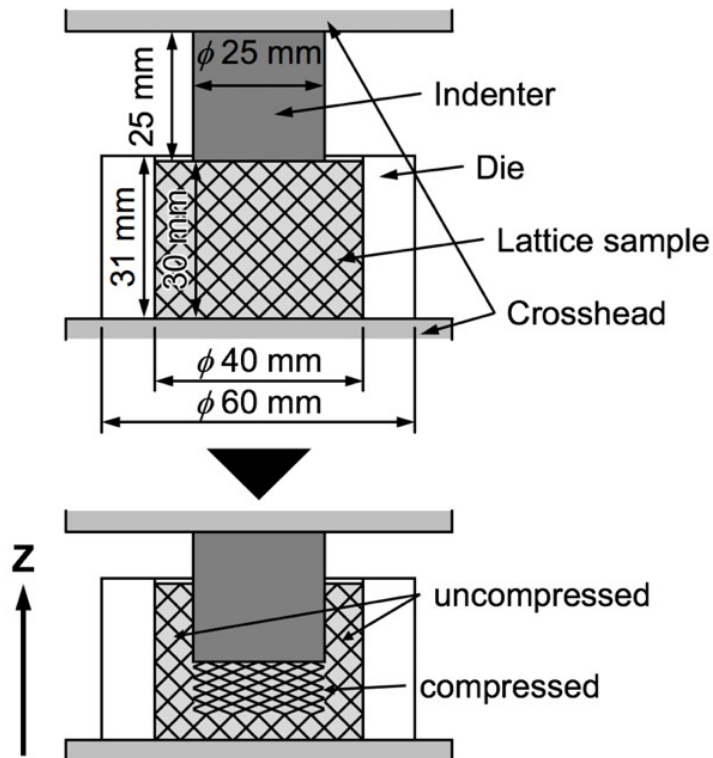


Fig. 2-3 Schematic illustration of static indentation tests.

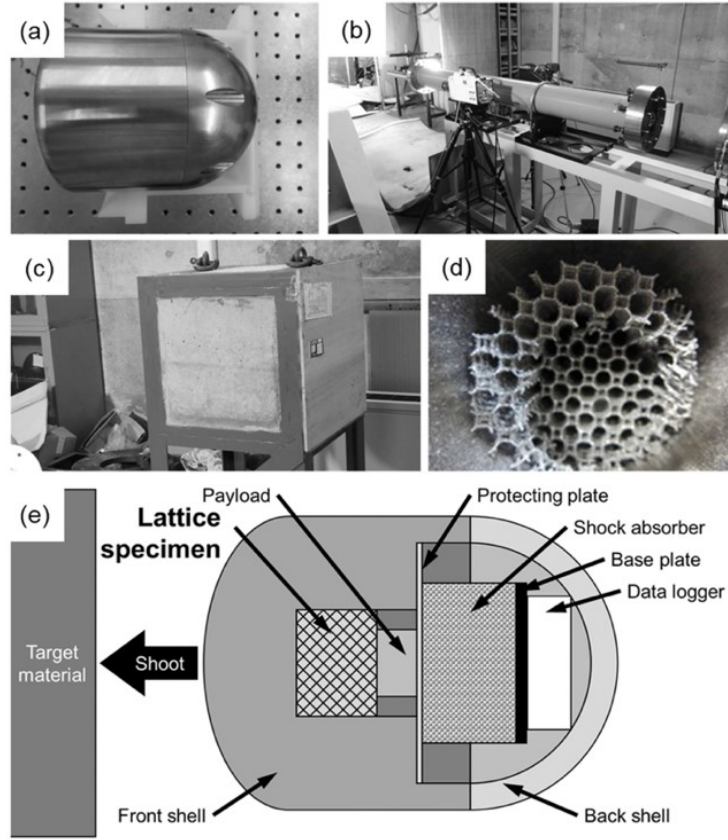


Fig. 2-4 (a-d) Photographs showing the apparatus and lattice structure used for high-speed indentation test: (a) crushable ball, (b) ballistic range, (c) target, and (d) TO lattice structure pushed-in by payload. (e) Schematic illustration of high-speed indentation test.

Assuming the lattice structures can exhibit constant mechanical properties under static and high-speed static indentations, the value of deceleration of the payload can be assessed from the static indentation test, using the motion-force equation for the payload as follows.

$$m_p a_p = \sigma_L S_p \quad (2.1)$$

where, m_p , a_p , and S_p are the mass, deceleration, and contact area of the payload. σ_L denotes the nominal stress of lattice structures. The plateau stress obtained from static indentation test was substituted into σ_L of Eq. (2.1) to estimate the deceleration of payload.

2.2.4 Finite element method

FEM analysis was conducted using Femtet 2019 (Murata Software, Tokyo, Japan). In order to save the calculation cost, reduced lattice models with 45 unit cells ($x \times y \times z = 3 \times 3 \times 5$) were

established for elasto-plastic analysis (**Fig. 2-5**). The relative density of each model was consistent with the corresponding lattice structure. The solid element of models was discretized by tetrahedral meshes (size: 0.3 mm). The input material properties, as given in **Table 2-2**, were obtained from the tensile tests of L-PBF manufactured AlSi10Mg bulk after annealing treatment at 300 °C for 2 hours [11]. The forced displacement of 10% height of lattice models were implemented on the top plane along Z direction. The top plane was fixed in X and Y direction, and the bottom plane was constrained in all degree of freedoms, in order to simulate the compressive experiments carried out with no lubrication.

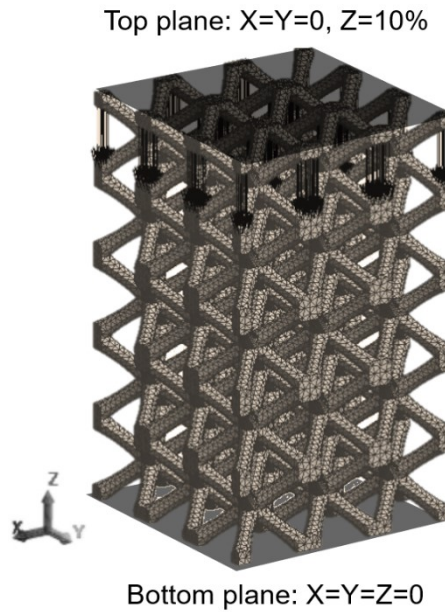


Fig. 2-5 An example of BCC lattice model for FEM analysis.

Table 2-2 Material properties applied for FEM analysis. The input properties were obtained from the tensile tests of L-PBF manufactured AlSi10Mg bulk after annealing treatment at 300 °C for 2 hours [11].

Young's modulus, E / GPa	60
Poisson's ratio, ν	0.3
Yield stress, σ_{YS} / MPa	200
Work hardening coefficient, n	0.2

2.3 Results

2.3.1 Mechanical property

Figure 2-6 presents stress–strain responses of representative BCC ($\rho^*/\rho_s = 0.16$), TO ($\rho^*/\rho_s = 0.17$), and Hexa ($\rho^*/\rho_s = 0.18$) lattice structures under quasi-static uniaxial compression. Three different stages were characterized in the stress–strain curves: initial linear elastic behavior, plateau region under larger deformation in plasticity, and densification region, as suggested in Chapter 1 and other researches [17-19]. The stiffness and yield strength in descending order of the three lattice structures were: TO, Hexa, and BCC. In the plateau regions, the BCC and TO lattice structures displayed stress fluctuations, while the Hexa lattice structure exhibited stable plateau stress. For the densification behavior, the Hexa lattice structure showed earlier densification (initial strain: 36.9%) than BCC (52.5%) and TO (58.6%) lattice structures. According to the ISO 13314 standard, the plateau stress of cellular structure is typically defined as the average nominal stress in the strain range of 20%~30%; the initial strain for densification is determined as the nominal strain at which the nominal stress is 1.3 times higher than the plateau stress. However, the flow stress of BCC and TO lattice structures showed oscillation in the strain range of 20%~30%, thus the average nominal stress in the strain range of 5%~10% is defined as the plateau stress here in order to avoid underestimation. The calculated plateau stress (σ_{pl}^*) and initial strain for densification against the relative densities (ρ^*/ρ_s) of BCC, TO, and Hexa lattice structures are plotted in **Fig. 2-7**. With the increase of relative density, the plateau stresses showed an increasing trend, whereas the initial strains for densification showed decreasing trend. The power-law relationship between plateau stress and relative density can be expressed in Gibson-Ashby equation, as follows:

$$\sigma_{pl}^* = C \left(\frac{\rho^*}{\rho_s} \right)^n \quad (2.2)$$

Table 2-3 shows the derived coefficient C and exponent n. The range of 2.1~2.4 for exponent was observed for the three lattice structures. Kitazono suggested that the TO lattice structure exhibited the exponent value of 2.1 [16], which is in line with the results in this study. Generally, the TO lattice structure with high plateau stress and large initial strain for densification exhibits superior energy absorption capacity, compared to BCC and Hexa lattice structures with close relative density.

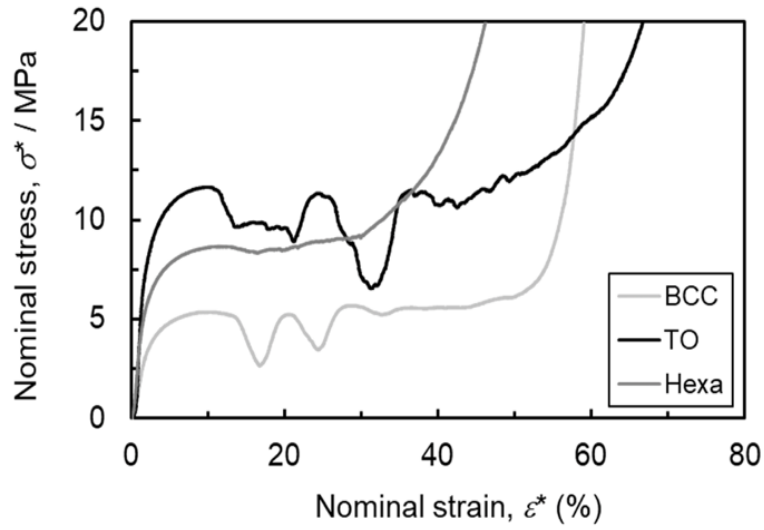


Fig. 2-6 Stress–strain responses of BCC ($\rho^*/\rho_s = 0.16$), TO ($\rho^*/\rho_s = 0.17$), and Hexa ($\rho^*/\rho_s = 0.18$) lattice structures.

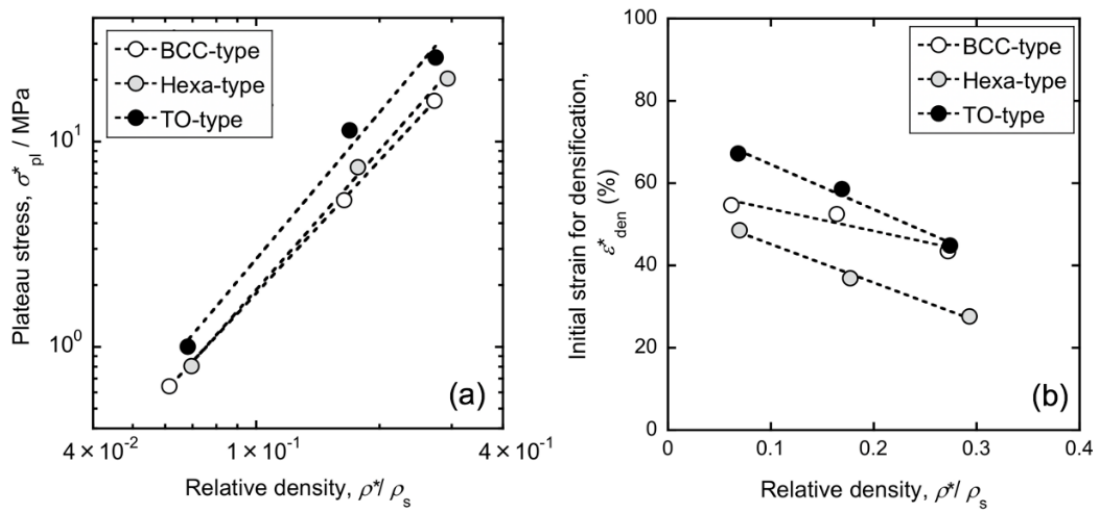


Fig. 2-7 Changes in (a) plateau stress and (b) initial strain for densification as a function of relative density.

Table 2-3 Coefficient C and exponent n for the BCC, TO, and Hexa lattice structures in the Gibson-Ashby equation.

	C / MPa	n
BCC	257	2.1
TO	345	2.3
Hexa	633	2.4

2.3.2 Deformation behavior

Figure 2-8 illustrates the photographs of lattice structures captured before compression and during compression at 20%, 40%, and 60% nominal strains. The representative lattice structures with close relative density (0.16 for BCC, 0.17 for TO, and 0.18 for Hexa) were presented. It is clear that the deformation was localized in a diagonal plane, i.e. shear band formation, for BCC and TO lattice structures at 20% nominal strain. This deformation behavior led to the fluctuation of stress–strain curves shown in **Fig. 2-6** as reported studies [7, 20]. Another shear band generated at different locations accompanied by stress drops under continuous compression. When the lattice structures were further compressed, the struts contacted with each other and resulted in structure densification, meanwhile the nominal stress rapidly increased in a small strain. For Hexa lattice structure, a barrel-like deformation behavior with expansion at middle height was observed owing to the restraint of top and bottom surface by the friction. Noted that shear band formation or distinct fracture did not appear before densification for Hexa lattice structure during the compression process, indicating the uniform and successive deformation behavior. In addition, similar deformation mode was characterized in the lattice structures with

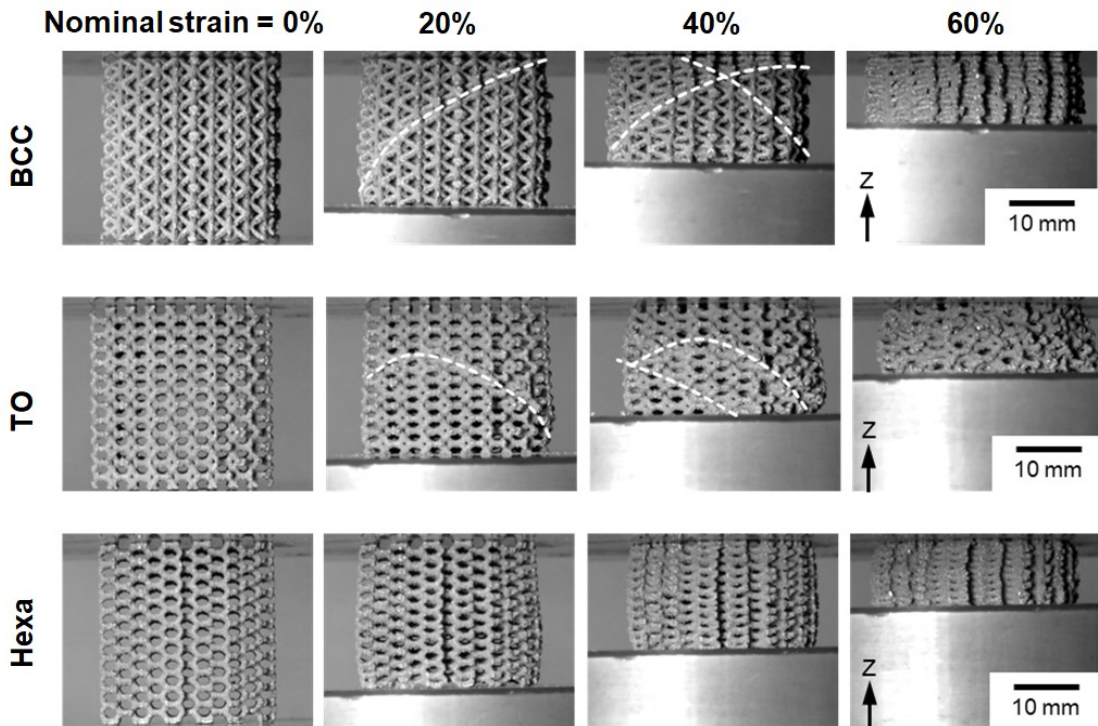


Fig. 2-8 Test appearances of BCC ($\rho^*/\rho_s = 0.16$), TO ($\rho^*/\rho_s = 0.17$), and Hexa ($\rho^*/\rho_s = 0.18$) lattice structures before compression and compressed at different nominal strains.

different relative density and same unit cell type. This revealed that the deformation behaviors of lattice structures are more dependent on the types of unit cell, less dependent on the relative densities.

When the lattice structures were compressed at 20% nominal strain, the tests were interrupted to carried out X-ray CT scanning. **Figure 2-9** presents the front view of the reconstruction models and cross-sections perpendicular and parallel to Z direction. It is observed that the diagonal shear bands were generated in BCC and TO lattice structures, and Hexa lattice structure exhibited no shear band formation, from the front view of the three models. This result coincides well with the deformation behavior shown in **Fig. 2-8**. As marked by the square in the cross-sections of BCC and TO lattice structures, the occurrence of cracks or fractures of struts were relevant to the shear band formation. The parallel results of crack generation in BCC lattice structures were found in the literatures [7, 21]. For Hexa lattice structure without shear band, both front view of model and cross-sections exhibited high symmetry of the deformed structure, indicating the uniform deformation consistently. The cracks in struts were not found within the capacity of the applied X-ray CT apparatus. Therefore, the initiation of cracks in struts may be related to the shear band formation. As shown in **Fig.**

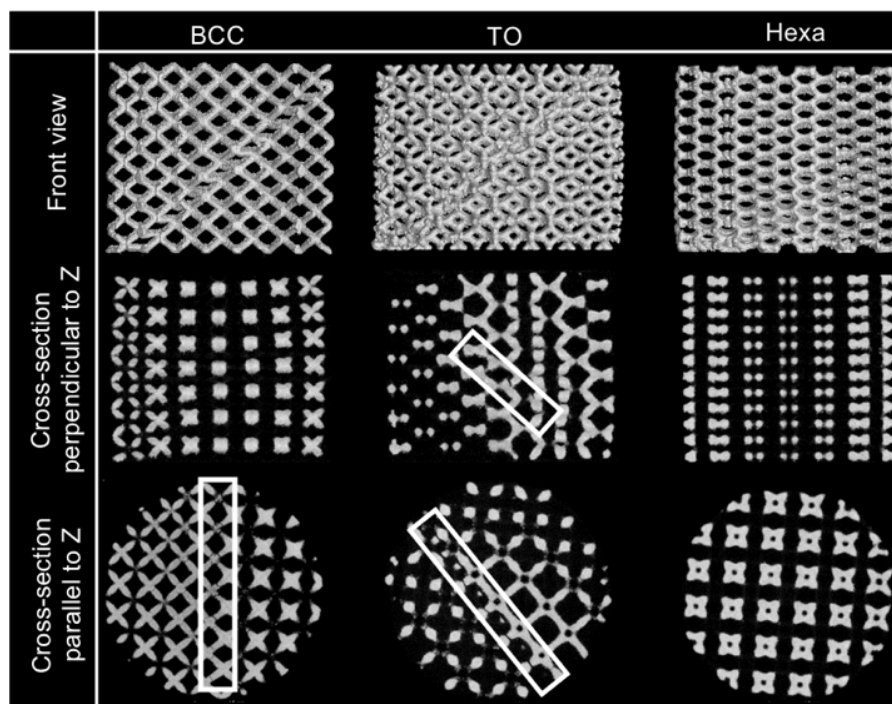


Fig. 2-9 X-ray computed tomography (CT) observations at 20% compressive strain.

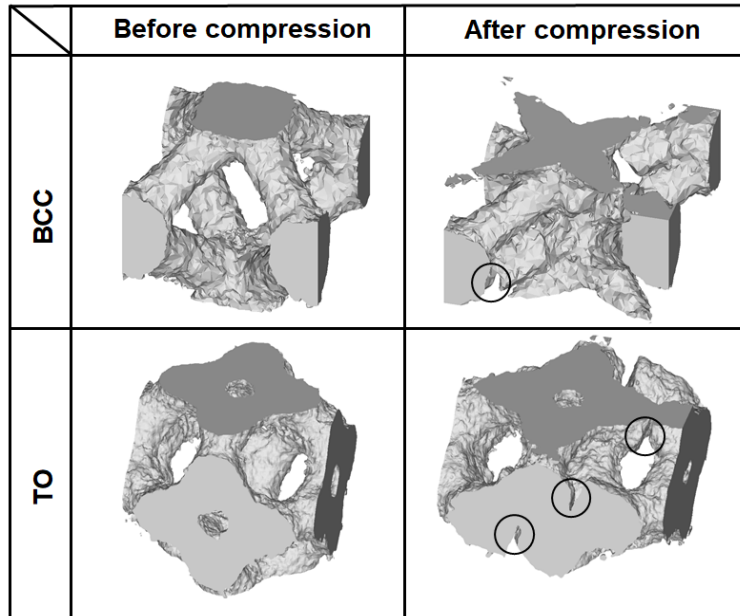


Fig. 2-10 X-ray CT images of undeformed and deformed unit cells in BCC and TO lattice structures.

2-10, the detail insights into the deformation behaviors of interior struts are obtained from the X-ray CT models of compressed and uncompressed BCC and TO lattice structures. It is shown that the initiation of cracks in struts was observed at the region near node. The reported study also suggested that the cracks generated near node in BCC lattice structure [7].

2.3.3 Static and high-speed indentation test

The comparison of stress–strain responses between static compression and indentation test of BCC, TO, and Hexa lattice structures is shown in **Fig. 2-11**. The nominal stress level of indentation tests was greater than that of static compression. The plateau regions of static compression were more stable with less fluctuations compared to those of indentation tests. The high and more frequently fluctuated flow stress is due to shear fracture of struts at the boundary between deformed and undeformed regions. The indenter needs to not only deform the lattice structure in the compressive direction but also fracture the struts at the boundary between the deformed and undeformed regions, resulting in high flow stress. The fluctuations of stress–strain curves led by shear fracture of struts in indentation tests were more frequent than those led by shear band formation in static compressions. Generally, the similar tendencies of stress–strain responses obtained by the two different tests are observed for each lattice structure.

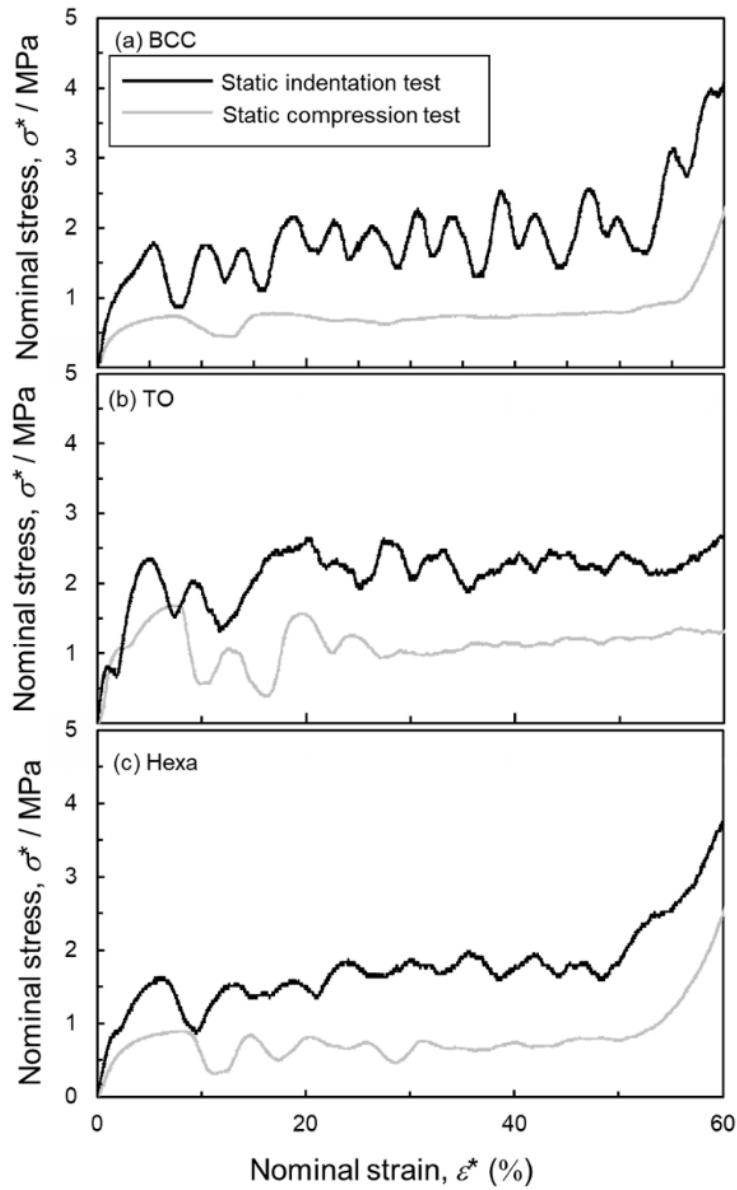


Fig. 2-11 Stress–strain curves obtained by static compression and indentation test of (a) BCC, (b) TO and (c) Hexa lattice structures.

Figure 2-12 shows the relationships between the deceleration in the high-speed indentation test and time for the three lattice structures. The deceleration showed a general tendency of increase, constant, and decrease to 0 for all the lattice structures. The constant value of deceleration that was provided by constant resistance force corresponds to the plateau region of lattice structure. To compare the mechanical properties obtained from static and high-speed

indentation tests, the decelerations were evaluated from the plateau stress of static indentation test by Eq. (2.1), as shown in horizontal dotted lines. The calculated decelerations of TO and Hexa lattice structures coincided well with the experimental decelerations. This result suggests that the mechanical properties in the high-speed practical case, especially energy absorption capacity, can be estimated by the static test for TO and Hexa lattice structures. However, the calculated deceleration of BCC lattice structures exhibited low value compared to the

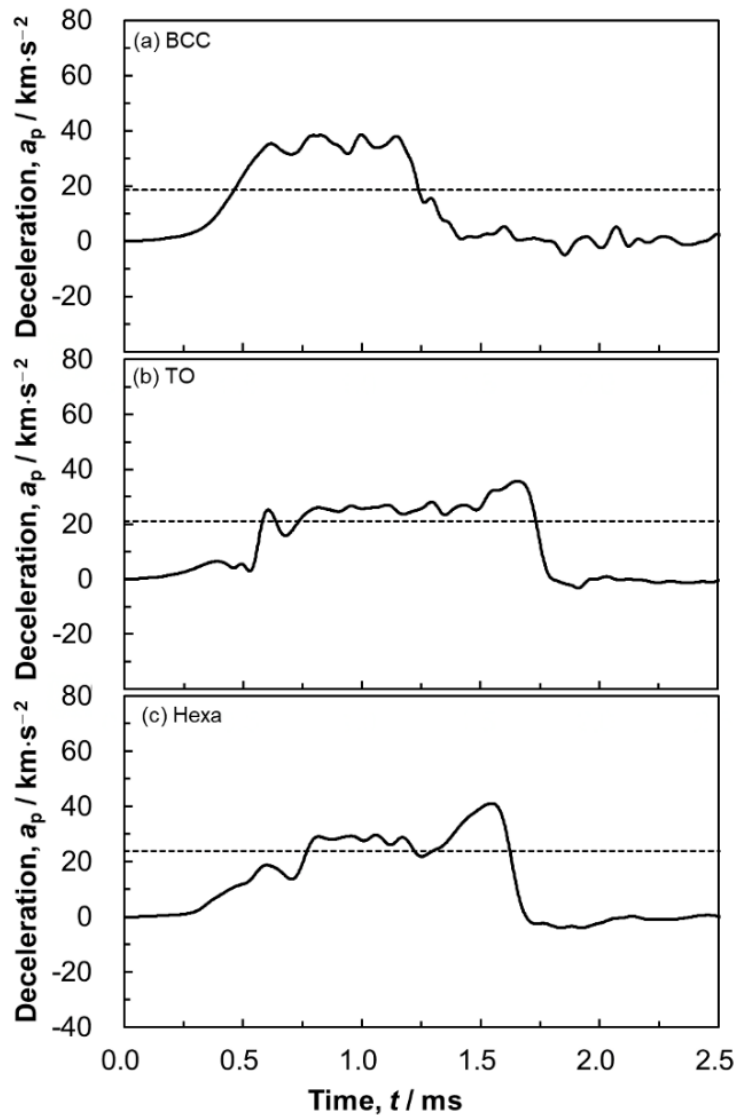


Fig. 2-12 Changes in deceleration obtained by the high-speed indentation test as a function of time: (a) BCC, (b) TO and (c) Hexa lattice structures. The horizontal broken lines indicate the deceleration estimated from the plateau stress in the stress–strain curves of static indentation test shown in Fig. 2-11.

experiment, indicating certain strain rate dependence. The sensitivity of the strain rate dependence for lattice structures with different unit cell type needs to be investigated through systematic investigations in the future.

2.4 Discussion

2.4.1 Compressive behavior

The differences of plateau stress and deformation behavior among the three different lattice structures were investigated by FEM analysis. **Figure 2-13** shows the stress–strain responses of established lattice models. TO lattice model exhibited the highest compressive strength, and BCC lattice model exhibited the lowest compressive strength. Compared to the experimental results in **Fig. 2-6**, the similar tendency of the curves was obtained, indicating the reliable simulation. **Figure 2-14** shows (a-c) contour maps and (d-f) histograms showing the Mises stress distribution in each lattice model at 10% nominal strain. The colors of bars in the histograms correspond to those of the contour maps. The struts perpendicular to the loading direction existed in TO and Hexa lattice model, where the most elements exhibited low stress distribution (**Fig. 2-14 bc**). The inclined struts showed relatively high and uniform stress (**Fig. 2-14 bc**). In comparison to the TO and Hexa lattice model, BCC lattice model has inclined struts with large aspect ratio and no strut perpendicular to the Z direction. In the elongated struts in the BCC lattice model, high stresses were distributed at the regions near nodes, while the center region of struts exhibited moderate stresses (**Fig. 2-14 a**). As illustrated in the histograms (**Fig. 2-14 d-f**), the Mises stresses were in the range of 0~600 MPa for the three lattice models. In the

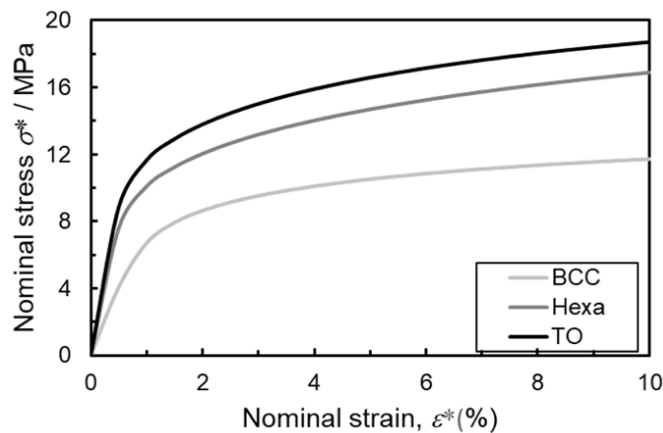


Fig. 2-13 Stress–strain responses of BCC, TO and Hexa lattice models obtained by the FEM analysis.

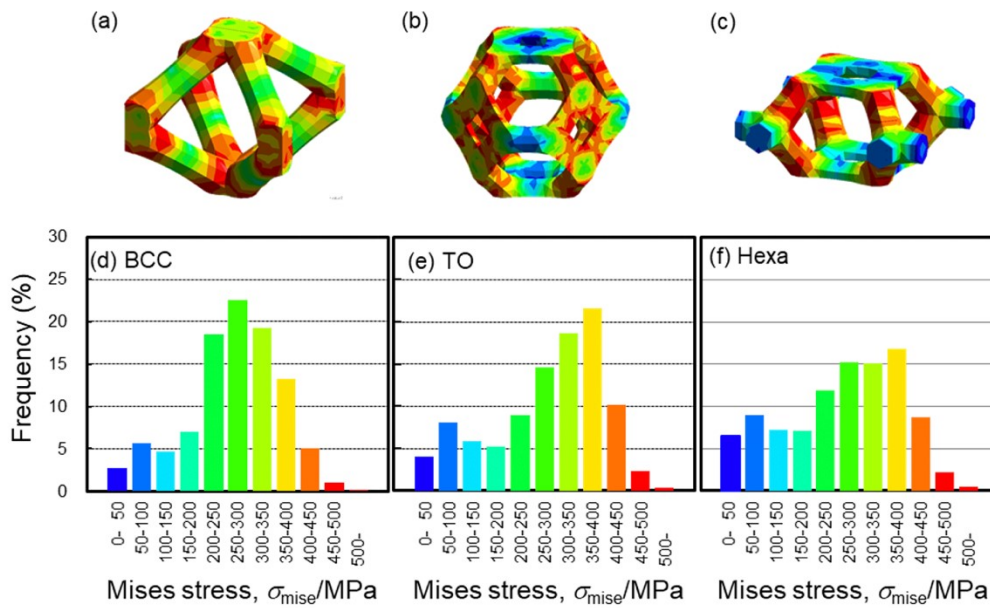


Fig. 2-14 (a-c) Contour maps and (d-f) histograms showing the Mises stress distributions in BCC, TO and Hexa models obtained by FEM analysis. The colors for bars in the histograms correspond to the those of the contour maps.

BCC lattice model, the stress range of 200~400 MPa was frequently distributed. This stress range was generally in correspondence with the stresses localized in the center region of struts (**Fig. 2-14 a**). In the TO lattice model, the majority of the elements exhibited high stress of 300~450 MPa. Similarly, the same range of Mises stress was frequently distributed in the Hexa lattice structure. But the fraction of low Mises stress less than 250 MPa was also relatively high compared to the other two models, because of more struts perpendicular to the loading direction in Hexa lattice model. These findings suggested that the high strength and plateau stress of TO lattice structure with thick and short struts and less struts perpendicular to the loading direction, are attributed to the uniform distribution of high Mises stress. Therefore, the struts that oriented not perpendicularly to the loading direction and exhibited small aspect ratio are desirable for the design of unit cells, with the aim of improving the strength of lattice structures.

The Hexa lattice structure exhibited stable deformation behavior without the appearance of shear band and consequential flat plateau region, which are distinct from the BCC or TO lattice structure (**Figs. 2-6** and **2-8**). The investigations of previous studies suggested that the cracks generated on the tension stress region of bended struts as a result of the shear band formation [7, 22]. Actually, the crack initiations near nodes were found in the tomography of compressed

BCC and TO lattice structure (Figs. 2-9 and 2-10). Thus, it is considered that the shear band formation is related to the crack generations owing to localized tensile stress. The maximum principal stress distributions of the three lattice models are therefore compared and shown in Fig. 2-15 a-c. The regions marked by arrows of BCC and TO lattice models indicated the high maximum principal stress, which roughly corresponded to cracks generation regions in Fig.

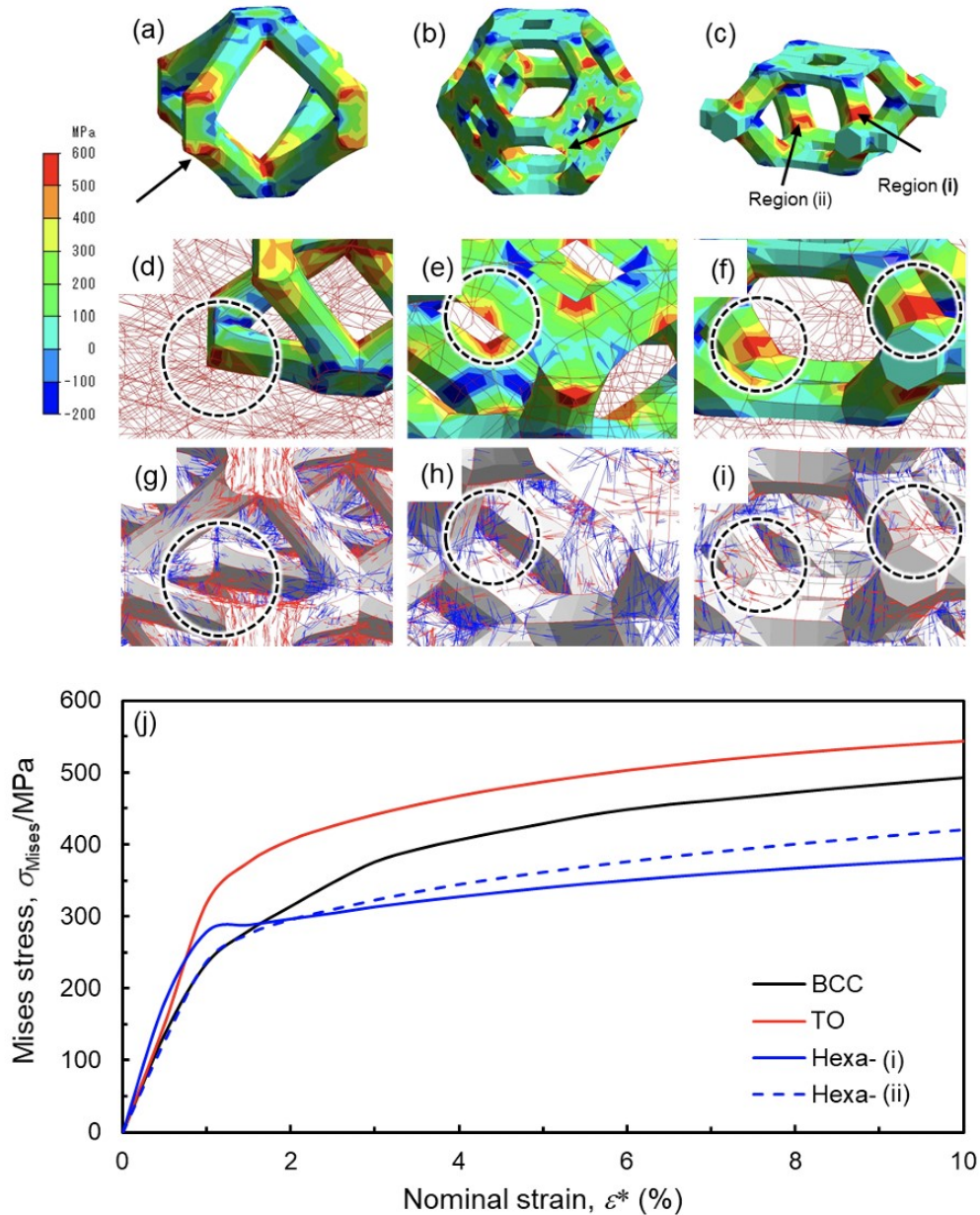


Fig. 2-15 (a-f) Maximum principal stress distributions and (g-i) surface vectors of principal stresses in the (a, d, g) BCC, (b, e, h) TO and (c, f, i) Hexa lattice models. (j) Change in the Mises stress at the positions marked by arrows in (a-c).

2-10. **Figure 2-15 d-i** shows the (d-f) the enlarged maximum principal stress distributions, and (g-i) the vector of the principal stress on the strut surfaces. The vectors in red color indicate the principal stress in tension, and those in blue indicate the principal stress in compression. As for the BCC and TO lattice models, arrow-marked regions in struts exhibited high tensile principal stress (**Fig. 2-15 d, e, g, h**). This behavior demonstrated that the crack generation due to stress concentration on the struts under tension lead to the shear band formation. In the case of Hexa lattice model, the two regions ((i) and (ii)) in the vicinity of nodes exhibiting high maximum principal stress with positive values were arrow-marked (**Fig. 2-15c**). The relationships between Mises stresses at the arrow-marked regions and the nominal strains of the three different lattice models are shown in **Fig. 2-15j**. Both the regions (i) and (ii) of Hexa lattice model exhibited lower Mises stress compared to the crack initiation positions of BCC and TO lattice models, when the nominal strain was larger than 2%. This result is in accordance with the deformation behavior of Hexa lattice structure without occurrence of cracks and shear band formation. Therefore, the uniform and stable deformation of lattice structures under compression can be achieved by low level of localized stress at tensile parts. Detailed formation sequence of shear band formation is discussed in the Chapter 3.

The early densification with small initial strain was observed in Hexa lattice structure compared to BCC and TO lattice structures (**Figs. 2-6 and 2-7b**). The densification of lattice structures starts when many struts contact with each other, and gradually there is no space for large deformation of struts in the compressive direction. **Figure 2-16** presents the cross-sections parallel to loading direction of the CAD lattice models. The cross-sections were selected to show the most struts in a vertical plane. The numbers of dotted arrow-marked struts are 14, 13 and 22 for BCC, TO, and Hexa lattice structures, respectively. It is considered that the densification initiates when the marked struts overlap. Thus, the predicted nominal strain for strut contact were calculated on the basis of strut number and diameter in lattice structure, as expressed in **Eq. (2.3)**.

$$\varepsilon_{con}^* = 1 - \frac{t \times N}{h} \quad (2.3)$$

where h , t , and N are the height of lattice structures, the diameter of strut, and the number of arrow-marked struts as shown in **Fig. 2-16**. The estimation values of the nominal strains for strut contacts were generally in line with the initial strains for densification obtained from the

experiments of representative lattice structures with close relative density, as shown in **Table 2-4**. Therefore, the reason of small initial strain for densification in Hexa lattice structure is due to higher number density of struts overlapping in the loading direction than those in BCC and TO lattice structures.

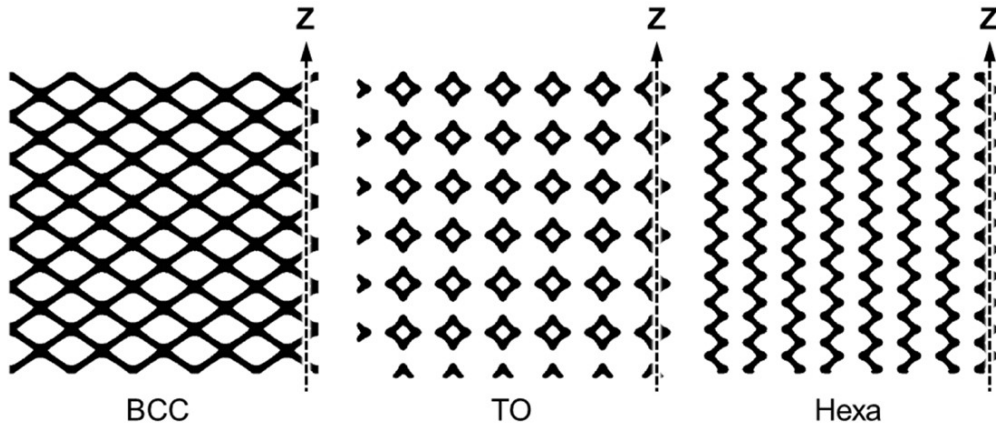


Fig. 2-16 Cross-sections of CAD models showing the BCC, TO and Hexa lattice structures. These cross-sections include the most struts in each lattice structure.

Table 2-4 Comparison between estimated nominal strain for strut contact and experimental initial strains for densification of representative BCC, TO, and Hexa lattice structures.

Lattice structure	Estimated nominal strain for strut contact	Experimental initial strains for densification
BCC ($\rho^*/\rho_s = 0.16$)	59 %	53 %
TO ($\rho^*/\rho_s = 0.17$)	66 %	59 %
Hexa ($\rho^*/\rho_s = 0.18$)	34 %	37 %

2.4.2 Energy absorption capacity

The energy absorption capacities of AlSi10Mg BCC, TO, and Hexa lattice structures in the present study are compared with reported lattice structures made of Ti-6Al-4V titanium alloy [23, 24], Al-12Si aluminum alloy [20], Cu-Cr-Zr copper alloy [25] and 316L stainless steel [26, 27]. **Figure 2-17** presents the relationship between energy per unit volume and bulk density of these lattice structures. Generally, aluminum alloy lattice structures exhibit lower energy absorption capacities compared to titanium alloy lattice structures, but higher capacities than

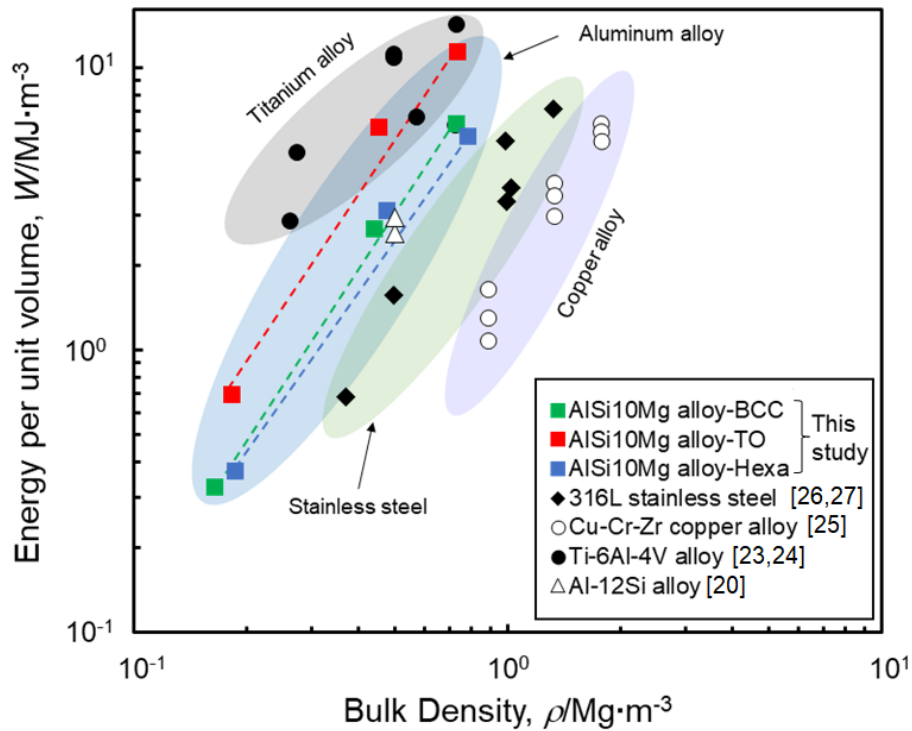


Fig. 2-17 Changes in energy absorption capacities of AlSi10Mg lattice structures in the present study and other reported lattice structures made of various materials as a function of the bulk density.

stainless steel and copper alloy lattice structures, when their bulk densities are close. For the AlSi10Mg lattice structures in this study, the similar energy absorption capacities are observed in BCC and Hexa lattice structures. In the case of TO lattice structures, obviously higher capacities than the BCC and Hexa lattice structures are shown. In addition, the TO lattice structure ($\rho^*/\rho_s = 0.27$) exhibits the highest energy per unit volume of $11.4 \text{ MJ}\cdot\text{m}^{-3}$ in this study. It is noted here the high capacity of AlSi10Mg TO lattice structure is in the range of titanium alloy lattice structures. This demonstrates that the requirement of high energy absorption can be met by aluminum alloy lattice structures with TO unit cells, instead of using expensive titanium alloy. Furthermore, energy absorption capacity of the TO lattice structure (**Fig. 2-17**) would be applied to the other materials, indicating the potential improvement of the performance of the titanium alloy lattice structure with the TO-type unit cell.

2.5 Conclusions

In this chapter, the AlSi10Mg lattice structures consisting of three different unit cells of body-centered cubic (BCC), truncated octahedron (TO) and hexagon (Hexa) configurations were manufactured by laser powder bed fusion (L-PBF). The compression experiments, X-ray CT, and FEM analysis were applied to elucidated the influence of the unit cell type on the mechanical properties and deformation behaviors of lattice structures. Based on the results, the following conclusions were drawn:

- (1) TO lattice structure exhibited higher yield strength and plateau stress than the BCC and Hexa lattice structures. FEM results suggested that high Mises stress was distributed in the most elements of TO lattice model, conversely the low Mises stress was frequently observed in BCC lattice model.
- (2) Shear band formation occurred in BCC and TO lattice structures during compression, resulting in the fluctuation of stress–strain curves. Cracks and fractures of struts in compressed lattice structures were found in X-ray CT observation. Continuous deformation behavior was observed in Hexa lattice structure without struts cracking, which was attributed to the FEM results that concentrated Mises stress at tensile stress part was lower.
- (3) Hexa lattice structure exhibited small initial strain for densification. A larger number of struts in compression direction led to the struts overlapping and early densification.
- (4) High-speed indentation tests indicated that the practical energy absorption capacities of TO and Hexa lattice structures can be estimated by static indentation tests.
- (5) Aluminum alloy lattice structures exhibited higher energy absorption capacities in comparison to the stainless steel and copper alloy lattice structures. The TO AlSi10Mg lattice structure with superior energy absorption capacity reached the level of titanium alloy lattice structures.

References

- [1] L. Xiao, W. Song, M. Hu, P. Li, Compressive properties and micro-structural characteristics of Ti–6Al–4V fabricated by electron beam melting and selective laser melting, *Adv. Eng. Mater.* 764 (2019) 138204.
- [2] F. Liu, Q. Ran, M. Zhao, T. Zhang, D.Z. Zhang, Z. Su, Additively manufactured continuous cell-size gradient porous scaffolds: pore characteristics, mechanical properties and

- biological responses in vitro, *Materials* 13(11) (2020) 2589.
- [3] L. Yang, C. Han, H. Wu, L. Hao, Q. Wei, C. Yan, Y. Shi, Insights into unit cell size effect on mechanical responses and energy absorption capability of titanium graded porous structures manufactured by laser powder bed fusion, *J. Mech. Behav. Biomed. Mater.* 109 (2020) 103843.
- [4] P. Koehnen, C. Haase, J. Buelmann, S. Ziegler, J.H. Schleifenbaum, W. Bleck, Mechanical properties and deformation behavior of additively manufactured lattice structures of stainless steel, *Mater. Des.* 145 (2018) 205–217.
- [5] Y. Liu, J. Zhang, X. Gu, Y. Zhou, Y. Yin, Q. Tan, M. Li, M.X. Zhang, Mechanical performance of a node reinforced body-centred cubic lattice structure manufactured via selective laser melting, *Scr. Mater.* 189 (2020) 95–100.
- [6] X. Cao, S. Duan, J. Liang, W. Wen, D. Fang, Mechanical properties of an improved 3D-printed rhombic dodecahedron stainless steel lattice structure of variable cross section, *Int. J. Mech. Sci.* 145 (2018) 53–63.
- [7] A. Suzuki, K. Sekizawa, M. Liu, N. Takata, M. Kobashi, Effects of heat treatments on compressive deformation behaviors of lattice-structured AlSi10Mg alloy fabricated by selective laser melting, *Adv. Eng. Mater.* 21 (10) (2019) 1900571.
- [8] C. Bonatti, Mohr, D, Large deformation response of additively-manufactured FCC metamaterials: From octet truss lattices towards continuous shell mesostructures, *Int. J. Plast.* 92 (2017) 122–147.
- [9] Q. Han, Y. Gu, S. Soe, F. Lacan, R. Setchi, Effect of hot cracking on the mechanical properties of Hastelloy X superalloy fabricated by laser powder bed fusion additive manufacturing, *Opt. Laser. Technol.* 124 (2020) 105984.
- [10] X. Cao, D. Xiao, Y. Li, W. Wen, T. Zhao, Z. Chen, Y. Jiang, D. Fang, Dynamic compressive behavior of a modified additively manufactured rhombic dodecahedron 316l stainless steel lattice structure, *Thin-Walled Struct* 148 (2020) 106586.
- [11] N. Takata, H. Kodaira, K. Sekizawa, A. Suzuki, M. Kobashi, Change in microstructure of selectively laser melted AlSi10Mg alloy with heat treatments, *Mater. Sci. Eng. A* 704 (2017) 218–228.
- [12] M. Liu, N. Takata, A. Suzuki, M. Kobashi, Development of gradient microstructure in the lattice structure of AlSi10Mg alloy fabricated by selective laser melting, *J. Mater. Sci. Tech.*

- 36 (2020) 106–117.
- [13] M. Liu, N. Takata, A. Suzuki, M. Kobashi, Effect of heat treatment on gradient microstructure of AlSi10Mg lattice structure manufactured by laser powder bed fusion, *Materials* 13 (2020) 2487.
- [14] International Organization for Standardization. *Metallic Materials-Ductility Testing-Compression Test for Porous and Cellular Metals*; ISO 13314; ISO; Geneva, Switzerland, 2011.
- [15] J. Haruyama, S. Sawai, T. Mizuno, T. Yoshimitsu, S. Fukuda, I. Nakatani, Exploration of lunar holes, possible skylights of underlying lava tubes, by smart lander for investigating moon (slim), *Trans. JSASS Aerospace Tech. Japan.* 10 (2012) 7–10.
- [16] K. Kitazono, Design of impact energy absorbing system based on porous aluminum, *J. Jpn. Inst. Light Met.* 67 (2017) 559–563.
- [17] A.M. Vilardell, A. Takezawa, A. du Plessis, N. Takata, P. Krakhmalev, M. Kobashi, I. Yadroitsava, I. Yadroitsev, Topology optimization and characterization of Ti6Al4V ELI cellular lattice structures by laser powder bed fusion for biomedical applications, *Mater. Sci. Eng. A* 766 (2019) 138330.
- [18] O. Al-Ketan, R. Rowshan, R.K.A. Al-Rub, Topology-mechanical property relationship of 3D printed strut, skeletal, and sheet based periodic metallic cellular materials, *Addit. Manuf.* 19 (2018) 167–183.
- [19] M. Zhao, D.Z. Zhang, F. Liu, Z. Li, Z. Ma, Z. Ren, Mechanical and energy absorption characteristics of additively manufactured functionally graded sheet lattice structures with minimal surfaces, *Int. J. Mech. Sci.* 167 (2020) 105262.
- [20] D.S. Al-Saedi, S.H. Masood, M. Faizan-Ur-Rab, A. Alomarah, P. Ponnusamy, Mechanical properties and energy absorption capability of functionally graded F2BCC lattice fabricated by SLM, *Mater. Des.* 144 (2018) 32–44.
- [21] Y. Amani, S. Dancette, P. Delroisse, A. Simar, E. Maire, Compression behavior of lattice structures produced by selective laser melting: X-ray tomography based experimental and finite element approaches, *Acta Mater.* 159 (2018) 395–407.
- [22] L. Yang, C. Yan, W. Cao, Z. Liu, B. Song, S. Wen, C. Zhang, Y. Shi, S. Yang, Compression–compression fatigue behaviour of gyroid-type triply periodic minimal surface porous structures fabricated by selective laser melting, *Acta Mater.* 181 (2019) 49–

66.

- [23] M. Mazur, M. Leary, S. Sun, M. Vcelka, D. Shidid, M. Brandt, Deformation and failure behaviour of Ti-6Al-4V lattice structures manufactured by selective laser melting (SLM), *Int. J. Adv. Manuf. Technol.* 84 (5) (2016) 1391–1411.
- [24] L. Xiao, W. Song, C. Wang, H. Liu, H. Tang, J. Wang, Mechanical behavior of open-cell rhombic dodecahedron Ti-6Al-4V lattice structure, *Mater. Sci. Eng. A* 640 (2015) 375–384.
- [25] Z. Ma, D.Z. Zhang, F. Liu, J. Jiang, M. Zhao, T. Zhang, Lattice structures of Cu-Cr-Zr copper alloy by selective laser melting: Microstructures, mechanical properties and energy absorption, *Mater. Des.* 187 (2020) 108406.
- [26] S. McKown, Y. Shen, W.K. Brookes, C.J. Sutcliffe, W.J. Cantwell, G.S. Langdon, G.N. Nurick, M.D. Theobald, The quasi-static and blast loading response of lattice structures, *Int. J. Impact. Eng.* 2008, 35, 795–810.
- [27] T. Zhong, K. He, H. Li, L. Yang, Mechanical properties of lightweight 316L stainless steel lattice structures fabricated by selective laser melting, *Mater. Des.* 181 (2019) 108076.

3. Understanding and suppressing shear band formation

3.1 Introduction

The shear band in lattice structures is formed by localized deformation of struts or sheets on a defined plane, which normally leads to the stress fluctuations in the plateau region, as indicated by the compressive behaviors of BCC and TO lattice structures in Chapter 2 and other reported studies [1-4]. However, the unstable stress due to shear band is detrimental to the energy-absorbing performance of lattice structures. The occurrence of shear band needs to be suppressed for a controllable stress level and good energy-absorbing capacity. The mechanical properties of used raw materials can influence the shear band formation in lattice structure. Van Hooreweder et al. [5] suggested that the Ti6Al4V lattice structures treated by stress relief and hot isostatic press exhibited higher ductility and plateau stress stability in comparison to the as-built lattice structure. Suzuki et al. [6] reported that the as-built AlSi10Mg alloy BCC lattice structure did not have plateau region because of the low ductility. The lattice structures heat-treated under different condition showed different frequency of shear bands and stress drops in plateau region. Other reported BCC lattice structures made of stainless steel displayed moderate deformation behavior without shear band formation [7-9]. Thus, the shear band formation can be avoided by using suitable raw material and/or by post-treatment. However, for the lattice structures without the occurrence of shear band regardless of used raw material, the understanding of the mechanism and the method to suppress shear band formation are required.

Investigations on the deformation behaviors including shear band formations in lattice structures have been reported. It is suggested that the diagonal bands in 45° direction to the compressive direction were observed in lattice structures to be similar to the damage mode of conventional solid materials subjected to uniaxial compression [10, 11]. Cutolo et al. [12] investigated the mechanical behavior of Ti6Al4V diamond lattice structures with <001>, <111> and <011> orientations, the shear bands plane inclined by 54°, 71° and 35° with respect to the horizontal plane indicated that the different unit cell orientations led to different shear band deformation patterns. Yang et al. [13] presented an analytic methodology to elucidate the propagation of strut deformation patterns of sandwiched BCC lattice structures. The experimental results validated the analytical calculations and indicated that the failure at the interfaces of parts exhibiting distinct elastic modulus was prone to occur. Li et al. [14]

investigated the influence of layer and cell number on the crushing behavior of sandwiched BCCZ lattice structures, indicating that the failure mode with shear band was significantly affected by the boundary constraint. Yang et al. [15] revealed that cracks were easy to initiate and propagate at the regions in struts with strong tensile stress concentrations, according to the experimental observation and FEA results of 316L Gyroid cellular structures. In Chapter 1, it is also demonstrated that the cracks relevant to shear band formation were initiated by localized tensile stress. Although the above-mentioned studies help to gain insights into shear band formation, the further investigations on the development process and mechanism, and preferential formation plane of shear band still need to be carried out.

The methods that can suppress the formation of shear band have been found in several literatures. The investigation by Liu et al. [16] on compressive behaviors of octet lattice structures demonstrated that the deformation of diagonal shear band was altered to horizontal crushing by oversizing the horizontal struts. Cao et al. [17] modified the struts of rhombic dodecahedron (RD) lattice structures by inducing a shape parameter. The increase in the shape parameter resulted in a transition from “V” to “I” shaped shear bands. Al-Saedi et al. [18] indicated that the graded F2BCC lattice structure exhibited higher energy absorption capacity with a layer-wise deformation pattern, in comparison to the uniform lattice structures accompanied by shear band occurrence. Pham et al. [19] suggested that the shear band in architected lattice structure was analogous to the dislocation behavior in crystal structure. The shear bands in lattice structures inspired by the hardening principles were restrained. The Hexa lattice structures in Chapter 2 exhibited moderate stress concentration and therefore no shear band occurred. However, these studies on suppressing shear band formation were limited to specific lattice structures. Versatile methods that can suppress shear band formation in various should be proposed.

In this chapter, the BCC lattice structure was selected to elucidate the process of shear band evolution. The commonly used BCC unit cell in lattice structure has the geometry with high simplicity and symmetry, which make it a suitable candidate to simply clarify the mechanism of shear band. The preferential formation plane of shear band was also investigated by the lattice structures with various types of unit cells. Furthermore, a simple method by modifying the struts to suppress shear band formation was proposed. All the lattice structures were manufactured by L-PBF processing using Al-12Si alloy powder. Their mechanical properties and deformation

behaviors were systematically investigated through full and interrupted compression test, X-ray CT scan, and FEM analysis.

3.2 Materials and methods

3.2.1 Design and manufacturing

A 3D Systems ProX DMP 200 (Rock Hill, USA) was used in this study for the L-PBF processing of lattice structures. The optimal building parameters of laser power, scan speed, layer thickness, and hatch distance were 191 W, 1.2 m/s, 30 μm , and 50 μm , respectively. The rotation angle between the powder layers was 90°. The L-PBF process was performed under argon gas atmosphere at room temperature. Gas-atomized Al–12Si alloy powder was served as a base material, as shown in **Fig. 3-1**.

To investigate the formation process of shear bands, the lattice structures with the same unit cell type and outline geometry to the BCC lattice structure in Chapter 2 were used here. The lattice structures with more complex unit cell types compared to BCC unit cell were selected to find out the preferential formation plane and direction of shear band. As shown in **Fig. 3-2**, differently orientated lattice structures with unit cells of combined BCC-cubic (BC) and FCC-cubic (FC), and octet truss (OT) were designed and fabricated. The difference between the BC and BCC lattice structures are the presence or absence of vertical and horizontal struts that make up the cubic. These lattice structures have cuboid geometry of approximately $35 \times 35 \times 42 \text{ mm}^3$, unit cell size of 4.2 mm, and strut radius of 0.3 mm. The $\langle 001 \rangle$, $\langle 110 \rangle$ and $\langle 111 \rangle$

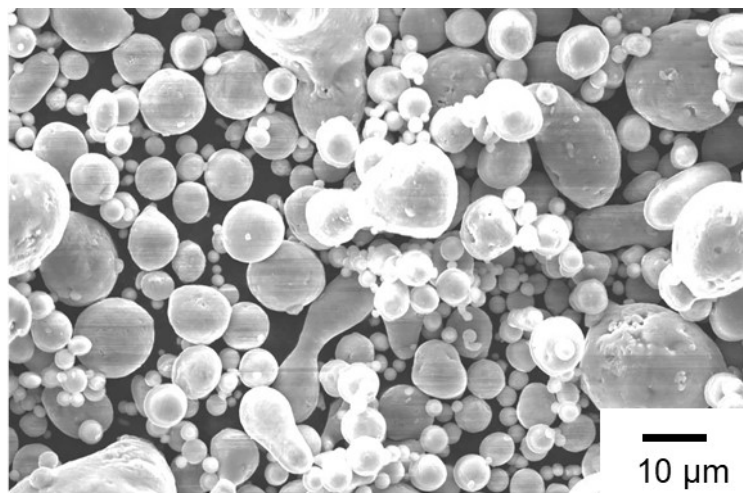


Fig. 3-1 SEM image showing Al–12Si gas-atomized powder for L-PBF manufacturing.

orientations aimed to investigate the influence of various loading directions on the preferential shear band plane and direction of lattice structures. For example, the lattice structure with BCC-cubic unit cells and $\langle 110 \rangle$ orientation, referred to as BC-110, were compressed in the

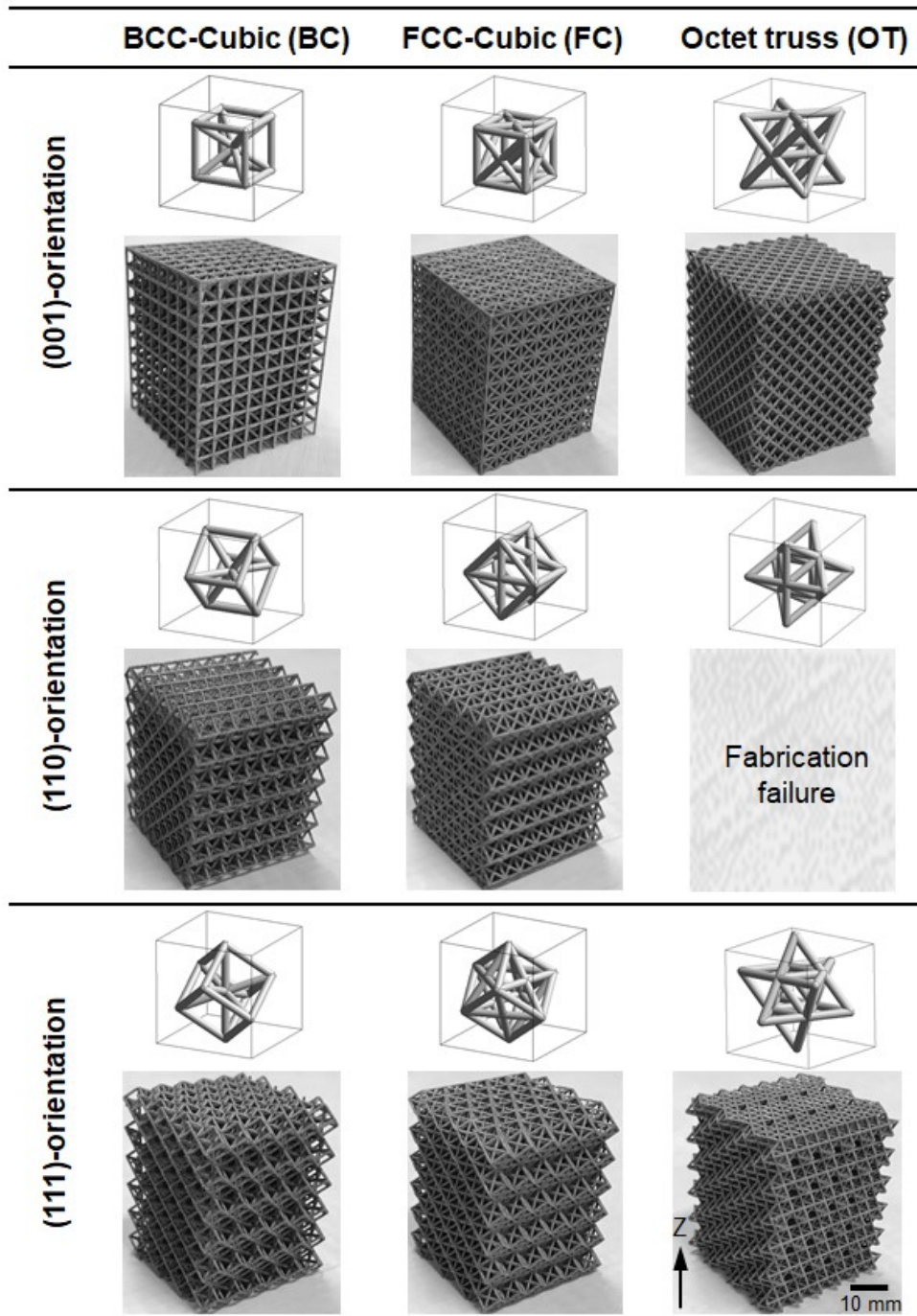


Fig. 3-2 Fabricated BCC-Cubic (BC), FCC-Cubic (FC), and Octet truss (OT) lattice structures with $\langle 001 \rangle$, $\langle 110 \rangle$ and $\langle 111 \rangle$ oriented unit cells.

<110> direction. The OT-110 lattice structure was not successfully fabricated.

Based on the understanding of shear band formation, the struts in BCC lattice structures were modified with a parameter R_d (the ratio of the radius) for the suppression of shear band. **Figure 3-3 (a)** shows the definition of R_d indicating the ratio of R_1 to R_2 , where R_1 is the strut radius at the two ends and R_2 is the strut radius at the center. Accordingly, the designed BCC unit cells with R_d equal to 0.5, 1, 2, 3, and 4 along with the corresponding manufactured lattice structures were shown in **Fig. 3-3 (b-f)**. These lattice structures have the same outline geometry

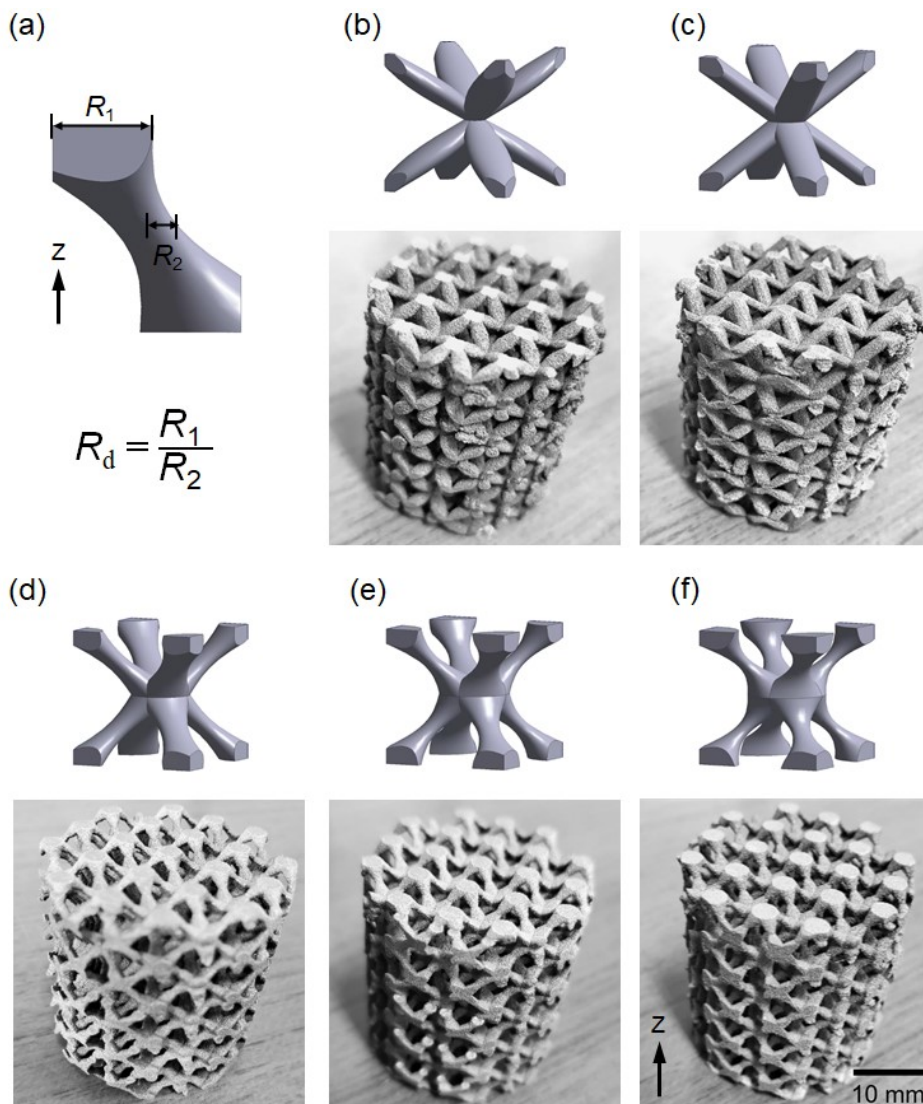


Fig. 3-3 (a) Illustration showing the definition of R_d , and fabricated BCC lattice structures with corresponding unit cell models of (b) $R_d = 0.5$, (c) $R_d = 1$, (d) $R_d = 2$, (e) $R_d = 3$, and (f) $R_d = 4$.

with the BCC lattice structure in Chapter 2, but different unit size of 6.3 mm due to the allowable strut radius according to the precision of applied L-PBF machine. In addition, the struts of BCC lattice structure for understanding shear band formation have R_d of approximately 2.3. The relative densities measured using the Archimedes' method for all the lattice structures used in this chapter were given in **Table 3-1**, in comparison to the designed values. The errors between the designed and measured relative densities were less than 5.5%. For the elimination of microstructural inhomogeneity and anisotropy generated in L-PBF fabricated specimens, a heat treatment under the condition of 530 °C for 6 hours was carried out, following by water quenching.

Table 3-1 Measured and designed relative density (the designed values are given in brackets) of different lattice structures.

Measured and designed relative density					
BCC				BC-001	0.134 (0.135)
				BC-110	0.122 (0.119)
				BC-111	0.112 (0.110)
BCC with R_d	0.5	0.212 (0.204)		FC-001	0.161 (0.163)
	1	0.211 (0.200)		FC-110	0.143 (0.146)
	2	0.198 (0.207)		FC-111	0.136 (0.134)
	3	0.197 (0.207)		OT-001	0.219 (0.215)
	4	0.198 (0.207)		OT-111	0.180 (0.182)

3.2.2 Mechanical tests and tomography

The compressive behaviors of lattice structures were investigated through quasi-static uniaxial compression experiments. The loading was applied by an Electronic Universal Testing Machine (capacity: 2.0×10^4 N) along the building direction. The interface between lattice specimens and loading plates was not lubricated. An initial strain rate of $2.2 \times 10^{-3} \text{ s}^{-1}$ was used. To characterize the step-by-step deformation behaviors of lattice specimens, the interrupted compressions and X-ray CT scan were repeatedly conducted at several stages of the compression process. A SKYSCAN 1275 (Bruker, Kontich, Belgium) with a voltage, current, and voxel size of 96 kV, 103 μA , and 18 μm , was applied for X-ray CT scan. The 3D models of

lattice specimens were established by reconstructing the two-dimensional (2D) projection images using NRecon (Bruker, Kontich, Belgium) software.

3.2.3 FEM analysis

FEM was conducted using Femtet 2019 (Murata Software, Tokyo, Japan). In order to save the calculation cost, reduced lattice models with $3 \times 3 \times 5$ unit cells were established for elasto-plastic analysis (**Fig. 3-4**). The relative density of each model was consistent with the corresponding lattice structure. The solid element of models was discretized by 4-node tetrahedron mesh. The mesh size of 0.2 mm was determined according to the convergence analysis of Mises stress generated in the struts and compressive stress–strain responses of lattice models. The input material properties, as given in **Table 3-2**, were obtained from the tensile tests of L-PBF manufactured Al–12Si bulk heat-treated at 530 °C for 6 h [20]. The forced displacement of 10% height of lattice models were implemented on the top plane along Z direction. The boundary conditions were same to those used in Chapter 2.

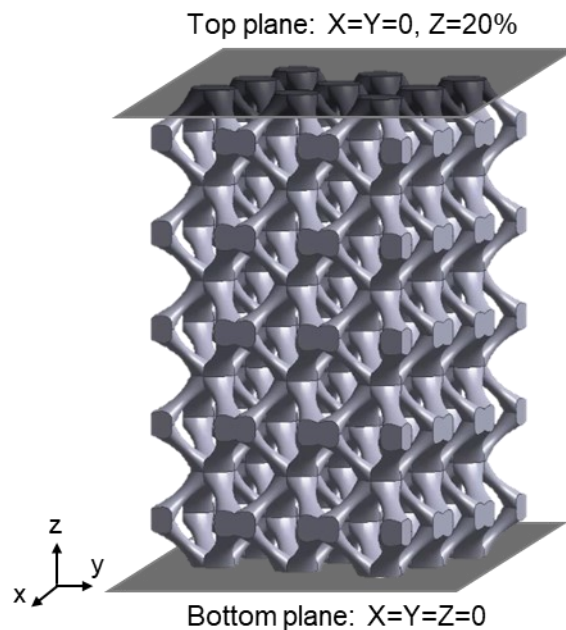


Fig. 3-4 An example of lattice model and applied boundary conditions for FEM analysis.

Table 3-2 Material properties applied for FEM analysis. These properties were obtained from the tensile tests of L-PBF manufactured Al–12Si bulk after the heat treatment at 530 °C for 6 hours.

Young's modulus, E / GPa	60
Poisson's ratio, ν	0.3
Yield stress, σ_{YS} / MPa	100
Work hardening coefficient, n	0.17

3.3 Results and discussion

3.3.1 Formation process of shear band

Figure 3-5 (a) illustrates the X-ray CT observations showing the cross-sections of BCC lattice structure prior to compression and during compression at several nominal strains. The observed cross-section of (110) plane in BCC unit cell is illustrated in **Fig. 3-6 (b)**. **Fig. 3-6 (c)** shows the nominal stress–strain responses of the interrupted compressions. As the overall images shown in **Fig. 3-5 (a)**, the BCC lattice structure was generally deformed to a barrel shape. At the nominal strains of 9.7% (before stress drop) and 12.3% (just after stress drop), preferential deformation occurring at the central unit cells was observed. At the nominal strain of 14.7% (during stress drop), obvious shear band generated diagonally throughout the lattice structure as marked by the red broken lines in the overall image. After the appearance of shear band, the fractured struts were still observed in the cross-sectional (110) plane, suggesting that the shear band in BCC lattice structure was formed along the $\langle 111 \rangle$ direction as illustrated in **Fig. 3-6 (b)**. Therefore, the family of shear band in BCC lattice structure is $\{110\} \langle 111 \rangle$, which corresponds to one of the slip systems of the BCC crystal structure. It was reported in literatures that the direction of shear band was the same to the maximum shear stress direction of 45° . However, the angle between $\langle 111 \rangle$ direction and the loading axis is approximately 54.7° . The $\{110\} \langle 111 \rangle$ shear band in BCC lattice structure indicates that the direction of shear band does not always form at constant 45° diagonal direction. In the enlarged local images, a crack initiated at the region of strut near node at 9.7% nominal strain. When the lattice structure was compressed to 12.3%, more cracks were initiated and propagated, resulting in preferential deformations of the cracked struts. At the nominal strain of 14.7%, preferentially propagated

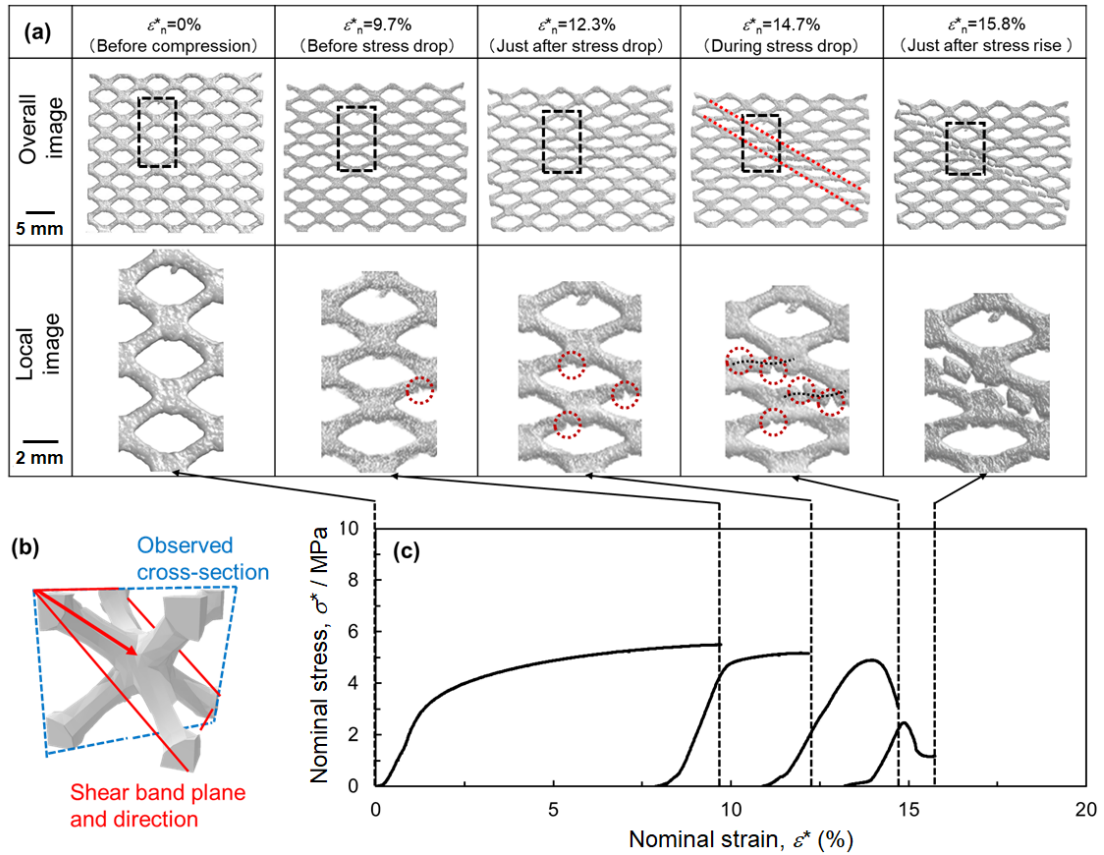


Fig. 3-5 (a) X-ray CT images showing cross-sections of lattice structure before compression and compressed at different strains. (b) Schematic illustration showing the observed cross-section and shear band plane and direction. (c) Interrupted compressive stress–strain curves showing the stop and restart point in the observation of shear band formation process.

cracks were located on the diagonal plane including the position of the first generated crack. These struts with cracks bended in S-shaped behavior, where the cracks present at the tensile stressed region of the deformed struts. With further compression to 15.8% (just after stress rises again), severe crack propagation and strut failure were observed. The upper and lower struts on the shear band contacted each other, subsequently the nominal stress increased again. Thus, the crack initiation in struts close to nodes triggered the shear band formation.

Figure 3-6 shows the experimental and numerical stress–strain curves of BCC lattice structure. The elastic modulus and yield strength were overpredicted by the simulation results, due to the established ideal model without geometry imperfection. The stress–strain curves of experiment and simulation show similar variation tendency, indicating that the FEM results are reliable to estimate the mechanical behavior of the BCC lattice structure at early plastic stage.

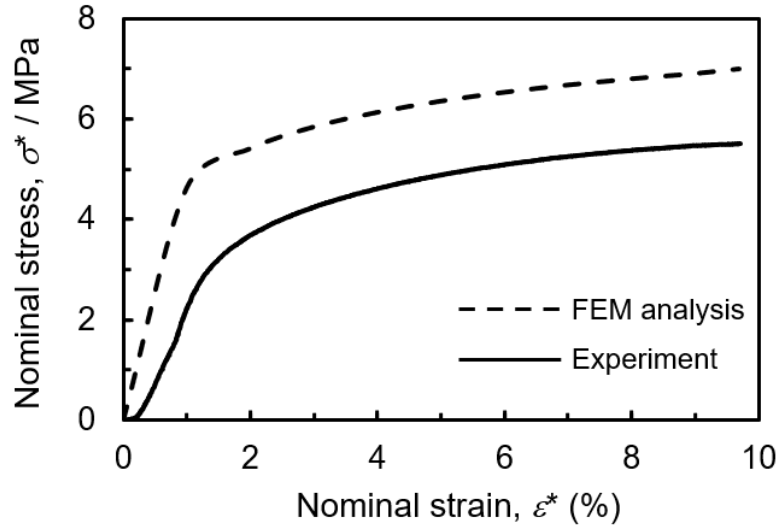


Fig. 3-6 Experimental and numerical stress–strain curves of BCC lattice structure.

Figure 3-7 (a-c) presents the von Mises stress distributions in the cross-sections of BCC lattice model at the nominal strains of (a) 1%, (b) 5%, and (c) 10%. The lattice model exhibited deformation of barrel shape, due to restrained X and Y in all degree of freedom on the top and bottom planes. As a result, the central unit cells of the lattice model deformed preferentially. The deformation behavior coincided well with cross-sectional images obtained by X-ray CT scan (**Fig. 3-5 (a)**). The square-dotted region showing local Mises stress distribution in **Fig. 3-7 (c)** is magnified and shown in **Fig. 3-7 (d)**. The arrow marked regions in the struts close to nodes suffered high stress concentration. **Figure 3-7 (e)** and **(f)** show the maximum-minimum principal stress distribution in cross-sections and enlarged local region. The size of the vector arrows indicates the relative value of the associated principal stress on strut surfaces. The tension and compression are illustrated in red and blue arrows, respectively. As shown in **Fig. 3-7 (f)**, the stress vectors on the struts were distributed in S-shaped behavior. High principal stress in tension generated at the convex as arrow marked region (**Fig. 3-7 (f)**), where the Mises stresses were also high (**Fig. 3-7 (d)**). This region exhibiting high Mises stress and principal stress in tension correlated to the cracks initiation positions in **Fig. 3-5 (a)**. Therefore, the localized tensile stress on bended struts leads to the initiation of cracks. Parallel results have also been found in literatures [6, 15, 21, 22].

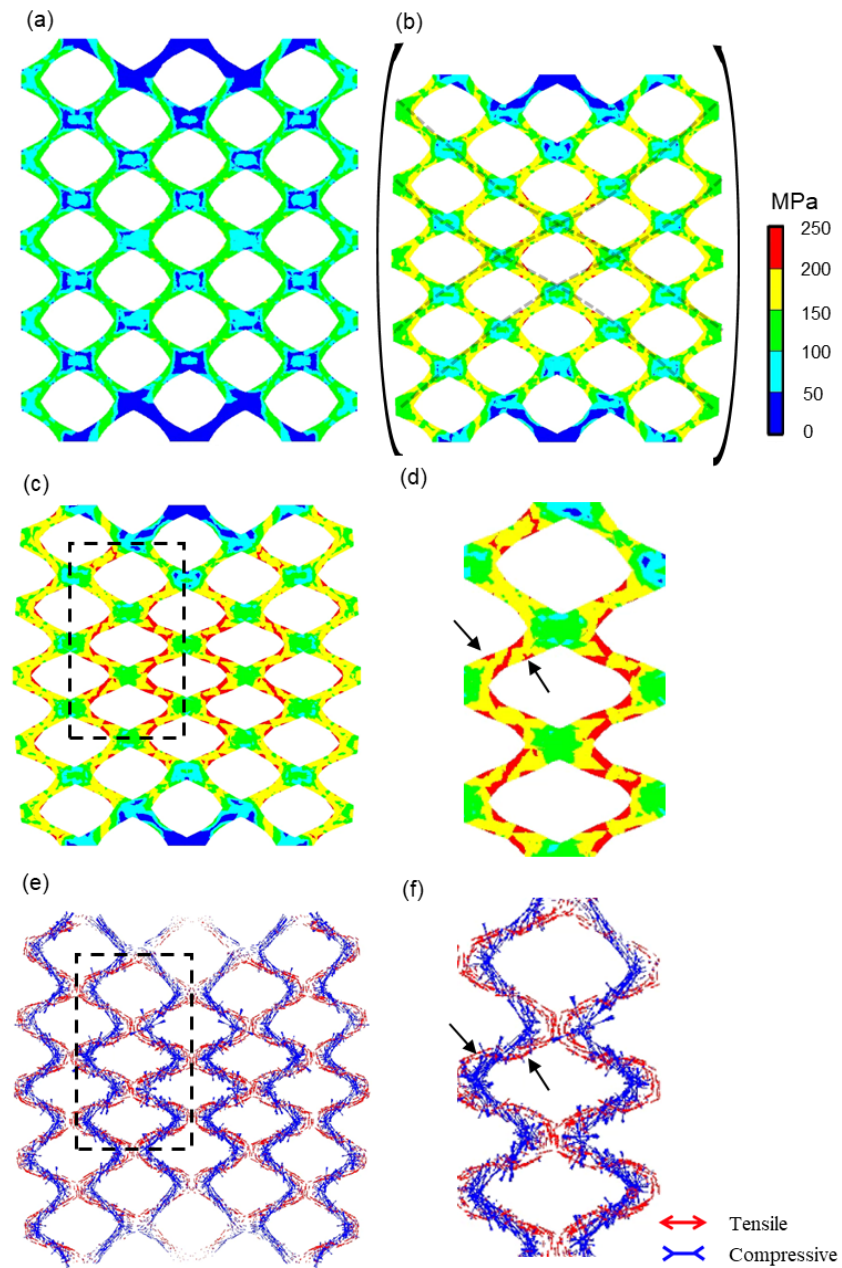


Fig. 3-7. Distributions of (a-d) von Mises stress and (e, f) principal stress in lattice model at nominal strains of (a) 1%, (b) 5%, and (c-f) 10%. The stress distributions in dotted squares in (c, e) are enlarged in (d, f).

Based on the above elucidation, the formation process of shear band of the BCC lattice structure is given in the flow chart, as shown in **Fig. 3-8**. Under compression, the lattice

structure exhibits a barrel-shaped deformation (**Figs. 3-5 (a)** and **3-7 (b)**). The unit cells at the center region preferentially experience large bending deformation (**Figs. 3-5 (a)** and **3-7 (c)**), which lead to the stress concentration at the bended struts in the vicinity of nodes (**Fig. 3-7 (d)**). Consequently, the crack is first generated at the convex region with localized tensile stress in a bended strut. Then, multiple cracks are initiated in the struts parallel to the initially cracked strut. Many crack generations and propagations significantly degrade the deformation resistance of the specific plane and direction ($\{110\} \langle 111 \rangle$ in BCC lattice structure), resulting in the shear band formation (**Fig. 3-5 (a)** and **(c)**). After that, the upper unit cells near the shear band contact the lower ones, and the lattice structure resumes to carry load (**Fig. 3-5 (a)** and **(c)**). It is suggested that other strut-based lattice structures exhibiting the bending deformation of struts may also have similar evolution process of shear band. In fact, cracks were observed in strut-based Kelvin, octet-truss, and TO (in Chapter 2) lattice structures experiencing shear bands under compression [23]. These results also indicate the shear band formation was related to the crack initiations.

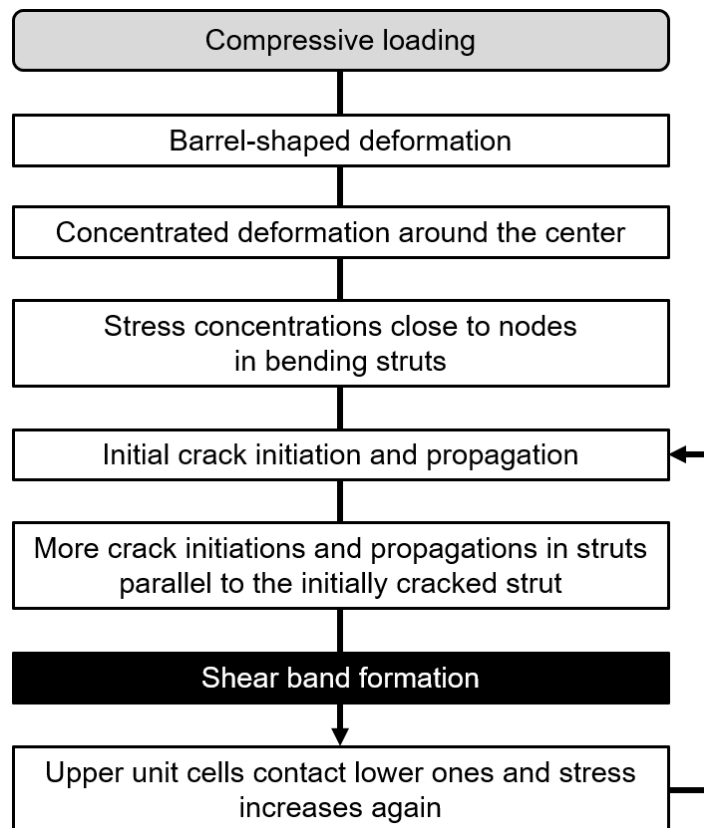


Fig. 3-8 Flow chart of shear band formation process.

The shear band plane and direction were $\{110\} \langle 111 \rangle$ in the BCC lattice structure, which can be attributed to less struts in this family capable to resist deformation. When the shear band formation is on the $\{110\} \langle 111 \rangle$ family, external loads on BCC lattice structure need to fracture two struts per unit cell. Assuming that shear band was formed in a 45° diagonal plane and direction, that is the family of $\{110\} \langle 110 \rangle$, four struts can resist deformation along this direction, indicating less tendency of shear band formation compared to the $\{110\} \langle 111 \rangle$ family. In the BCC crystal structure, the close-packed plane and direction of atoms present on $\{110\} \langle 111 \rangle$. For the architected BCC unit cell imitating BCC crystal structure, the first nearest-neighbor lattice points are connected by struts, thus struts are present the most densely on the $\{110\} \langle 111 \rangle$ family. This result implies a possibility that shear band would form in the densest plane and direction of struts with the smallest deformation resistance. In that case, the family of shear band in lattice structure may correspond to the slip system of the crystal structure, although the investigation on other crystal-inspired lattice structures needs to be conducted. For common lattice structures with various arrangement of struts, the preferential formation plane and direction of shear band are investigated in the next section.

3.3.2 Preferential formation plane and direction of shear band

The interrupted compression tests and X-ray CT scan were alternatively carried out on the BCC-cubic (BC) and FCC-cubic (FC), and octet truss (OT) lattice structures with $\langle 001 \rangle$, $\langle 110 \rangle$ and $\langle 111 \rangle$ orientations. The interrupted stress–strain curves and X-ray CT cross-sectional images showing the deformation behaviors of all the lattice structures are presented in **Figs. 9-11**. The observed cross-sections parallel to the loading direction and shear band plane and direction (if occurred) were also illustrated. In the case of BC lattice structures (**Fig. 3-9**), the densest plane with the most struts is present on $\{110\}$ in BC unit cell. It was clearly observed that a diagonal shear band was formed on the (110) plane along the $\langle 110 \rangle$ direction in BC-001 (**Fig. 3-9 (a)**), which is the same as the shear band occurred in the BCC lattice structure. For the BC-110 lattice structure, the densest (110) plane was parallel or perpendicular to the loading direction, and no shear band was identified (**Fig. 3-9 (b)**). The first stress drops were due to the failure of unit cells at bottom layer rather than the shear band formation. The BC-110 lattice structure experienced crushing deformation behavior in a layer-by-layer manner. For the BC-111 lattice structure, shear band was also formed on the densest (110) plane along the $\langle 110 \rangle$

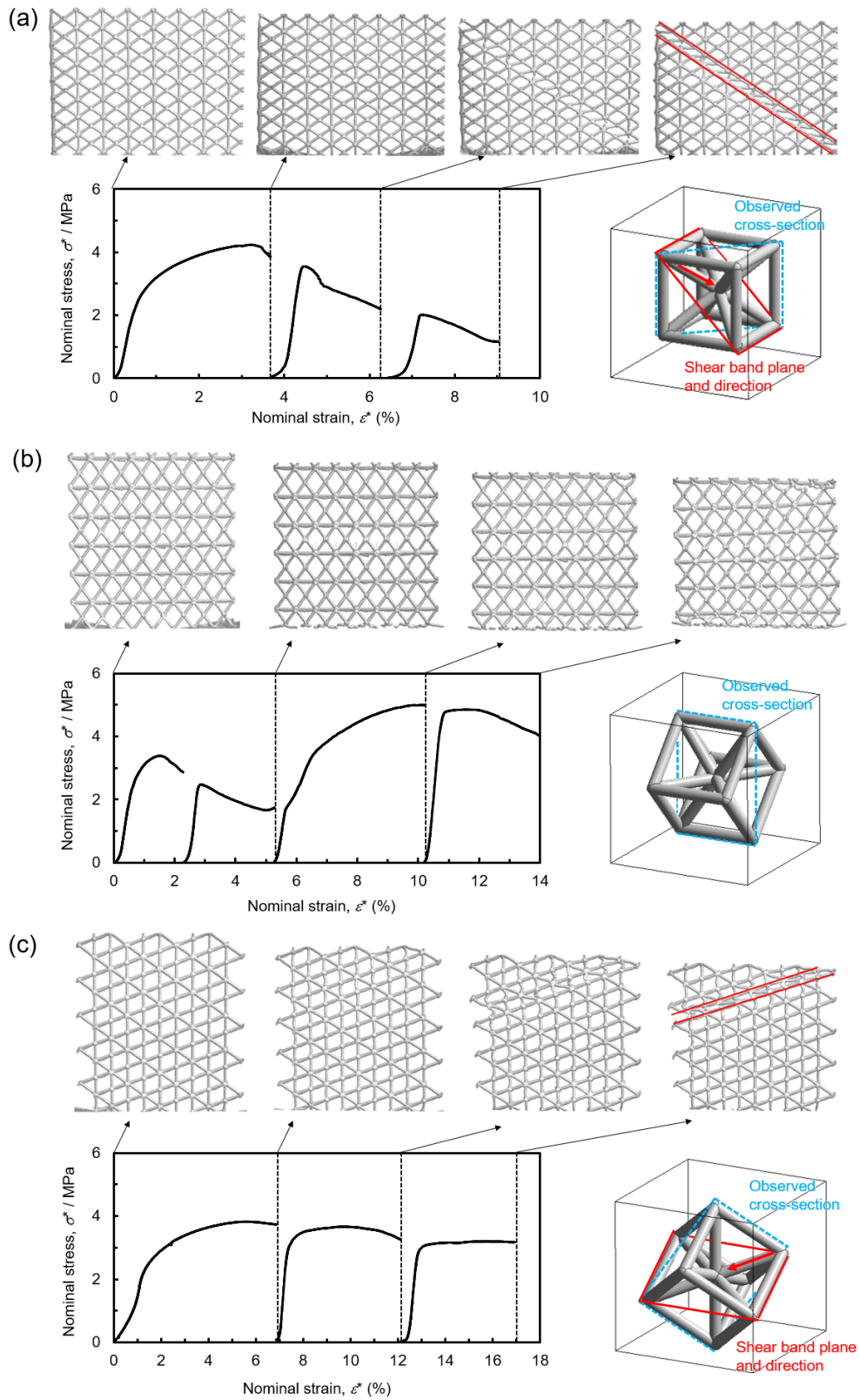


Fig. 3-9 Cross-sectional images observed by X-ray CT scan showing deformation behavior of BCC-cubic (BC) lattice structures with (a) $\langle 001 \rangle$, (b) $\langle 110 \rangle$, and (c) $\langle 111 \rangle$ orientation.

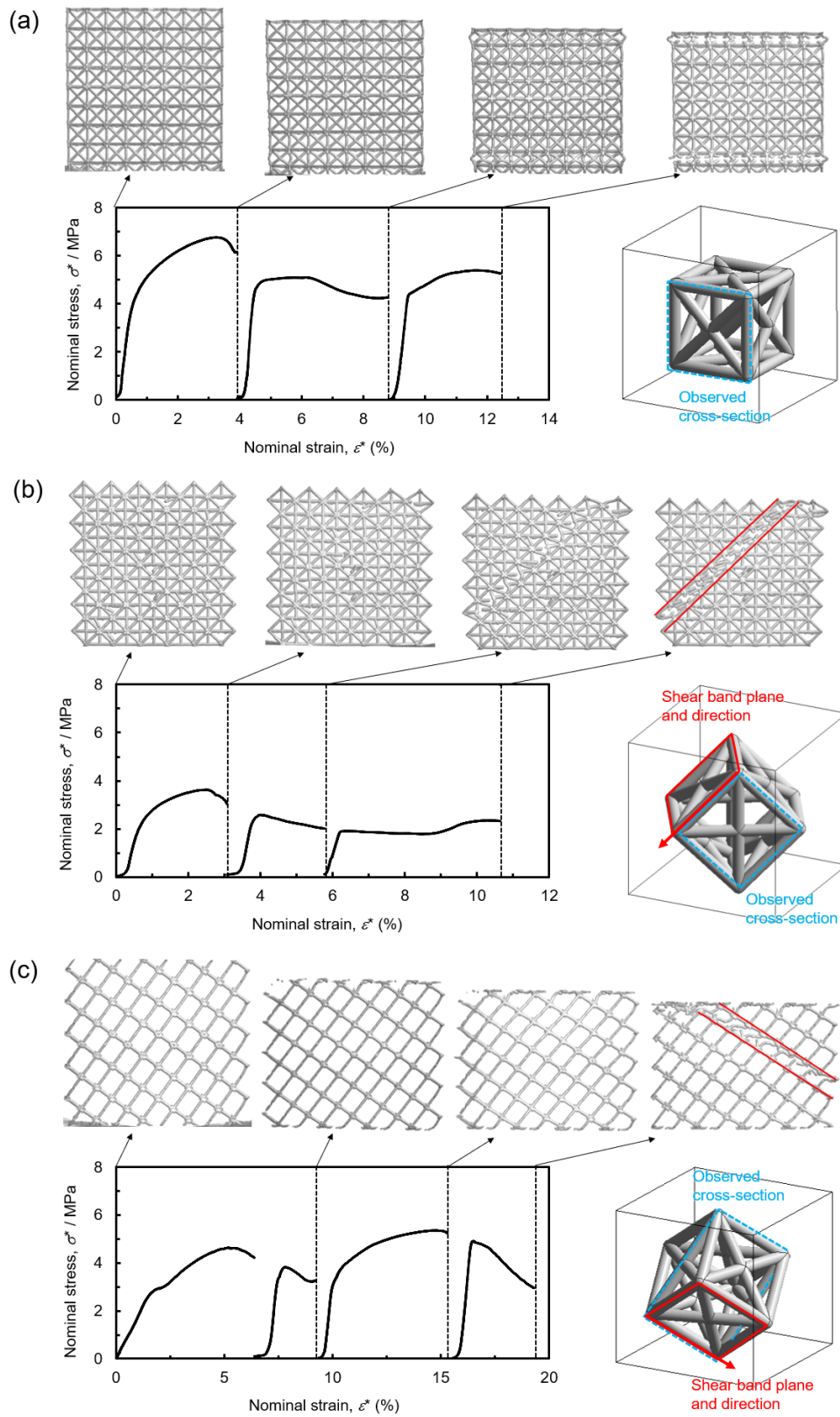


Fig. 3-10 Cross-sectional images observed by X-ray CT scan showing deformation behavior of FCC-cubic (FC) lattice structures with (a) $\langle 001 \rangle$, (b) $\langle 110 \rangle$, and (c) $\langle 111 \rangle$ orientation.

direction (**Fig. 3-9 (c)**). It is worthy of being noted that the stress was slightly degraded and relatively stable, compared to the drastic stress drop in BC-001 lattice structure with shear band formation. As for the FC lattice structures shown in **Fig. 3-10**, the densest plane is $\{001\}$, where shear band is prone to occur based on the results of BCC and BC lattice structures. In fact, the shear bands were formed on the (100) plane along the $\langle 100 \rangle$ direction in FC-110 (**Fig. 3-10 (b)**) and FC-111 lattice structure (**Fig. 3-10 (c)**), at which this plane has the angle of neither 0 nor 90° with respect to the loading axis. In the case of FC-001 lattice structure (**Fig. 3-10 (a)**) with the densest (100) plane parallel to the loading direction, shear band was not formed and the structure was deformed by successively buckling or crushing the unit cells.

For the crystal-imitated lattice structures, according to the design strategy using struts to connect the first-nearest-neighbor lattice points, OT unit cell corresponds to the FCC crystal structure. The slip system in FCC crystal structure is $\{111\} \langle 110 \rangle$. In the OT-001 lattice structure (**Fig. 3-11**), observed shear band plane and direction were also $\{111\} \langle 110 \rangle$. This is ascribed to the low capacity of deformation resistance in the $\langle 110 \rangle$ direction on (111) plane, because shear deformation would be activated by fracturing the fewest struts (only 3 per unit cell). Parallel results are also reported in the studies on the deformation behavior of octet-truss lattice structure [23, 24]. This result supports the suggestion that shear band in architected lattice structure is in accordance with the slip system of the corresponding crystal structure. In addition, shear band was not observed in the OT-111 lattice structure because of the existence of perpendicularly oriented densest planes to the loading direction. Based on the above results, the densest plane of struts and shear band formations in differently oriented BC, FC, and OT lattice structures were summarized in **Table 3-3**. It is confirmed that shear band is preferentially formed on the densest plane including the most struts when the loading axis is not parallel or perpendicular to this plane. The reason of the preferential formation directions of shear band in BC and FC lattice structures is not clear, due to the strut variety in BC and FC unit cells with distinct orientation angles and aspect ratios compared to the simple BCC and TO unit cells with high symmetry. Additionally, the effect of loading orientations with various angles on the shear band formation are not sufficiently understood. For instance, the transition angle between the densest plane and loading axis determining appearance or absence of shear band needs to be clarified.

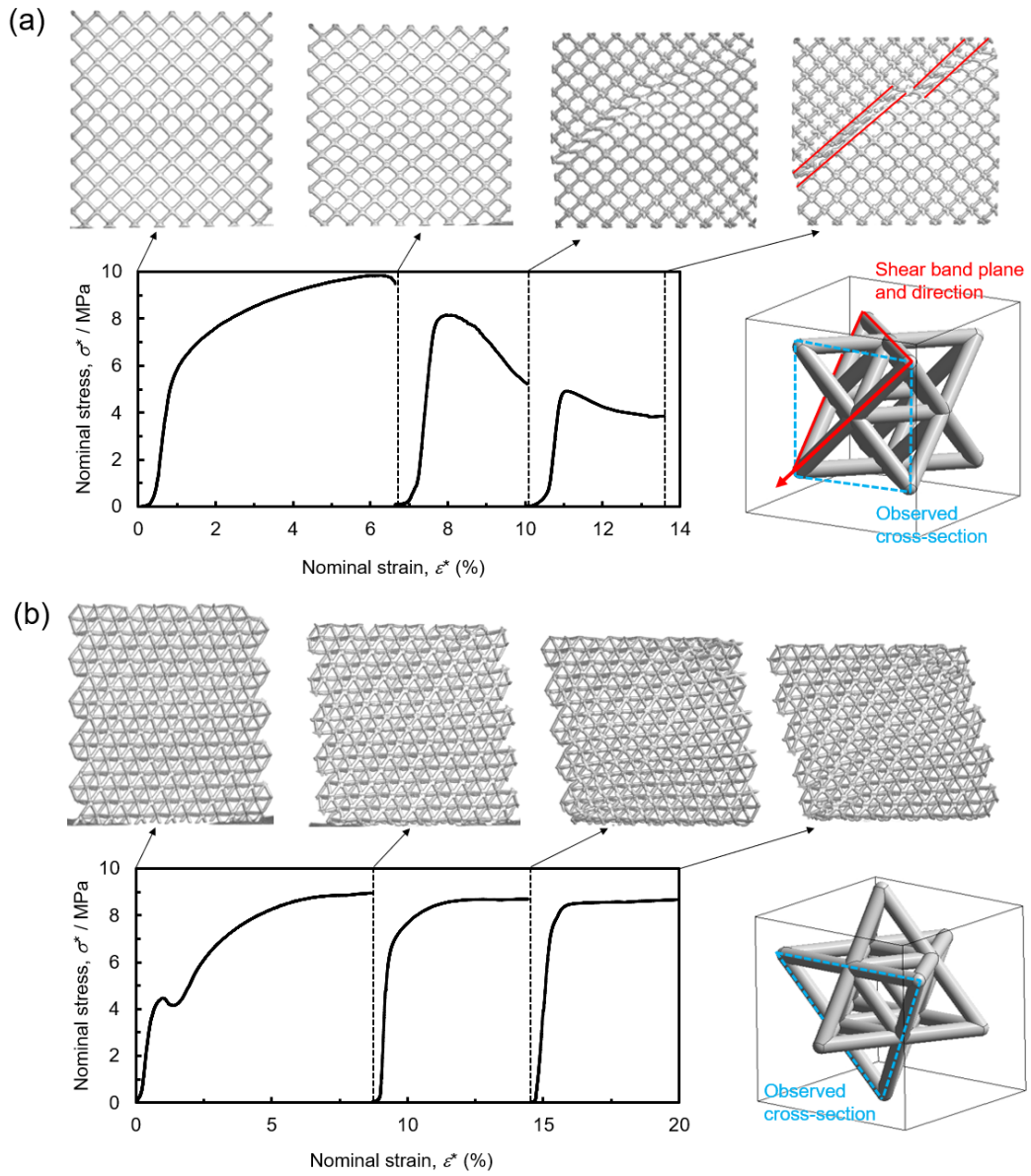
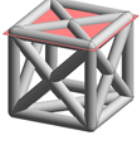
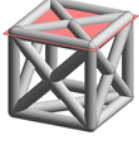


Fig. 3-11 Cross-sectional images observed by X-ray CT scan showing deformation behavior of Octet truss (OT) lattice structures with (a) $\langle 001 \rangle$ and (b) $\langle 110 \rangle$ orientation.

Table 3-3 The densest plane of struts and shear band formations in BC, FC, and OT lattice structures with different orientations.

Lattice structure	Densest plane of struts	Shear band occurrence	Shear band plane	Shear band direction	
BC	001	$\{110\}$	Yes	(110)	$\langle 111 \rangle$
	110		No	/	/
	111		Yes	(110)	$\langle 111 \rangle$
FC	001	$\{001\}$	No	/	/
	110		Yes	(001)	$\langle 100 \rangle$
	111		Yes	(001)	$\langle 100 \rangle$
OT	001	$\{111\}$	Yes	(111)	$\langle 110 \rangle$
	111		No	/	/

3.3.3 Suppression of shear band formation

To prevent the appearance of shear band formation, lattice structures can be oriented with the densest plane of struts parallel or perpendicular to the loading direction. However, the method to suppress shear band formation in a common case that the loading directions are not parallel or perpendicular to the densest plane of struts still needs to be explored. This is because a load may be applied from various directions in actual shock absorbing components. The suppression of shear band can be achieved by hindering the occurrence of one of the steps during the formation process shown in **Fig. 3-8**. For instance, the relief of localized tensile stress on bended struts results in the restraint of crack initiations and propagations, which are the critical cause of shear band formation. Appropriate selection of unit cell type for lattice structures can realize relieved tensile stress. The investigation by Al-Ketan et al. suggested that the lattice structures with skeletal-based gyroid unit cell experienced no shear band formation, although shear bands were formed in the lattice structures with strut- and sheet-based unit cells. Additionally, the results in Chapter 2 indicated that the hexagon lattice structure exhibited more

moderate tensile stress concentration compared to the BCC and truncated octahedron lattice structures, leading to a deformation behavior without shear band formation in the hexagon lattice structure. Another possibly effect method to suppress shear band is strut shape modification. It is reported that the energy absorption capacity was improved by tapering struts of BCC lattice structure due to increased volume of plastically stressed region [25]. According to the compression test of RD lattice structure with modified struts, Cao et al. indicated that the struts modification offered different deformation behaviors and enhanced mechanical properties [26]. Thus, the modification of struts could lead to the suppression or promotion of shear band formation, because the stress in tension can be relaxed or further concentrated depending on re-distributed material in struts. In this section, the influence of strut shape on the mechanical property and deformation behavior (especially the shear band formation) of BCC lattice structures is discussed.

The strut shape is modified with R_d equal to 0.5, 1, 2, 3, and 4 in the unit cells of BCC lattice structures (**Fig. 3-3**). The nominal stress–strain responses of BCC lattice models with different R_d values obtained by FEM are shown in **Fig. 3-11**. With an increase in the R_d value, the compressive strength increased and then decreased when R_d value was 3. The lattice model with R_d equal to 2 exhibits the highest strength. The tendency of the stress–strain curves is consistent with the reported results [25].

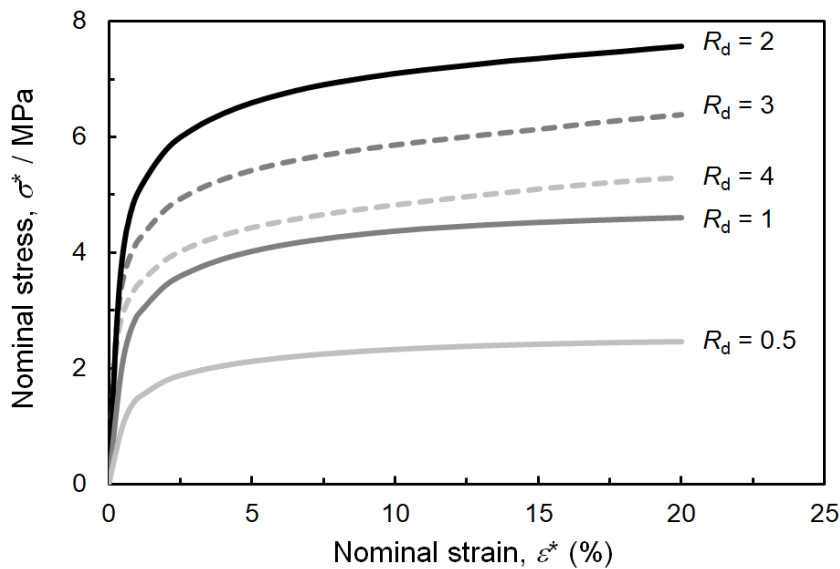


Fig. 3-11 Stress–strain responses of BCC lattice models with different R_d obtained by FEM.

Figure 3-12 shows Mises stress distribution in (110) cross-sections and unit cells in BCC lattice models with different R_d at 10% nominal strain. For the lattice model with R_d equal to 0.5, the Mises stresses are highly concentrated on nodes, and low Mises stresses are spread in struts. With an increase in the R_d value, the node regions under high Mises stress are gradually shifted to the struts, as a result of increased material volume of node region and decreased material volume of strut region. In the lattice model with R_d equal to 2, the distributed Mises stresses are more uniform compared to the other structures. The histograms showing the frequency of Mises stress distributed in struts with different R_d value are present in **Fig. 3-12**. The colors in the histograms correspond to those of the contour maps in lattice models and unit cells. When R_d is equal to 2, almost all the Mises stresses are in the range of 150~250 MPa, indicating uniform stress distribution. However, other lattice models show more dispersed stress distribution, and relatively low Mises stress under 150 MPa have high frequency. Therefore, the lattice model with R_d equal to 2 exhibits uniform and high stress distribution, which result in larger compressive strength simulated by FEM analysis in **Fig. 3-11**.

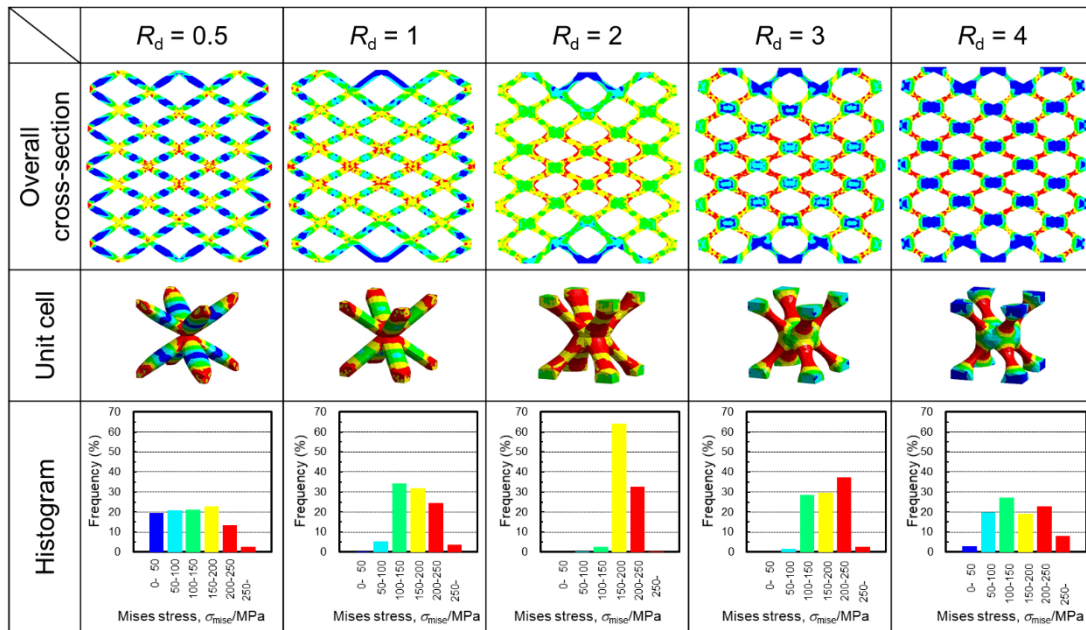


Fig. 3-12 von Mises stress distribution in lattice models and unit cells with different R_d at 10% nominal strain.

Figure 3-13 shows strut deformation behavior in lattice models with different R_d when compressed at 5% and 20% nominal strains. When R_d is equal to 0.5 and 1, the struts deform in a pin-joint like behavior, barely experience bending deformation. With an increase in the R_d value, the struts in unit cells suffer more significant S-curved bending deformation behavior. Typically, the lattice structures are compressively deformed by bending, stretching or buckling the struts. Local buckling behavior normally occurs when the struts are consecutively oriented in the loading direction (**Figs. 3-9 (a, c) and 10 (a)**). Maxwell's stability criterion is simply used to characterize whether a lattice structure is under bending- or stretching-dominated deformation behavior (as indicated in Chapter 1). In this section, in order to further distinguish the different deformation behavior of the bending-dominated BCC lattice structures with different R_d value, a concept of node- and strut-dominated deformation behavior is proposed. When high Mises stress is concentrated on node region, the structure is denoted as node-dominated. Conversely, when high Mises stress is concentrated on strut region rather than node, the structure is denoted as strut-dominated.

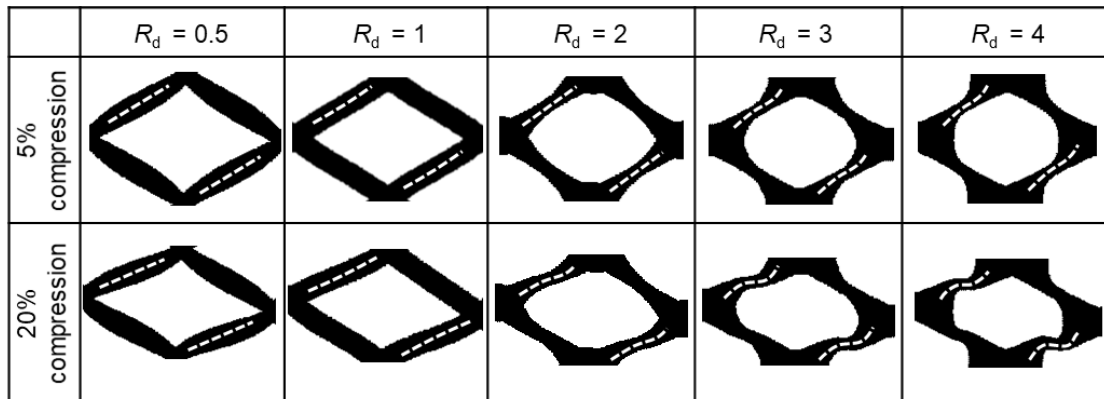


Fig. 3-13 Strut deformation behavior in lattice models with different R_d at 5% and 20% compression.

The cracks are prone to occur at the tensile stressed region in struts with high Mises stress concentration. **Figure 3-14 (a)** presents the relationship between the maximum value of Mises stress at the tensile stressed region in struts and the nominal strain, in order to compare the tendency for crack initiation in the lattice models with different R_d . As the R_d increases, the maximum values of Mises stresses at the arrow-marked region largely increase, the value with R_d equal to 2 is approximately 1.8 times higher than that with R_d equal to 0.5. Therefore, the

struts with smaller R_d value exhibit less potential for crack occurrence, which suggests that the modified struts with smaller R_d value can suppress the shear band formation. **Figure 3-14 (b)** shows the relationship between the maximum value of Mises stress at the tensile stressed region in struts and R_d value at 10% nominal strain. The maximum Mises stress substantially increase

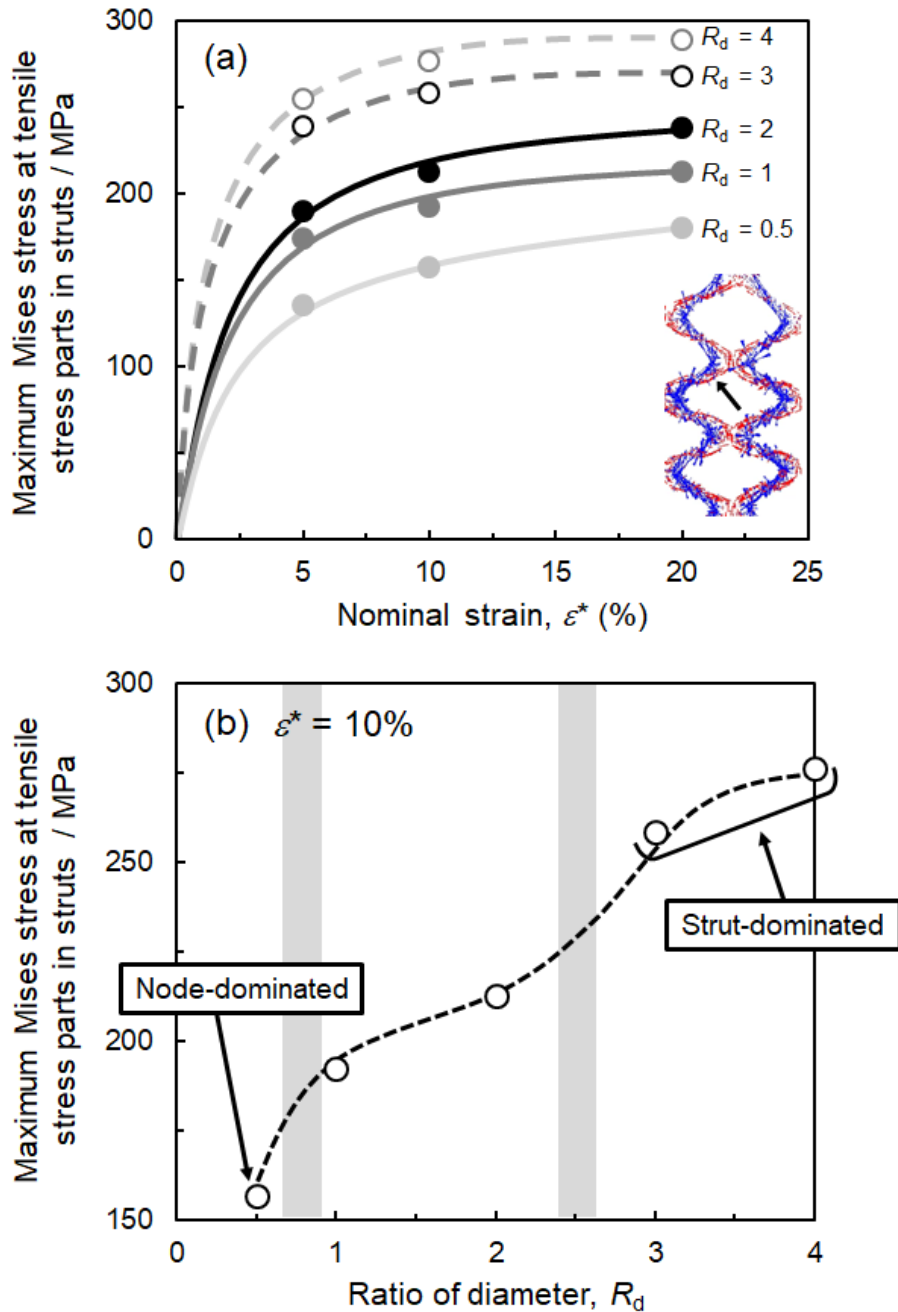


Fig. 3-14 Changes in maximum Mises stress at tensile stressed region in struts as a function of (a) the nominal strain of lattice model and (b) ratio of diameter (R_d) at 10% compression.

with the R_d from 0.5 to 1 and from 2 to 3. The lattice model with R_d equal to 0.5 exhibits node-dominated deformation behavior and hardly bending behavior (Figs. 3-12 and 13), thus the Mises stress at the tensile stress region in the struts is low. In the case of R_d equal to 3 and 4, the struts in the lattice models are bended in a strut-dominated deformation behavior. The severely bended struts lead to Mises stress concentration and high tendency for crack initiation (Figs. 3-12 and 13).

Figure 3-15 illustrates (a) X-ray CT images showing local cross-sections of lattice structures, and (b) the relationship between the relative diameters of struts with different

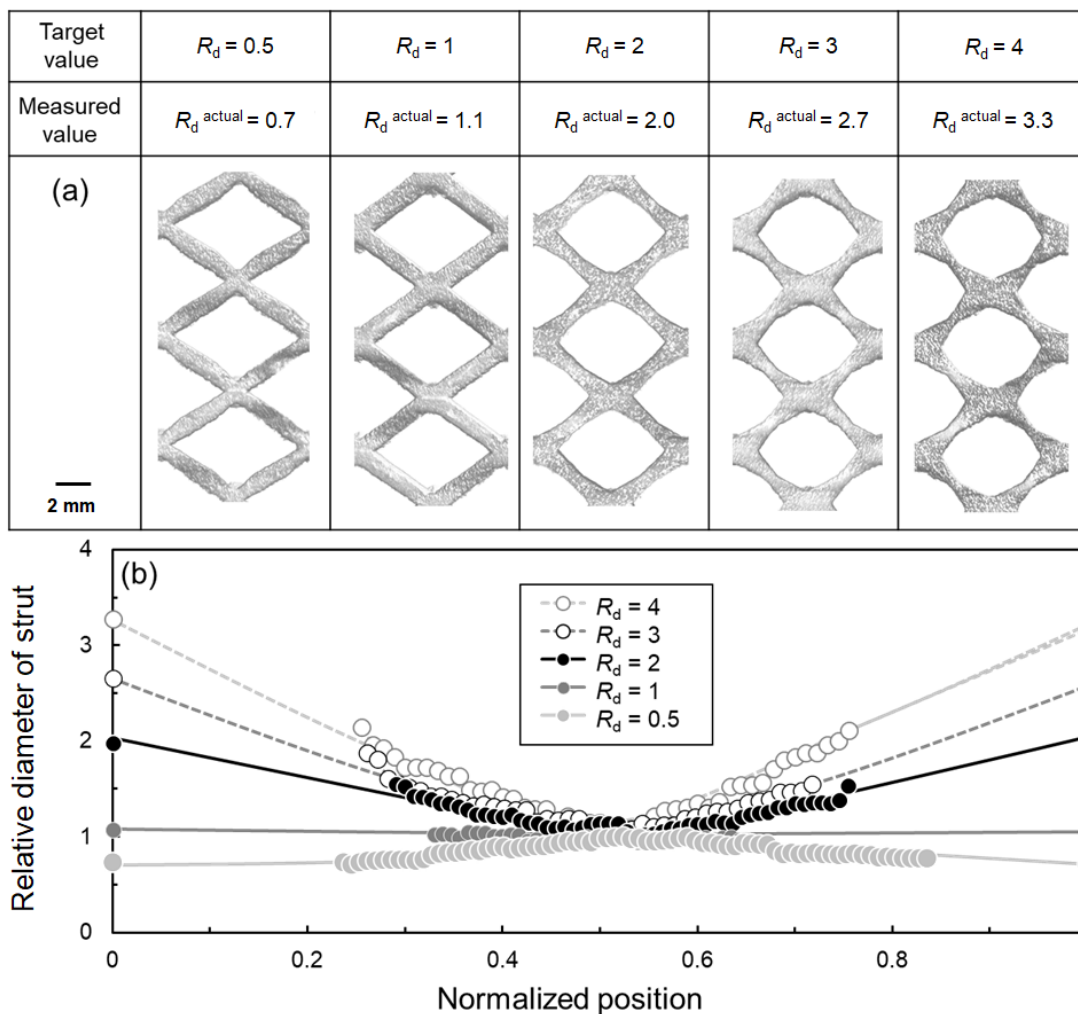


Fig. 3-15 (a) X-ray CT images of lattice structures with different R_d and (b) change in relative diameter of strut as a function of normalized position. The normalized positions of 0 and 1 indicate node, and that of 0.5 indicates the center of strut. The relative diameter of struts was defined as struts diameters divided by those at the normalized positions of 0.5.

designed R_d and normalized position. The normalized positions of 0 and 1 mean node, and those of 0.5 mean the center of strut. The diameters of struts are normalized by those at the normalized positions of 0.5. The relative diameter at the normalized positions of 0 and 1 means the actual R_d (denoted as R_d^{actual}). For the designed R_d of 0.5, 1, 2, 3, and 4, the values of R_d^{actual} are 0.7, 1.1, 2.0, 2.7, and 3.3, respectively. The R_d^{actual} is close to the designed value in the case of R_d equal to 1 and 2. However, the R_d^{actual} is obviously larger or smaller than the designed R_d , in the case that R_d is equal to 0.5, 3 and 4 and the regions with small diameter exist in the unit cells. This is caused by the accuracy of the applied L-PBF process.

Figure 3-16 presents the SEM images and optical micrographs of representative lattice structures with R_d^{actual} equal to 0.7 and 2.7. Both lattice structures have the thin parts at node or struts. The relative densities were analyzed by measuring the area fraction of pores using binary images converted from optical micrographs. The quantified relative densities of the L-PBF produced lattice structures with R_d^{actual} equal to 0.7 and 2.7 are above 98.8% and 99.3%,

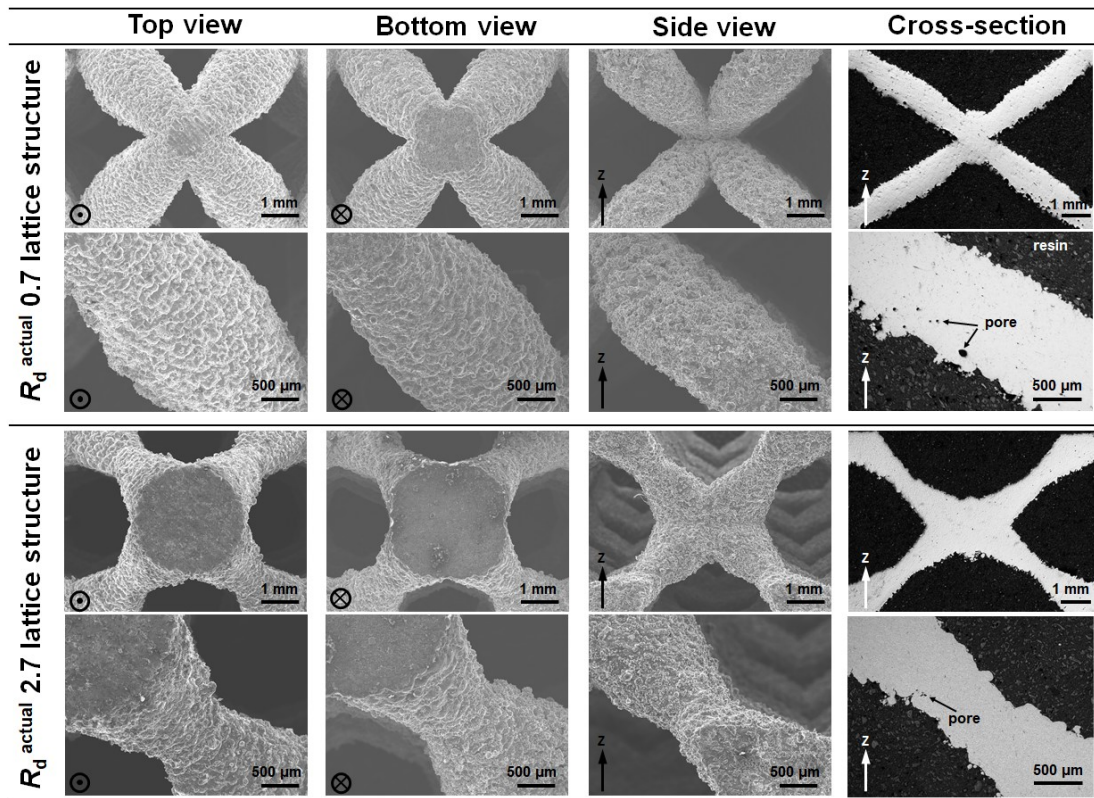


Fig. 3-16 SEM images of the surface of unit cells and struts and optical micrographs of their cross-sections showing building quality of representative lattice structures with R_d^{actual} equal to 0.7 and 2.7.

respectively, indicating satisfied printing quality. In the SEM images, the surfaces of node regions from the bottom view are smoother and larger compared to those from the top view. It is attributed by the wire-electrode cutting used to remove the building panel from the bottom of lattice structures. It has been observed that partially melted raw metal particles attached on the strut surfaces, which may be the reason of the deviation between designed and measured actual R_d values. As illustrated in cross-sectional images of the two lattice structures, the lower surfaces of struts have more pores and rough boundaries than the upper ones, indicating the different printing quality at upper and lower surface. The effects of printing qualities on the compressive behavior of lattice structures are discussed later.

The nominal stress–strain responses of representative lattice structures with R_d^{actual} equal to 0.7, 1.1, 2.0, 2.7, and 3.3 are shown in **Fig. 3-17**. The main mechanical properties including elastic modulus, apparent 0.2% proof stress (related to the compressive strength), and energy absorption capacity are derived from the stress–strain curves and summarized in **Table 3-4**. All the stress–strain responses of the lattice structures exhibit initial linear elastic behavior, subsequent plateau region up to approximately 60% strain, and densification region accompanied by steep rise of nominal stress. The elastic modulus of the lattice structures increases from 0.8 to 1.9 GPa with the increase of R_d^{actual} from 0.7 to 2.0, and then remains almost constant when the R_d^{actual} becomes higher than 2.0. It is noteworthy that the stress–strain curves in the plateau region are relatively flat with less fluctuations in the case of R_d^{actual} equal to 0.7, 1.1, and 2.0. In contrast, the lattice structures with R_d^{actual} equal to 2.7 and 3.3 exhibit

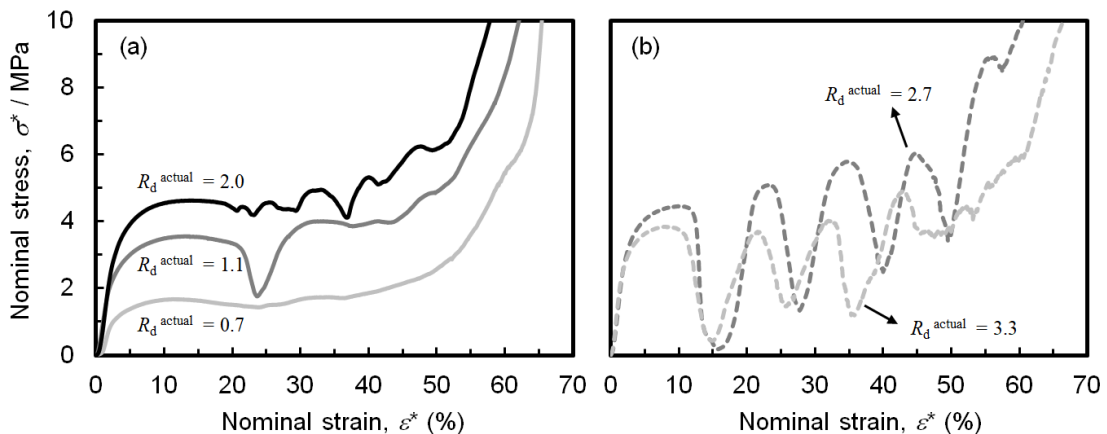


Fig. 3-17 Nominal stress–strain responses of BCC lattice structures with R_d^{actual} equal to (a) 0.7, 1.1, 2.0, (b) 2.7 and 3.3.

oscillating plateau region with many stress drops. Furthermore, the highest value of plateau stress is achieved when R_d^{actual} is equal to 2.0. Thus, the strut shape with R_d^{actual} equal to 2.0 represents the optimized design of BCC unit cell and indicates high energy absorption capacity.

Table 3-4 Mechanical properties of BCC lattice structures with different R_d^{actual} obtained from compression tests.

BCC lattice structures with R_d^{actual}	Elastic modulus /GPa	Apparent 0.2% proof stress /MPa	Energy absorption capacity /MJ·m ⁻³
0.7	0.79	1.21	0.64
1.1	1.33	2.70	1.58
2.0	1.85	3.77	2.40
2.7	1.90	3.73	1.92
3.3	1.87	3.10	1.67

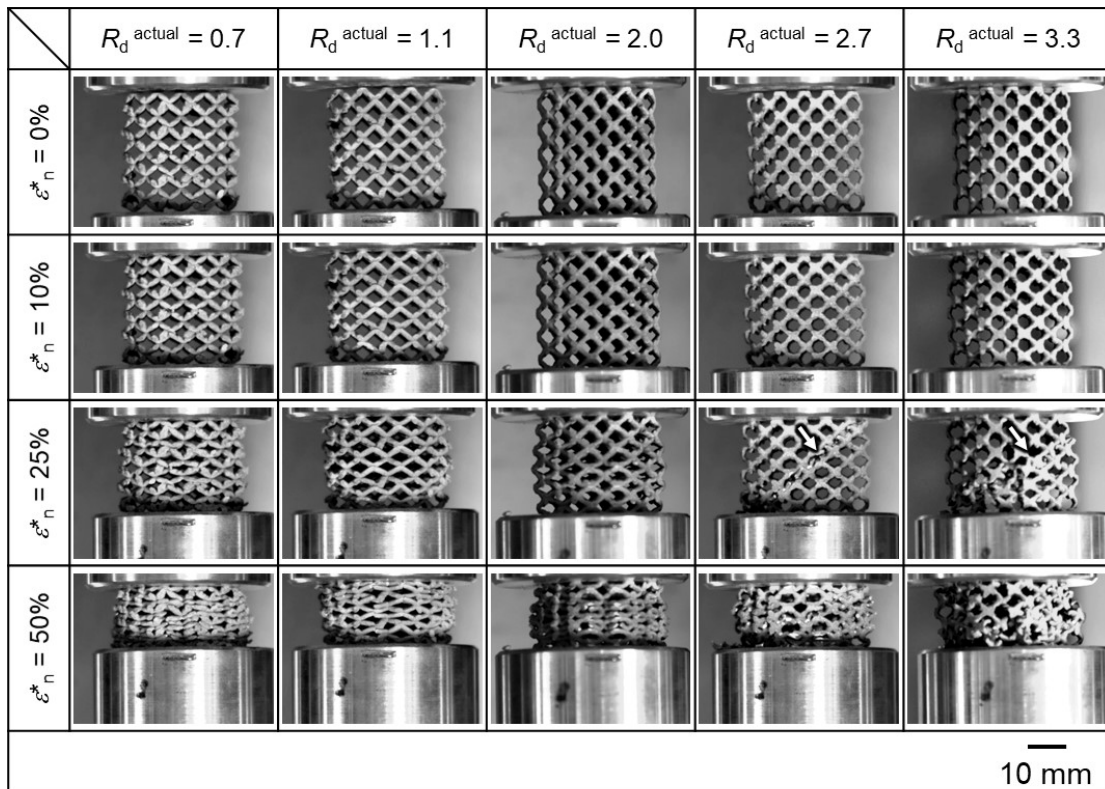


Fig. 3-18 Test appearance of the lattice structures with R_d^{actual} equal to 0.7, 1.1, 2.0, 2.7, and 3.3 at 0%, 10%, 25%, and 50% nominal compressive strains.

Figure 3-18 shows the test appearance of lattice structures with R_d^{actual} equal to 0.7, 1.1, 2.0, 2.7, and 3.3 at 0%, 10%, 25%, and 50% nominal compressive strains. When the nominal strain is 10%, the lattice structures are steadily compressed without the observation of local or global fracture. With further compression at 25%, the lattice structures with R_d^{actual} equal to 0.7, 1.1, and 2.0 display relatively uniform deformation behaviors without shear band formation, corresponding to the stable plateaus in **Fig. 3-17**. And deformation of the struts seems to be node-dominated behavior. For the lattice structures with R_d^{actual} equal to 2.7 and 3.3, clear shear bands are observed as the arrow-marked, and the bended struts exhibit strut-dominated deformation behavior. At the nominal strain of 50%, the severely deformed struts contact with each other and stack to densify at the R_d^{actual} equal to 0.7, 1.1, and 2.0. While the lattice structures with R_d^{actual} equal to 2.7 and 3.3 exhibit the deformation pattern with the combination of shear band formation and local fragmentation.

For a detailed insight into the deformation behavior with and without shear band occurrence, the lattice structures with R_d^{actual} equal to 0.7 and 2.7 are observed by X-ray CT and the cross-sectional images are shown in **Fig. 3-19**. The two lattice structures are deformed in a barrel shape. For the lattice structure with R_d^{actual} equal to 0.7, the unit cells near center

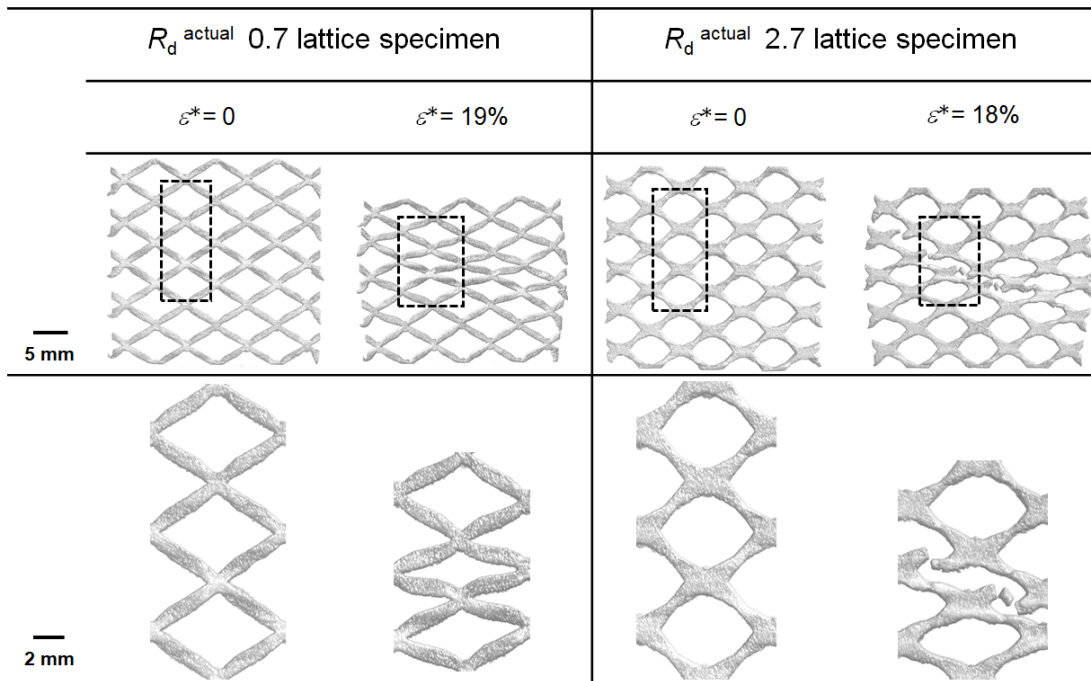


Fig. 3-19 X-ray CT images showing cross-sections of lattice structures with R_d^{actual} equal to 0.7 and 2.7.

preferentially deform and the struts rotate around the nodes, indicating node-dominated behavior. No cracks or fractures is observed within the resolution capacity of the applied X-ray CT apparatus. For the lattice structure with R_d^{actual} equal to 2.7, the fractures of struts are clearly identified as a result of crack initiations and propagations, indicating strut-dominated behavior. As illustrated in **Fig. 3-5 (a)**, the cracks are often initiated at the lower surfaces of struts, which are relatively rough because of the pores and bonded particles (**Fig. 3-16**). The printing quality may lead to the cracks preferentially generated at the lower surface of the lattice structure with R_d^{actual} equal to 2.7. In contrast, cracks are not initiated in the lattice structure with R_d^{actual} equal to 0.7, even at the lower surface of struts where the printing quality is worse than that at R_d^{actual} equal to 2.7. It is suggested that the suppression of crack generations is strongly influenced by the strut shape rather than the printing qualities. The printing qualities may also influence the deformation behavior of lattice structures in the case of higher R_d^{actual} value.

Based on the results above, shear band formation along with the fluctuation of stress–strain response can be effectively suppressed by optimizing the struts shape (small R_d) (**Figs. 3-17 and 18**). This is because that the localized stress at tensile region can be relieved by enlarging the diameter of struts at center, as suggested by FEM (**Fig. 3-14**). According to the compression tests, cracks in the struts do not appear in the lattice structure with R_d^{actual} equal to 0.7 (**Fig. 3-19**). Additionally, shear band dose not form when R_d^{actual} is 2.0, whereas shear band forms when R_d^{actual} is 2.7 (**Figs. 3-17 and 18**). It is demonstrated that high Mises stresses are localized on nodes at low R_d and in struts at high R_d , based on the results of FEM analysis (**Fig. 3-12**). For the lattice model with R_d equal to 0.5, high Mises stresses are mainly concentrated on the nodes (node-dominated deformation) (**Fig. 3-13**). When R_d is equal to 1 and 2, both node and strut region exhibit uniform and high Mises stress. When R_d is equal to 3 and 4, struts mainly suffer Mises stress concentration, leading to the deformation behavior with bended struts (strut-dominated deformation) (**Fig. 3-13**). As a result, the maximum values of Mises stress at tensile stressed regions in the struts increase significantly as R_d increases from 2 to 3. Furthermore, at the lower surface of struts with poor printing quality in the built lattice structure, cracks led by localized tensile stress are prone to initiate. According to these results, in order to avoid the formation of shear band, it is required to the Mises stresses dispersed on struts and nodes to lower the tendency of bending behavior and decrease the tensile stress in struts. It is believed that the modification of strut shape proposed to suppress shear band formation in the

present study can be also effective for strut-based lattice structures with other types of unit cell, such as octet truss, FCC, diamond, rhombic dodecahedron, etc. For the skeletal and sheet-based lattice structures, shear band occurrence may be attributed to the localized stress on defined planes [15, 27, 28]. The shape modification on curved struts or cell walls to rationalize the material distribution may relieve the stress concentration and prevent shear band formation. In addition, the optimization on strut shape is still required after applying the topology optimization design, because the topologically optimized lattice structure with the objective function of stiffness maximization may also experience shear bands. In such instance, the strut shape should be optimized to relax the concentrated tensile stress for the suppression on shear band formation.

The compressive strength and energy absorption capacity of the lattice structures with different R_d are investigated. The compressive strength was estimated as the apparent 0.2% proof stress. The relationships between the apparent 0.2% proof stress obtained by FEM and experiments and R_d values are shown in **Fig. 3-20**. The lattice structure with R_d equal to 2 exhibits the highest the apparent 0.2% proof stress (compressive strength), as indicated in **Figs. 3-11,17** and **Table 3-4**. The calculated apparent 0.2% proof stress agree well with the experimental result, the similar changing trend of increasing with R_d up to 2 and decreasing with R_d above 2 reveals the reliability of the FEA simulation. As demonstrated in **Figs. 3-17** and **18**, the formation of shear band does not appear at R_d less than or equal to 2. In this range of R_d from 0.7 to 2, the experimental apparent 0.2% proof stress increase from approximately 1.2 to 3.8 MPa. It is suggested that the apparent 0.2% proof stress correlating with the level of plateau stress could be controlled in a wide range by altering strut shape alone in the lattice structure without shear band formation. The energy absorption capacities, which are evaluated by the integrating the experimental compressive stress–strain responses before the end of plateau region or densification (appeared when the nominal stress is 1.3 times higher than the plateau stress), are quantified and plotted in **Fig. 3-20**. The energy absorption capacities exhibit similar changing trend with the apparent 0.2% proof stress. By decreasing R_d from 2.7 to 2.0, shear band formation is suppressed in lattice structures and the cumulative energy per unit volume is obviously improved, despite the fact that the experimental apparent 0.2% proof stress is slightly enhanced. This insight demonstrates the importance of suppression on shear band formation while remaining high plateau stress for the utilization of metallic lattice structures as energy

absorber in wide engineering applications.

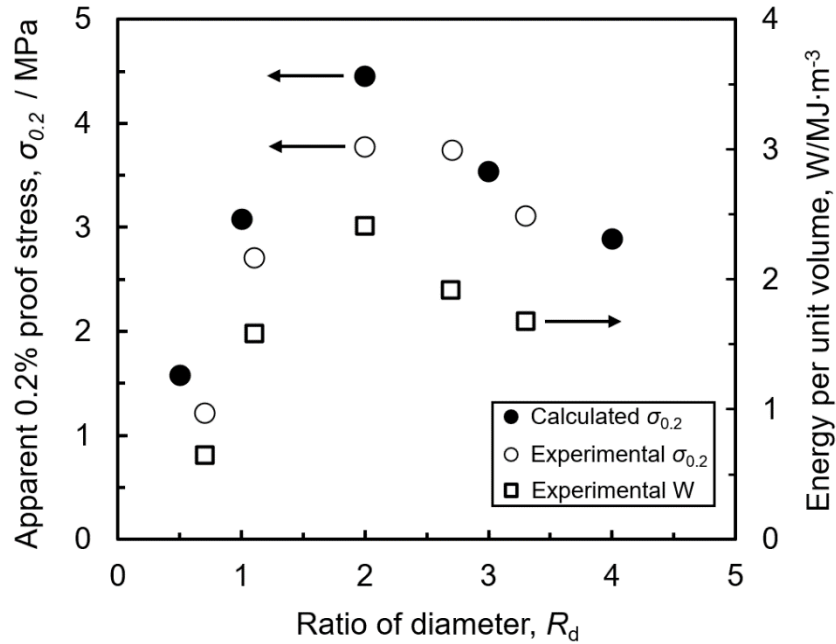


Fig. 3-20 Changes in apparent 0.2% proof stress and experimental energy per unit volume of lattice structures with ratio of diameter of strut (R_d).

3.4 Conclusions

In this chapter, the Al-12Si alloy lattice structures consisting of the body-centered cubic (BCC), BCC-cubic (BC), FCC-cubic (FC), and octet truss (OT) unit cells were fabricated by L-PBF process. The evolution mechanism and preferential formation plane and direction of shear band in lattice structures were clarified. A method altering the strut shape to suppress the shear band formation was proposed and validated. Based on the results, the following conclusions were drawn:

- (1) The formation mechanism and process of shear band in BCC lattice structure were clarified. The shear band is triggered by the crack initiation and propagation at the tensile stressed regions in struts.
- (2) The family of shear bands in crystal-inspired lattice structure corresponds to the slip system of the crystal structure. Shear band was preferentially formed on the densest plane including the most struts when the loading axis is not parallel or perpendicular to this plane.

- (3) FEM results indicated that localized tensile stress in strut can be relieved by lower R_d (large diameter at the strut center and small diameter near node), leading to a transition of deformation mode from strut-dominated to node-dominated. This behavior predicted a low tendency of shear band formation.
- (4) The experimental results showed that the shear band was suppressed in the lattice structures with R_d^{actual} equal to 0.7, 1.1, and 2.0. Relaxation of concentrated stress in struts and high Mises distributed on node contributed to the suppression of shear band.
- (5) The compressive strength and energy absorption capacity of the BCC lattice structures were substantially enhanced by optimized strut shape. The apparent 0.2% proof stress can be controlled in a wide range of approximately 1.2~3.8 MPa without the shear band formation in the plateau region.

References

- [1] V Crupi, E Kara, G Epasto, E Guglielmino, H Aykul, Static behavior of lattice structures produced via direct metal laser sintering technology, *Mater. Des.* 135 (2017) 246–256.
- [2] C. Qiu, S. Yue, N.J.E. Adkins, M. Ward, H. Hassanin, P.D. Lee, P.J. Withers, M.M. Attallah, Influence of processing conditions on strut structure and compressive properties of cellular lattice structures fabricated by selective laser melting, *Mater. Sci. Eng. A* 628 (2015) 188–197.
- [3] M. Kuczewicz, P. Baranowski, M. Stankiewicz, M. Konarzewski, Modelling and testing of 3D printed cellular structures under quasi-static and dynamic conditions, *Thin-Walled Struct.* (2019) 145.
- [4] I. Maskery, N.T. Aboulkhair, A.O. Aremu, C.J. Tuck, I.A. Ashcroft, R.D. Wildman, R.J.M. Hague, A mechanical property evaluation of graded density Al-Si10-Mg lattice structures manufactured by selective laser melting, *Mater. Sci. Eng. A* 670 (2016) 264–274.
- [5] B. Van Hooreweder, Y. Apers, K. Lietaert, J.P. Kruth, Improving the fatigue performance of porous metallic biomaterials produced by Selective Laser Melting, *Acta Biomater.* 47 (2017) 193–202.
- [6] A. Suzuki, K. Sekizawa, M. Liu, N. Takata, M. Kobashi, Effects of heat treatments on compressive deformation behaviors of lattice-structured AlSi10Mg alloy fabricated by selective laser melting, *Adv. Eng. Mater.* 21 (10) (2019) 1900571.

- [7] S. Roos, C. Botero, J. Danvind, A. Koptioug, L. E. Rännar, Macro-and Micromechanical Behavior of 316LN Lattice Structures Manufactured by Electron Beam Melting, *J. Mater. Eng. Perform.* 28 (12) (2019) 7290–7301.
- [8] R. Gümrük, R.A.W. Mines, Compressive behaviour of stainless steel micro-lattice structures, *Int. J. Mech. Sci.* 68 (2013) 125–139.
- [9] P. Li, Z. Wang, N. Petrinic, C.R. Siviour, Deformation behaviour of stainless steel microlattice structures by selective laser melting, *Mater. Sci. Eng. A* 614 (2014) 116–121.
- [10] S.Y. Choy, C.-N. Sun, K.F. Leong, J. Wei, Compressive properties of Ti-6Al-4V lattice structures fabricated by selective laser melting: design, orientation and density, *Addit. Manuf.* 16 (2017) 213–224.
- [11] L. Xiao, W. Song, M. Hu, P. Li, Compressive properties and micro-structural characteristics of Ti-6Al-4V fabricated by electron beam melting and selective laser melting, *Mater. Sci. Eng. A* 764 (2019) 138204.
- [12] A. Cutolo, B. Engelen, W. Desmet, B. Van Hooreweder, Mechanical properties of diamond lattice Ti-6Al-4V structures produced by laser powder bed fusion: On the effect of the load direction, *J. Mech. Behav. Biomed. Mater.* 104 (2020) 103656.
- [13] Y. Yang, M. Shan, L. Zhao, D. Qi, J. Zhang, Multiple strut-deformation patterns based analytical elastic modulus of sandwich BCC lattices, *Mater. Des.* 181 (2019) 107916.
- [14] C.L. Li, H.S. Lei, Y.B. Liu, X.Y. Zhang, J. Xiong, H. Zhou, D.N. Fang, Crushing behavior of multi-layer metal lattice panel fabricated by selective laser melting, *Int. J. Mech. Sci.* 145 (2018) 389–399.
- [15] L. Yang, C. Yan, W. Cao, Z. Liu, B. Song, S. Wen, C. Zhang, Y. Shi, S. Yang, Compression–compression fatigue behaviour of gyroid-type triply periodic minimal surface porous structures fabricated by selective laser melting, *Acta Mater.* 181 (2019) 49–66.
- [16] L. Liu, P. Kamm, F. García-Moreno, J. Banhart, D. Pasini, Elastic and failure response of imperfect three-dimensional metallic lattices: the role of geometric defects induced by Selective Laser Melting, *J. Mech. Phys. Solids.* 107 (2017) 160–184.
- [17] X. Cao, D. Xiao, Y. Li, W. Wen, T. Zhao, Z. Chen, Y. Jiang, D. Fang, Dynamic compressive behavior of a modified additively manufactured rhombic dodecahedron 316l stainless steel lattice structure, *Thin-Walled Struct* 148 (2020) 106586.

- [18] D.S. Al-Saedi, S. Masood, M. Faizan-Ur-Rab, A. Alomarah, P. Ponnusamy, Mechanical properties and energy absorption capability of functionally graded F2BCC lattice fabricated by SLM, *Mater. Des.* 144 (2018) 32–44.
- [19] M.S. Pham, C. Liu, I. Todd, J. Lertthanasarn, Damage-tolerant architected materials inspired by crystal microstructure, *Nature* 565 (2019) 305–311.
- [20] M. Liu, T. Wada, A. Suzuki, N. Takata, M. Kobashi, M. Kato, Effect of annealing on anisotropic tensile properties of Al–12% Si alloy fabricated by laser powder bed fusion, *Crystals* 10 (11) (2020) 1007.
- [21] T.B. Sercombe, X. Xu, V.J. Challis, R. Green, Y. Sheng, Z. Zhang, P.D. Lee, Failure modes in high strength and stiffness to weight scaffolds produced by Selective Laser Melting, *Mater. Des.* 67 (2015) 501–508.
- [22] Y. Li, K. Lietaert, W. Li, X.Y. Zhang, M.A. Leeftang, J. Zhou, A.A. Zadpoor, Corrosion fatigue behavior of additively manufactured biodegradable porous iron, *Corros. Sci.* 156 (2019) 106–116.
- [23] O. Al-Ketan, R. Rowshan, R.K.A. Al-Rub, Topology-mechanical property relationship of 3D printed strut, skeletal, and sheet based periodic metallic cellular materials, *Addit. Manuf.* 19 (2018) 167–183.
- [24] C. Bonatti, D. Mohr, Large deformation response of additively-manufactured FCC metamaterials: from octet truss lattices towards continuous shell mesostructures, *Int. J. Plast.* 92 (2017) 122–147.
- [25] T. Tancogne-Dejean, D. Mohr, Stiffness and specific energy absorption of additively-manufactured metallic BCC metamaterials composed of tapered beams, *Int. J. Mech. Sci.* 141 (2018) 101–116.
- [26] X. Cao, S. Duan, J. Liang, W. Wen, D. Fang, Mechanical properties of an improved 3D-printed rhombic dodecahedron stainless steel lattice structure of variable cross section, *Int. J. Mech. Sci.* 145 (2018) 53–63.
- [27] L. Zhang, S. Feih, S. Daynes, S. Chang, M.Y. Wang, J. Wei, W.F. Lu, Energy absorption characteristics of metallic triply periodic minimal surface sheet structures under compressive loading, *Addit. Manuf.* 23 (2018) 505–515.
- [28] H. Zhou, M. Zhao, Z. Ma, D.Z. Zhang, G. Fu, Sheet and network based functionally graded lattice structures manufactured by selective laser melting: Design, mechanical properties,

and simulation, Int. J. Mech. Sci. 175 (2020) 105480.

4. Lattice structures inspired by crystal structures

4.1 Introduction

The crystal structures represent an ordered array of atoms describing their arrangement. The lattice structures with periodic pattern have been observed to be analogous to the crystal structures. In the unit cells of lattice structure, the node is analogous to the atom and the strut is equivalent to the atomic bond in crystal structure. Therefore, the designs for lattice structures through mimicking the atomic crystallographic configurations have been proposed. For example, the mechanical behaviors of the lattice structures with the body-centered cubic (BCC) and face-centered cubic (FCC) unit cells, which are analogous to the BCC and FCC crystal structures, have been studied in literatures [1]. Liu et al. suggested that a substantial improvement in the strength and energy absorption capacity of BCC lattice structure was achieved by reinforced node, which mimicked the atoms of crystal structures [2]. In Chapter 3, it demonstrated that the formation plane and direction of shear bands in BCC and FCC (octet truss) lattice structures correspond to the slip systems of the corresponding crystal structures. This insight offers a possible method to suppress shear band formation in lattice structures through mimicking complex crystal structures whose slip systems are difficult to act. Based on the similarities between crystal structure and lattice structure, Pham et al. integrated the hardening mechanisms found in crystalline materials into the architected lattice structures [3]. The metallurgical concepts enable the design of lattice structures with desired properties, such as architected meta-materials mimicking geometrically close-packed (GCP) Ni_3Al phase. Laves phase is a common class of AB_2 -type intermetallic compounds with topologically close-packed (TCP) structure (known as Frank-Kasper structure) [4]. The more common structures are the cubic C15 and hexagonal C14 with a minor form of the hexagonal C36 type [5]. In the C15 Laves structure, sublattice site of A-atom forms the diamond crystal structure and sublattice site of B-atom forms the connected tetrahedrons [5, 6]. The diamond-inspired lattice structure with negative Maxwell stability criterion (M) exhibits bending-dominated deformation [7]. Tetrahedron architecture locally formed using struts to connect the B atoms has the M value of zero and may exhibit stretch-dominated deformation. Therefore, architected lattice structure inspired by C15 Laves structure can indicate unique mechanical behaviors, owing to the special arrangement of C15 crystal structure with the combination of diamond structure and

tetrahedron.

In this chapter, the lattice structures were designed by mimicked C15-type TCP structure as well as diamond crystal structure for comparison. L-PBF process was applied for the fabrication of Al-12Si lattice structure. The compressive properties of the lattice structures were investigated by full and interrupted compression tests, X-ray CT observations and FEM analysis. The deformation behaviors of the C15 lattice structures were characterized from the view of the Gibson-Ashby equation [8].

4.2 Materials and methods

For the lattice structures inspired by common BCC or FCC crystal structure, it has been reported that these lattice structures compose of distinct types of unit cells with same node arrangement but various struts [2, 3, 9, 10], as indicated in **Fig. 1-8** in Chapter 1. In order to ensure the design consistency of the lattice structure based on the inspiration from crystal structures, a design strategy for unit cell is proposed: the position of atoms in crystal structure is considered as node, and struts are used to connect the first-nearest-neighbor nodes to form a unit cell. Accordingly, the bending-dominated BCC and stretch-dominated octet truss lattice structures are obtained on the basis of BCC and FCC crystal structures [11, 12], as shown in **Fig. 4-1**. In this chapter, the architected diamond and C15 unit cells were designed by mimicking the

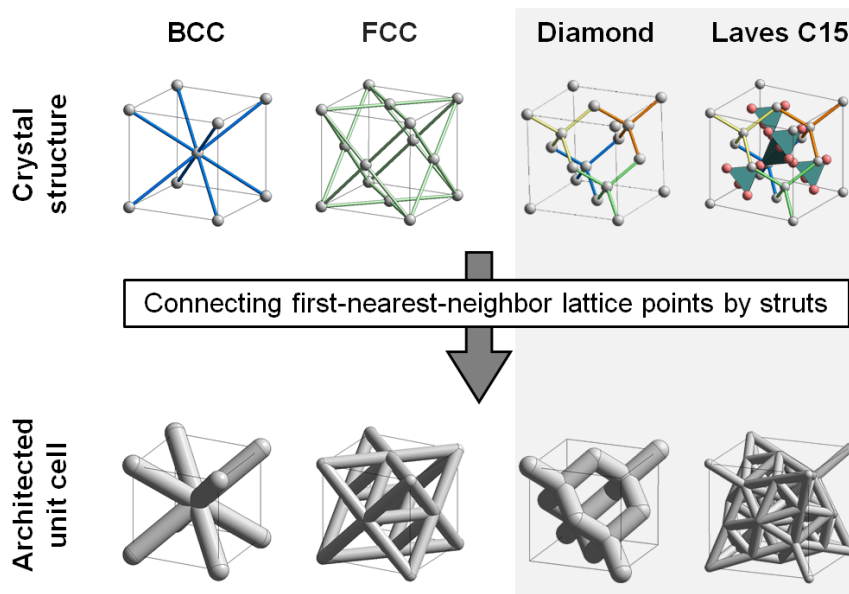


Fig. 4-1 Architected unit cells designed via mimicking crystal structures.

Table 4-1 The designed and measured relative densities of fabricated lattice specimens.

Lattice structure	Designed ρ^*/ρ_s	Measured ρ^*/ρ_s	Error /%
Diamond	0.174	0.167	-4.0
	0.179	0.173	-3.4
	0.201	0.204	1.5
C15	0.224	0.216	-3.6
	0.247	0.236	-4.5
	0.271	0.259	-4.4
	0.383	0.374	-2.3

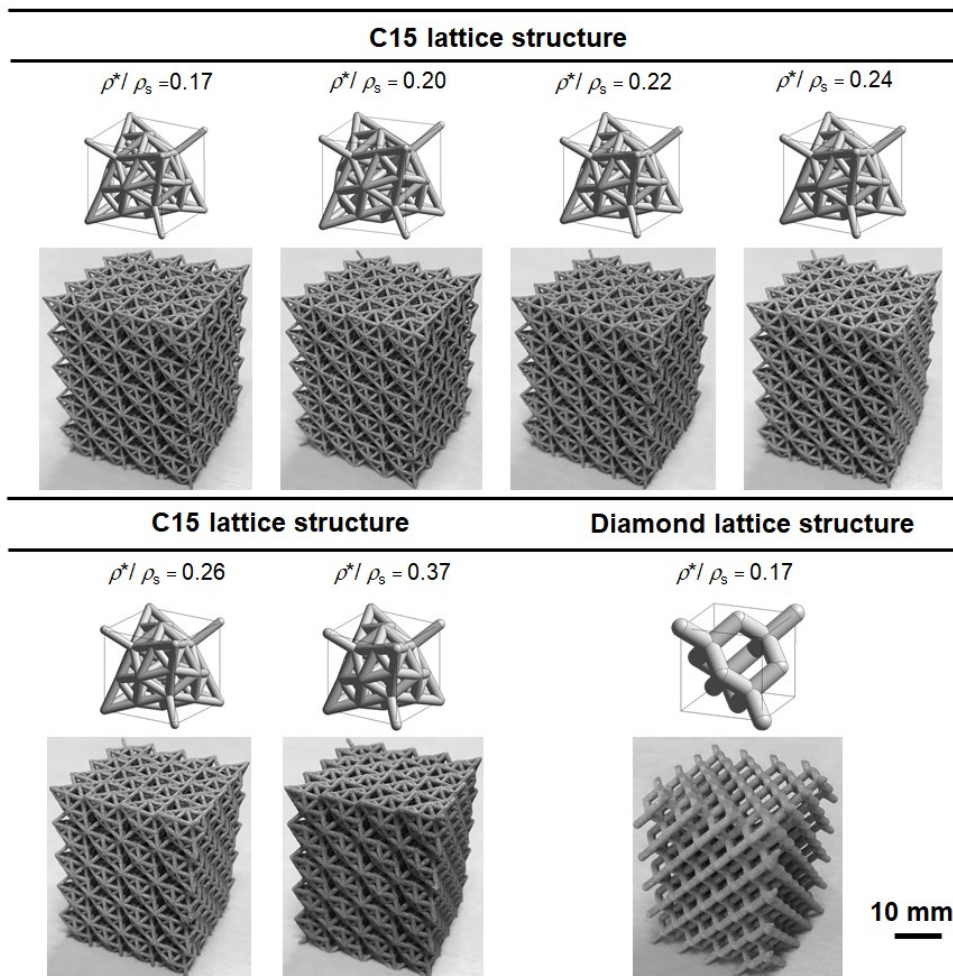


Fig. 4-2 L-PBF fabricated diamond lattice structure and C15 lattice structures with various relative densities.

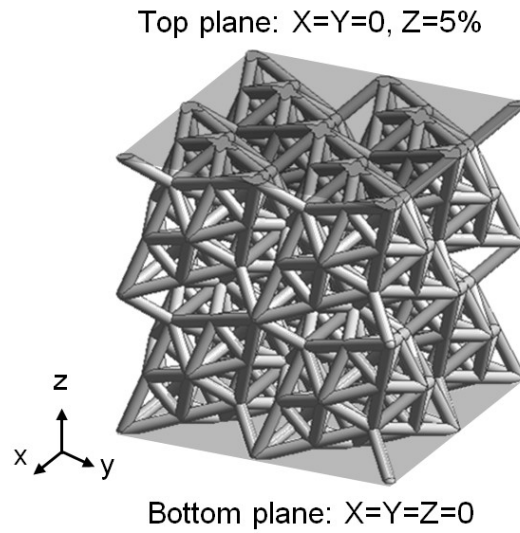


Fig. 4-3 Reduced FEM C15 lattice model consisting of 8 unit cells.

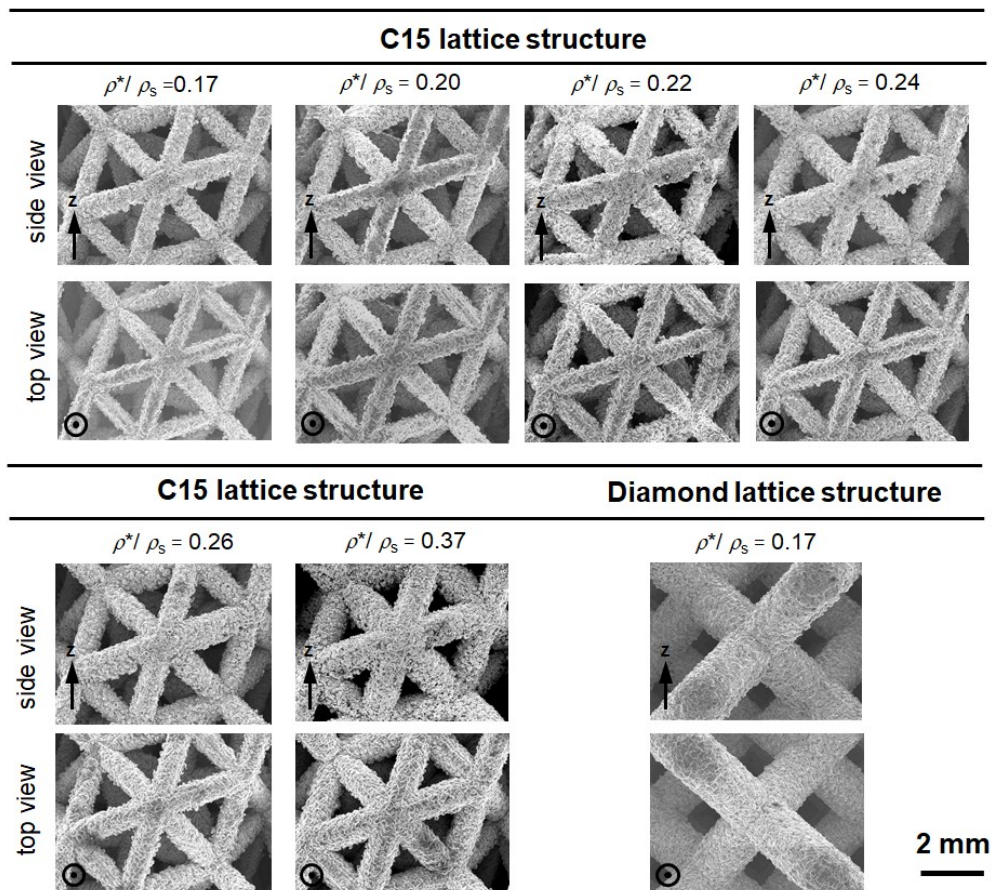


Fig. 4-4 SEM images showing building quality of C15 and diamond lattice structures.

corresponding crystal structures (**Fig. 4-1**). The L-PBF process using Al–12Si alloy raw powder was applied to fabricate lattice structures. The detailed processing conditions and post-treatment are the same as used in Chapter 3. The measured relative densities for the diamond (0.167) and C15 (0.173~0.374) lattice structures are listed and compared with designed values in **Table 4-1**. The errors of relative density between the design and fabrication are less than 5%. The photos of fabricated lattice structures are present in **Fig. 4-2**. Scanning electron microscopy (SEM) was used to observe the building quality of the lattice structures. Compression tests and X-ray CT scan were carried out. FEM analysis was conducted by establishing a reduced C15 lattice model consisting of 8 unit cells, as shown in **Fig. 4-3**. The input material property, mesh, boundary and loading conditions have been also demonstrated in Chapter 3.

4.3 Results and discussion

Figure 4-4 presents the SEM images of the struts in C15 and diamond lattice structures. In side view, it was found that partially melted raw metal particles attached on the lower surfaces of struts. This phenomenon results in a relatively rougher surfaces and larger diameters of struts in side view compared to those in the top view. In addition, the diamond lattice structure seems to exhibit better surface condition than C15 lattice structures, owing to the larger designed struts diameter of diamond lattice structure. Generally, the struts in all lattice structures were well-printed, because no clear defects such as cracks or lack of materials was observed in the SEM images.

Figure 4-5 shows the comparison of nominal stress–strain curves between C15 ($\rho^*/\rho_s = 0.20$) and diamond ($\rho^*/\rho_s = 0.17$) lattice structures under compression, along with the test appearances at different nominal strain. The diamond lattice structure exhibited a typical compressive stress–strain response of cellular structure. It was observed that the initial linear elastic behavior was followed by plateau region, where stress fluctuations occurred due to the localization deformation of struts (test appearance in **Fig. 4-5**). The structure finally entered densification region with sharply increasing stress. As for the C15 lattice structure, the structure did not densify at the end of plateau at the nominal strain of approximately 20%, but a 2nd plateau region emerged from the nominal strain of approximately 30%. Therefore, the C15 lattice structure exhibits unique two plateau regions at different stress levels. In the test appearance of C15 lattice structure shown in **Fig. 4-5**, it seems that the lattice structure

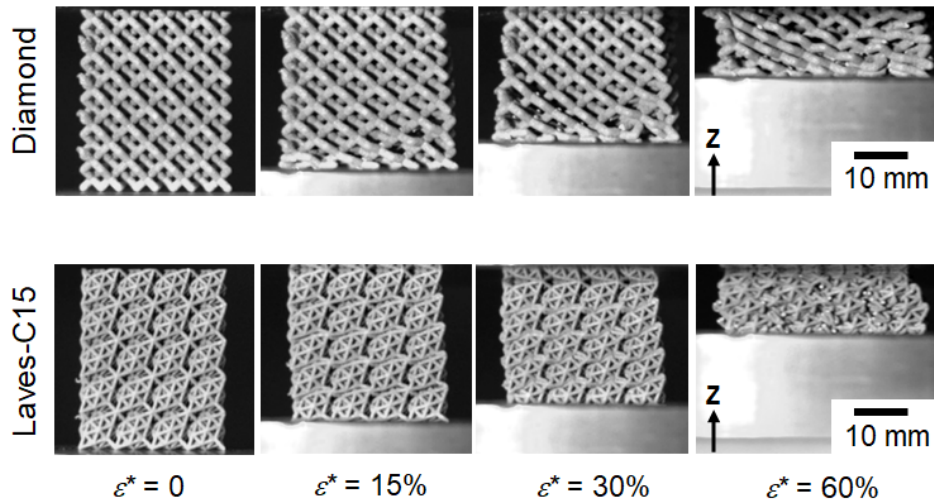
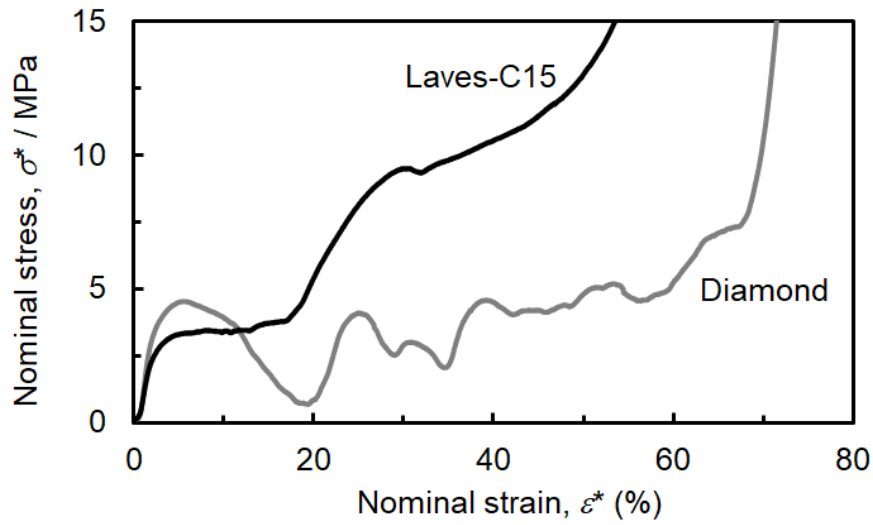


Fig. 4-5 Compressive nominal stress–strain curves of C15 and diamond lattice structures along with the test appearances at the compressive strains of 0%, 15%, 30%, and 60%.

underwent non-uniform deformation behavior, some struts at local regions deformed preferentially and other struts deformed subsequently. This behavior may result in the two plateau regions. Detailed step-by-step deformation behavior is characterized by X-ray CT observation to investigate the cause of the two plateau regions, which will be addressed in further discussion.

Figure 4-6 presents the stress–strain responses of C15 lattice structures with various relative densities. For the lattice structures with the relative density in the range of 0.17~0.26, two plateau regions appeared. However, the C15 lattice structure exhibited one plateau region similar to the typical cellular structures when the relative density was 0.37. The mechanical

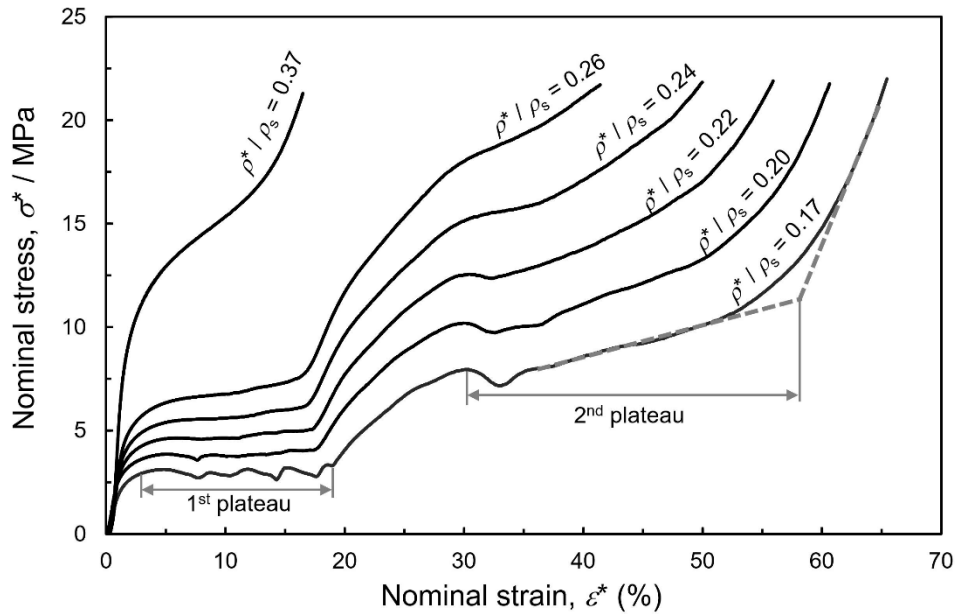


Fig. 4-6 Stress–strain curves of C15 lattice structures with the relative density of 0.17~0.37.

Table 4-2 Mechanical properties of C15 lattice structures with the relative density of 0.17~0.37.

Relative density of C15 lattices	Elastic modulus, E^*/GPa	Yield stress, σ_y^*/MPa	1st plateau		2nd plateau		Energy absorption capacity, $W/\text{MJ}\cdot\text{m}^{-3}$
			plateau stress, σ_{pl}^*/MPa	strain range (%)	plateau stress, σ_{pl}^*/MPa	strain range (%)	
0.17	0.25	2.2	3.0	17.7	9.4	26.7	3.8
0.20	0.31	2.8	3.9	16.6	11.7	23.4	4.4
0.22	0.38	3.3	4.8	16.2	14.2	21.2	5.0
0.24	0.47	3.6	5.7	15.5	16.3	11.3	4.4
0.26	0.59	3.9	6.9	15.4	19.0	4.7	4.0
0.37	1.03	6.8	14.8	12.2	-	-	1.8

properties obtained from the compressive tests are given in **Table 4-2**. Apparent elastic modulus (E^*) and yield stress (σ_y^*) was quantified prior to the 1st plateau region. The apparent 0.2% proof stress was served as yield stress here. The plateau start/end strains were determined by the intersections of tangent lines between the adjacent segments with different slope (**Fig. 4-6**). The plateau strain range was defined as the difference of plateau start and end strain. The plateau stress was determined by the average stress in the plateau strain range, because of the fact that the stress–strain curves in the plateau region were relatively smooth. As relative density increases, the level of plateau stress increases while the strain range of plateau region decreases. It is suggested that the stress and strain range of the two plateau regions can be adjusted by

changing the relative density.

The C15 lattice structures can absorb energy in two graded plateau regions. The energy absorption capacities provided by 1st plateau and 2nd plateau are quantified by integrating the stress–strain curves from zero to the 1st plateau end strain and from the 1st plateau end strain to the 2nd plateau end strain, respectively. The total energy absorption capacity is equal to the summations of the energy of 1st plateau and 2nd plateau. The relationships between the energy per unit volume and relative density of the C15 lattice structures are illustrated in **Fig. 4-7**. For the 1st plateau region, the energy absorption capacity increases almost linearly with increasing relative density, but the level of absorbed energy is relatively low. The energy per unit volume of 2nd plateau is much higher than that of 1st plateau, and shows the similar tendency with the total energy of C15 lattice structures. The peak value ($5.0 \text{ MJ}\cdot\text{m}^{-3}$) of the total energy per unit volume is achieved at the relative density of 0.22. This reaches the high level of energy-absorbing capability among the reported aluminum alloy lattice structures, as compared to **Fig. 2-17** in Chapter 2. Therefore, the two plateaus appeared in C15 lattice structures can provide high capacity of energy absorption through two graded stages. When the relative

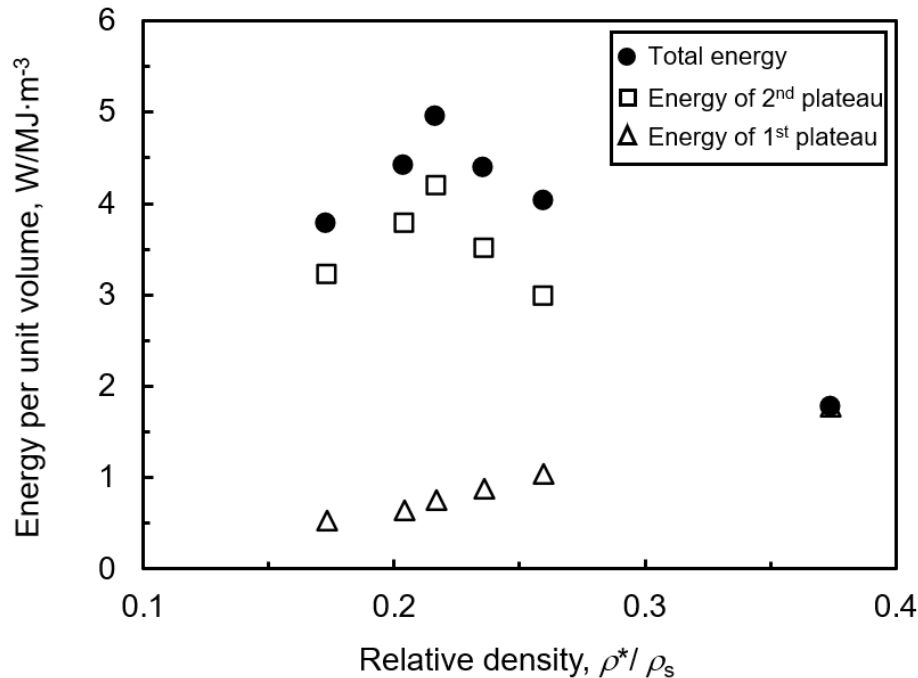


Fig. 4-7 Relationships between the energy absorption capacities of the 1st plateau region, 2nd plateau region, and 1st plateau region + 2nd plateau region of the C15 lattice structures and relative densities.

density is higher than 0.22, although the stresses in the two plateau regions were enhanced, the plateau strain ranges were shortened, especially for the 2nd plateau region. In this case, short plateau region affects the energy absorption capacity more significantly than the enhanced plateau stress, resulting in substantial degeneration at high relative density. For the lattice structure with the relative density of 0.37, the energy per unit volume is the lowest due to the fact that only one plateau can absorb energy. This result indicates the significance of 2nd plateau region for the energy absorption capacity of C15 lattice structures.

Figure 4-8 (a) shows the von Mises stress distributions at 3% nominal strain of C15 lattice model with the relative density of 0.20 simulated by FEM analysis. At this nominal strain, the nominal stress obtained by FEM was approximately 4.2 MPa, while the experimental value was 3.6 MPa. The mechanical property of C15 lattice structure was slightly overpredicted, owing to the established ideal model without geometry imperfection. Despite this, the calculated results agree well with experimental results and show the validity of simulations. In the unit cells of lattice model, the Mises stress is mainly localized on the corner struts, whereas the center struts exhibited low Mises stress (lower than approximately 80MPa). It is caused by the unequal distribution of struts at corner (small number of struts) and center (large number of struts) region in unit cell. According to the distinct struts and associated stress distribution of corner and center region in unit cell, the C15 lattice structure can be recognized as the repetition of two separated units with graded local relative density: crisscross and interconnected deltahedron, as illustrated in **Fig. 4-8 (b)**. The local densities for the two units were determined by the value of

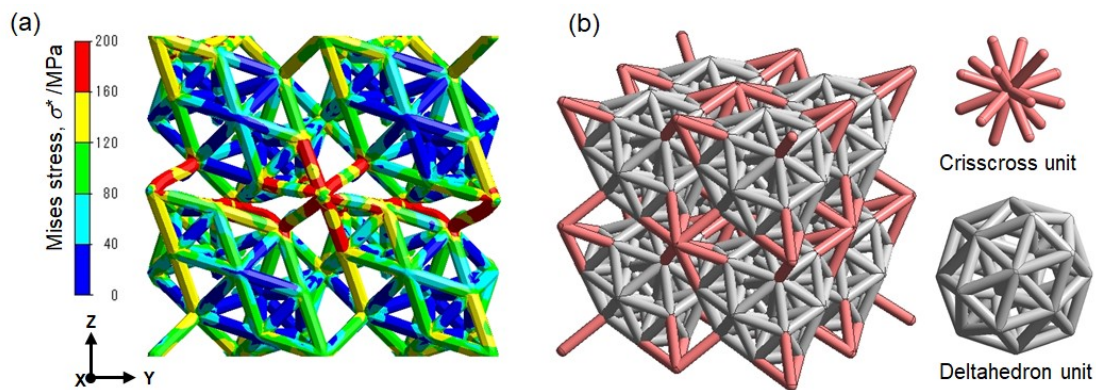


Fig. 4-8 von Mises stress distribution of C15 lattice model at 3% nominal strain. (b) Schematic illustration showing C15 lattice structure distinguished by crisscross and deltahedron units.

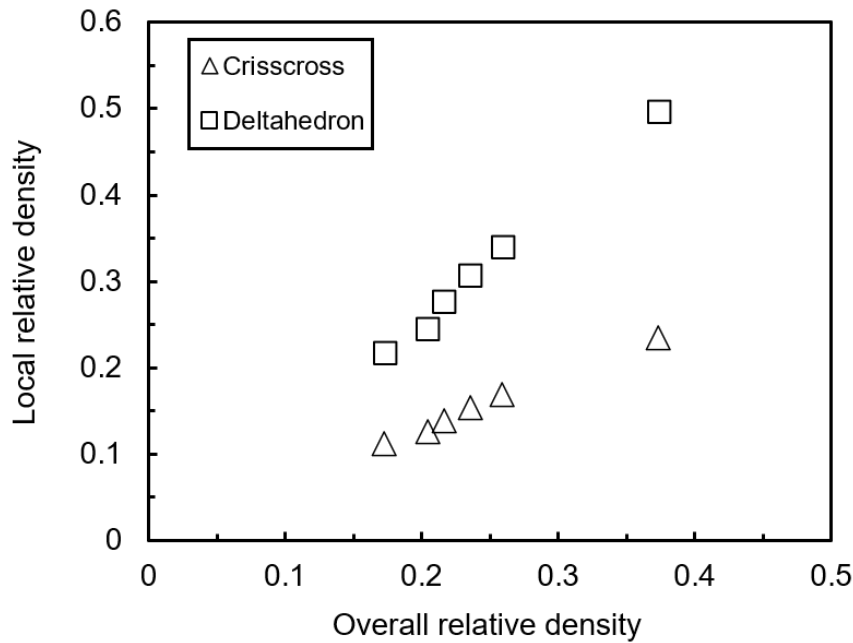


Fig. 4-9 The relationships between the local relative density of crisscross and deltahedron units and the overall relative density of C15 lattice structures.

material volume divided by the occupied space. The relationships between the local relative density of crisscross and deltahedron units and the overall relative density of C15 lattice structures are shown in **Fig. 4-9**.

Figure 4-10 (a) presents the (100) cross-sectional images observed by X-ray CT scan at different compressive strains of C15 lattice structures with the relative density of 0.20. Four unit cells in lattice structure are enlarged to show the detailed deformation of struts. The stress–strain curves of interruptedly compressed C15 lattice structure are illustrated in **Fig. 4-10 (b)**. At the nominal strain of 9.0% in the 1st plateau region, one layer of crisscross units severely deformed by bending the struts owing to the high Mises stress distribution (**Figs. 4-10 (a)** and **4-8 (a)**). Meanwhile, the deformation of the struts in the deltahedron unit was not distinct compared to the struts in crisscross units. With further compression to the end of 1st plateau region at the nominal strain of 19.1%, the rest layers of crisscross units perpendicular to the loading direction successively collapsed in the same pattern as the initially deformed layer. However, the plastic deformations of deltahedron units were still hardly noticeable, as a result of low stress distribution (**Fig. 4-8 (a)**). The 1st plateau region exhibited smooth flow stress of approximately 3.9 MPa without fluctuation, because the struts in crisscross units deformed in a moderate bending behavior rather than drastic deformations of brittle or shear failure, which normally

lead to abrupt stress drops. After the densification of the crisscross unit layers, the upper struts in deltahedron units contacted the low ones to bear higher loads, thus the stress increased again. The 2nd plateau region emerged at the nominal strain of 32.8% and nominal stress of 10.8 MPa in the C15 lattice structure. Large plastic deformations and generated cracks were observed in the struts of deltahedron units. Finally, almost all the struts deformed by intersecting and stacking with each other, which resulted in the structure densification. The deltahedron unit in C15 lattice structure is analogous to the polyhedron in complex close-packed intermetallic [13]. The preferential deformation of low-density crisscross unit is similar to the deformation on the less dense space of atoms between the polyhedrons, despite the fact that the preferential

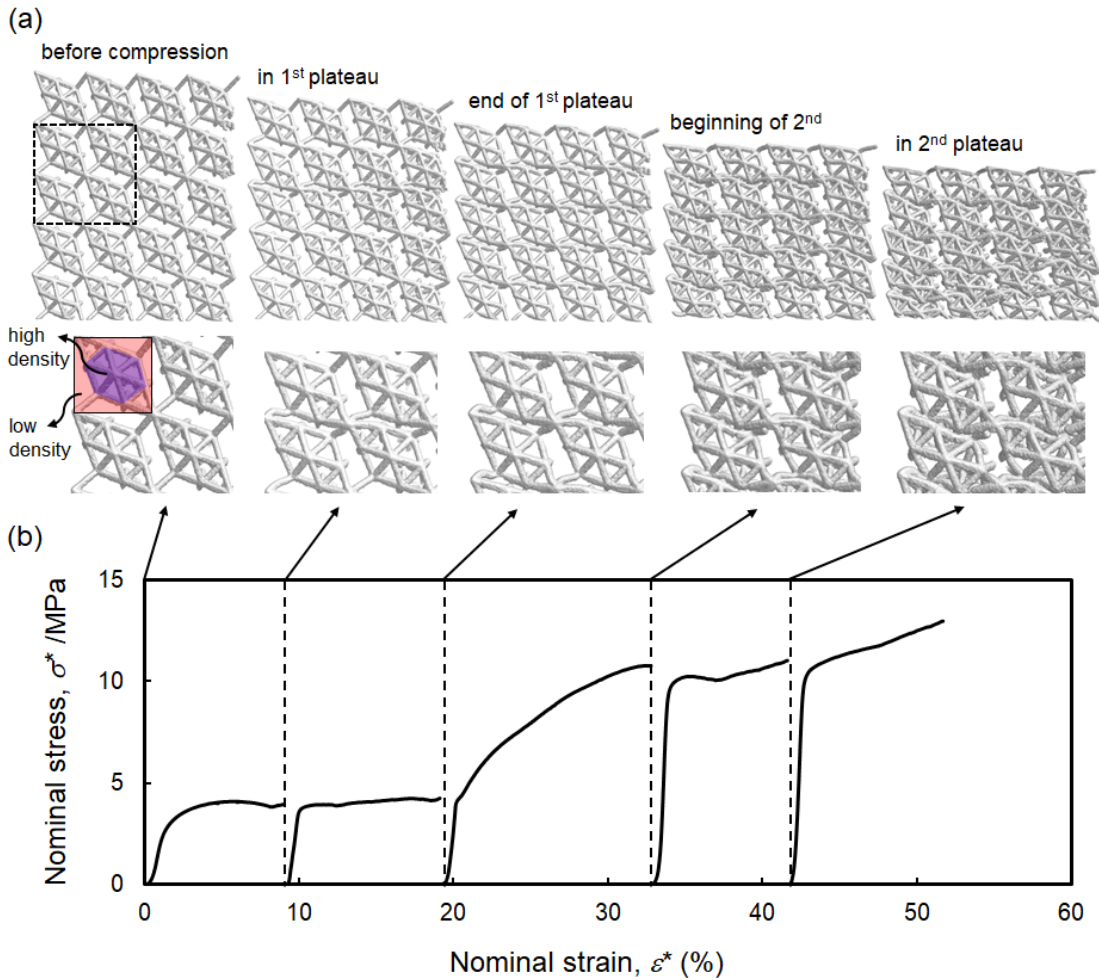


Fig. 4-10 (a) X-ray CT images of C15 lattice structure with the relative density of 0.20 before compression and compressed at different nominal strains. (b) Stress–strain curves obtained by interrupted compression test.

deformation in C15 lattice structure was not shearing analogous to the slip deformation in crystal structures. Therefore, the results reveal the possibility that the lattice structure with various polyhedron units inspired by other TCP intermetallics may yield multi-plateau regions with graded stress levels.

According to the Gibson-Ashby equation (Eq. (1.4) and (1.5) in Chapter 1), relative densities ρ^*/ρ_s exhibit power law relationships with the relative elastic modulus E^*/E_s and relative yield strength σ_y^*/σ_s of cellular structures. As indicated in Table 1-1 in Chapter 1, the value of the exponent n determines the bending- or stretch-dominated deformation behavior. The $n \geq 2$ for relative elastic modulus and $n \geq 1.5$ for the relative yield strength indicate bending-dominated behavior, while $n \leq 1$ for both of them indicate stretch-dominated behavior. Figure 4-11 shows the relative elastic modulus and relative yield strength as functions of overall relative density of the C15 lattice structures and local relative density of crisscross units. The exponents n of E^*/E_s and σ_y^*/σ_s against the overall relative density are 1.9 and 1.5, respectively, which is an indicator of the bending-dominated mode for C15 lattice structure. However, the deformation behavior predicted by the Maxwell stability criterion revealed over-stiff stretch-dominated mode, due to the fact that the Maxwell number (M) of unit cell in C15 lattice structure is 19 with 115 struts and 34 nodes (Eq. (1.1) in Chapter 1). The

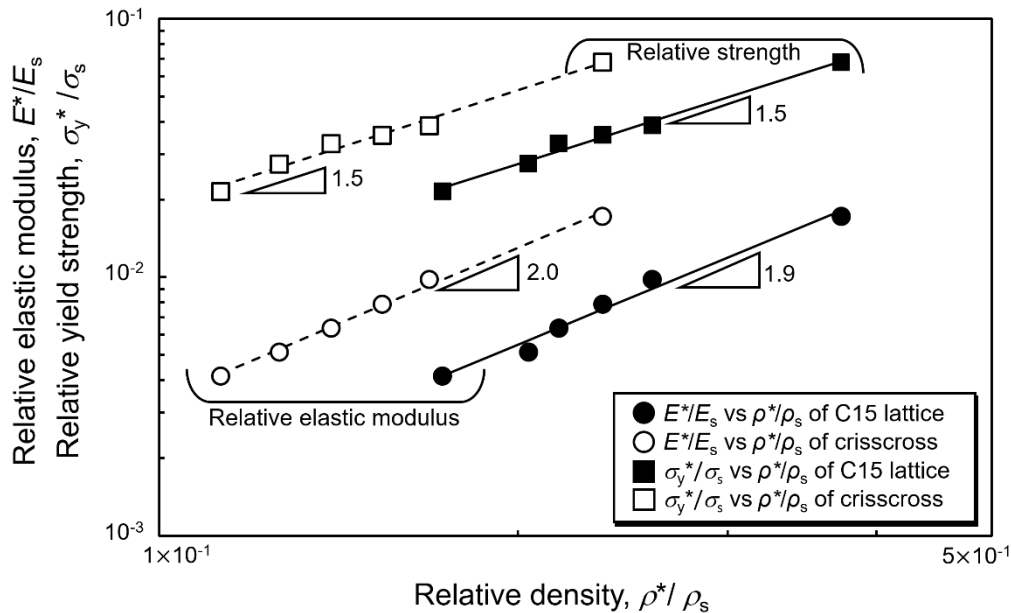


Fig. 4-11 Changes in the relative elastic modulus and relative yield strength as functions of overall relative density of C15 lattice structures and local relative density of crisscross units.

contradictory results between experiments and predictions are due to the successive deformation behaviors of the crisscross and deltahedron units with graded local relative densities in C15 lattice structures. The relative elastic modulus and yield strength were determined by the elastic and early plastic regions, at which the deformation behaviors of C15 lattice structures were dominated by the bended struts in crisscross units with low local relative density (**Fig. 4-10 (a)**). In addition, the negative Maxwell number ($M = -29$) of the crisscross unit with 16 struts and 17 nodes agrees with the discussion above. E^*/E_s and σ_y^*/σ_s scaling $(\rho^*/\rho_s)^{1.9}$ and $(\rho^*/\rho_s)^{1.5}$ for the crisscross unit also revealed the bending-dominated mode of early deformed C15 lattice structure, which was mainly attributed by the crisscross units.

The power law relationships between the plateau stress σ_{pl}^* and relative densities, including the overall relative density of the C15 lattice structures and local relative density of crisscross and deltahedron units, are plotted and shown in **Fig. 4-12**. The 1st plateau stress changed with $(\rho^*/\rho_s)^{2.1}$ and $(\rho^*/\rho_s)^{2.2}$ for C15 lattice structures and crisscross units, respectively. For the bending-dominated lattice structures in Chapter 2 and reported literature [14], the exponent n is in the range of 2.1~2.4. These results consistently support that the crisscross units deformed in a bending-dominated mode during the 1st plateau. The exponents of the 2nd plateau

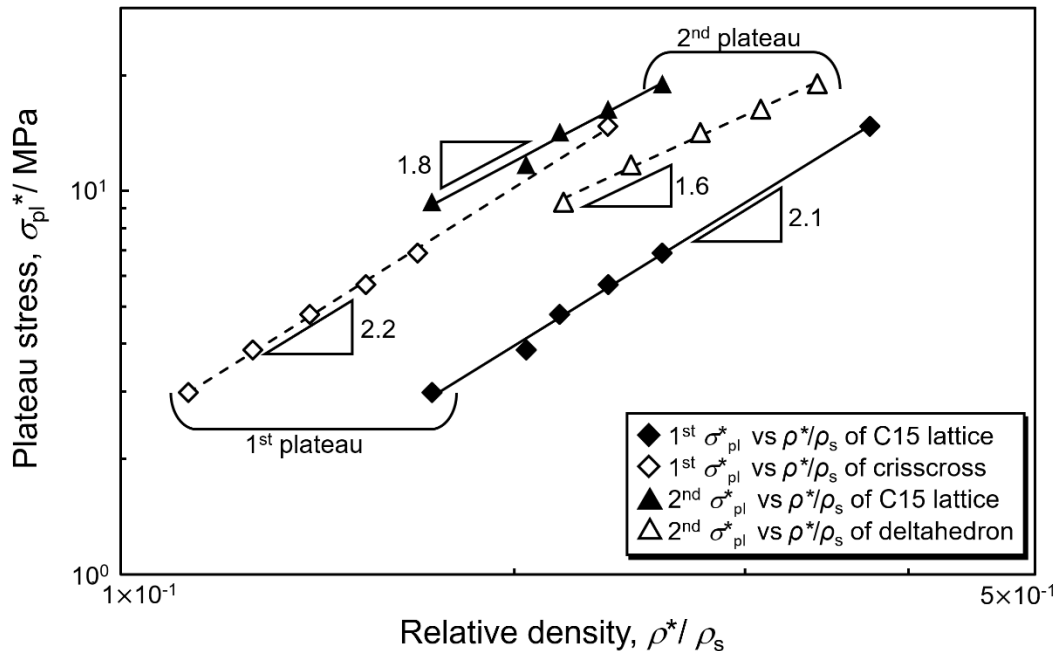


Fig. 4-12 Changes in the plateau stress as functions of overall relative density of C15 lattice structure and local relative density of crisscross and deltahedron units.

stress for both lattice structure and deltahedron unit were obviously lower than those for the 1st plateau stress. In the 2nd plateau region, the crisscross units perpendicular to the loading direction were densified, while the deltahedron units mainly experienced plastically large deformation. The deltahedron unit has 99 struts, 26 nodes, and positive Maxwell number value of 27, suggesting the stretch-dominated deformation behavior. It is reported that stretch-dominated lattice structures consisting of octet truss unit cells exhibited the relationship of $\sigma_{pl}^* \propto (\rho^*/\rho_s)^{1.3\sim 1.7}$ [15, 16]. The exponent value of 1.6 for the 2nd plateau stress against the local relative density of deltahedron units showed good agreement with reported octet lattice structures, which indicate that the deltahedron units deformed in stretch-dominated mode during the 2nd plateau region.

In order to further confirm the deformation mode in crisscross and deltahedron units, the principal stress distributions on the surface of struts in C15 lattice model at the nominal strains of 3% obtained by FEM are illustrated in **Figure 4-13**. The struts in crisscross and deltahedron units in dotted squares are enlarged. The tension (T) and compression (C) are illustrated in red and blue arrows, respectively. For the struts in crisscross units, it is observed that the regions in tension and those in compression occur in pairs near nodes [17]. The same side of strut bears tensile and compressive stress at the two ends, which indicates a S-curved bending deformation behavior and demonstrates in **Fig. 4-10**. This phenomenon is similar to the deformation behavior of the struts in bending-dominated BCC lattice structure as shown in **Figs. 3-5 and 3-7** in Chapter 3. In contrast, tensile or compressive stress only is distributed on the representative struts in deltahedron units magnified in **Fig. 4-13**. Almost all the stress vectors are along the axial direction of struts, indicating the stretching behavior. Before entering the 2nd plateau region, all the deltahedron units hardly deformed (**Fig. 4-10 (a)**). It is believed that the deltahedron units at early stage of the 2nd plateau region exhibit similar principal stress distribution but different stress level compared to the initial deformation stage, implying the stretch-dominated deformation of deltahedron units at 2nd plateau region. Therefore, based on the results by simulation of stress distribution and experiments according to the Gibson-Ashby equation and Maxwell stability criterion, the designed C15 lattice structures can be considered as a hybrid structure composed of two unit cell types of crisscross and deltahedron, which have grade local relative densities and different deformation behaviors of bending- and stretch-dominated modes.

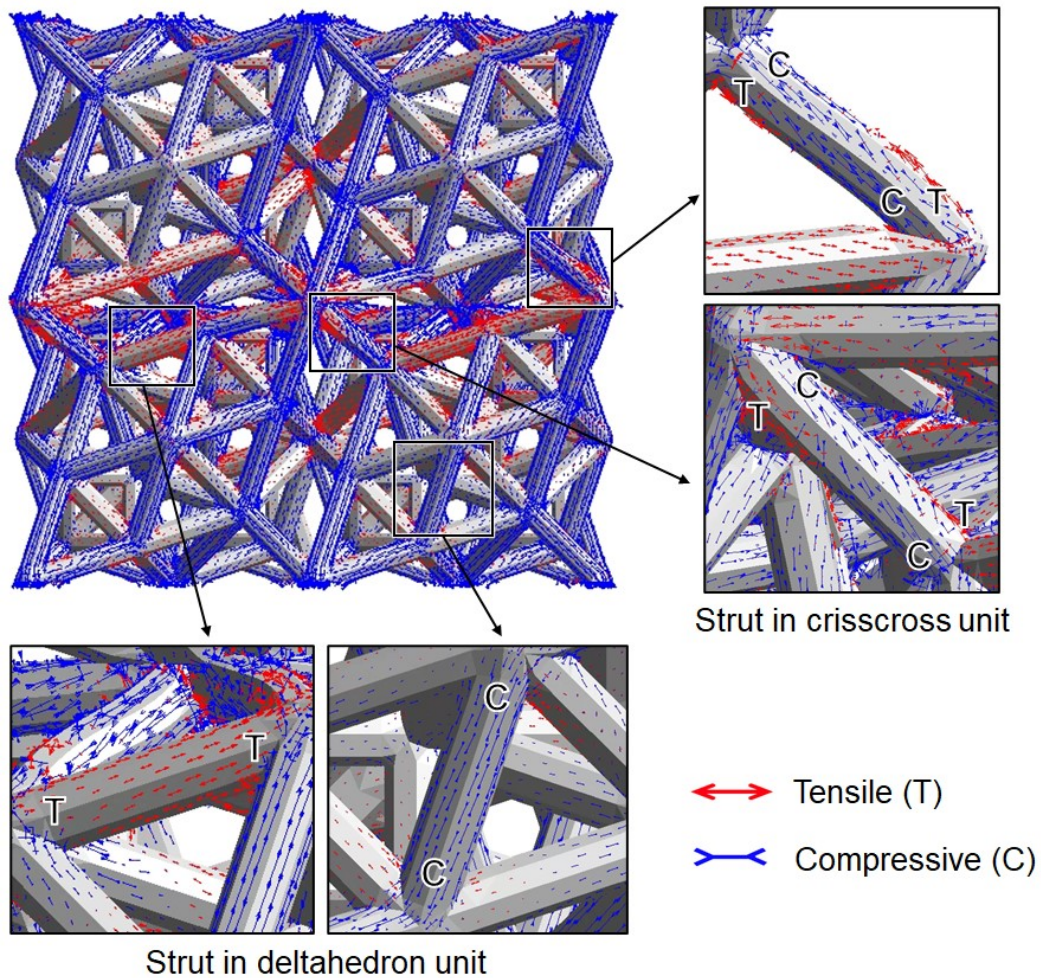


Fig. 4-13 Principal stress distributions on the surfaces of struts in C15 lattice model at the nominal strains of 3%. The tension and compression are illustrated in red and blue arrows, respectively. The struts in crisscross and deltahedron unit in squares are enlarged.

It has been reported that the multiple plateau regions appeared in the stress–strain responses of density-graded [18] or layered-hybrid [19] lattice structures. However, the property of multiple plateaus in these lattice structures is limited to the specific loading direction, because of the anisotropic strut distribution and the graded relative density present in one specific direction. On the contrary, the C15 lattice structures proposed here can display two plateau regions under different compressive loading directions, as a result of the alternate arrangement of crisscross and deltahedron unit in 3-dimensions. Furthermore, the two graded plateau stresses can be also controlled by altering the strut diameters in the two different units separately. The influences of loading directions and controlled strut diameters on the

mechanical property and deformation behavior of the C15 lattice structures need to be further clarified.

4.4 Conclusions

In this chapter, the lattice structures were designed by mimicking C15-type TCP structure as well as diamond crystal structure for comparison, and manufactured via L-PBF process using Al–12Si powder. The compression tests, X-ray CT scan and FEM analysis were carried out to investigate mechanical properties and deformation behaviors of lattice structures. Based on the results, the following conclusions were drawn:

- (1) The diamond lattice structure displayed a common compressive behavior of cellular structures. The C15-type TCP lattice structures with various relative densities exhibited two plateau regions with graded stress level.
- (2) The C15 lattice structure with the relative density of 0.22 exhibited high energy absorption capacity of $5.0 \text{ MJ} \cdot \text{m}^{-3}$.
- (3) The two plateau regions in C15 lattice structures were attributed to the two different units of crisscross and deltahedron with graded relative densities.
- (4) Crisscross units preferentially exhibited a bending-dominated deformation behavior in 1st plateau, and subsequently deltahedron units exhibited a stretch-dominated deformation behavior in 2nd plateau, suggesting the hybrid deformation mode of C15 lattice structures.
- (5) The lattice structures with various polyhedron units inspired by other TCP intermetallics would exhibit multi-plateau regions with controlled stress levels.

References

- [1] X. Li, Y.H. Tan, H.J. Willy, P. Wang, W. Lu, M. Cagirici, C.Y.A. Ong, T.S. Herng, J. Wei, J. Ding, Heterogeneously tempered martensitic high strength steel by selective laser melting and its micro-lattice: Processing, microstructure, superior performance and mechanisms, *Mater. Des.* 178 (2019) 107881.
- [2] Y. Liu, J. Zhang, X. Gu, Y. Zhou, Y. Yin, Q. Tan, M. Li, M.X. Zhang, Mechanical performance of a node reinforced body-centred cubic lattice structure manufactured via selective laser melting, *Scr. Mater.* 189 (2020) 95–100.
- [3] M.S. Pham, C. Liu, I. Todd, J. Lertthanasarn, Damage-tolerant architected materials

- inspired by crystal microstructure, *Nature* 565 (2019) 305–311.
- [4] J. Nei, K. Young, S.O. Salley, K.Y.S. Ng, Determination of C14/C15 phase abundance in Laves phase alloys, *Mater. Chem. Phys.* 136 (2012) 520–527.
- [5] F. Stein, A. Leineweber, Laves phases: a review of their functional and structural applications and an improved fundamental understanding of stability and properties, *J. Mater. Sci.* 56 (2021) 5321-5427.
- [6] A. Yakoubi, O. Baraka, B. Bouhafis, Structural and electronic properties of the Laves phase based on rare earth type BaM₂ (M= Rh, Pd, Pt), *Results Phys.* 2 (2012) 58–65.
- [7] H. Soul, P. Terriault, V. Brailovski, The static and fatigue behavior of AlSiMg alloy plain, notched, and diamond lattice specimens fabricated by laser powder bed fusion, *J. manuf. mater.* 2 (2) (2018) 25.
- [8] M.F. Ashby, The properties of foams and lattices, *Philos. Transact. A Math. Phys. Eng. Sci.* 364 (2006) 15–30.
- [9] X. Li, Y.H. Tan, P. Wang, X. Su, H.J. Willy, T.S. Herng, J. Ding, Metallic microlattice and epoxy interpenetrating phase composites: Experimental and simulation studies on superior mechanical properties and their mechanisms, *Compos. Part A Appl. Sci. Manuf.* 135 (2020) 105934.
- [10] B. Lozanovski, D. Downing, P. Tran, D. Shidid, M. Qian, P. Choong, M. Brandt, M. Leary, A Monte Carlo simulation-based approach to realistic modelling of additively manufactured lattice structures, *Addit. Manuf.* 32 (2020) 101092.
- [11] T. Tancogne-Dejean, D. Mohr, Stiffness and specific energy absorption of additively-manufactured metallic BCC metamaterials composed of tapered beams, *Int. J. Mech. Sci.* 141 (2018) 101–116.
- [12] X. Zheng, H. Lee, T.H. Weisgraber, M. Shusteff, J. DeOtte, E.B. Duoss, J.D. Kuntz, M.M. Biener, Q. Ge, J.A. Jackson, S.O. Kucheyev, N.X. Fang, C.M. Spadaccini, Ultralight, ultrastiff mechanical metamaterials, *Science* 344 (6190) (2014) 1373–1377.
- [13] H. Inui, N.L. Okamoto, S. Yamaguchi, Crystal Structures and Mechanical Properties of Fe–Zn Intermetallic Compounds Formed in the Coating Layer of Galvannealed Steels, *ISIJ Int.* 58 (9) (2018) 1550–1561.
- [14] O. Al-Ketan, R.K.A. Al-Rub, R. Rowshan, The effect of architecture on the mechanical properties of cellular structures based on the IWP minimal surface, *J. Mater. Res.* 33(3)

(2018) 343–359.

- [15] O. Al-Ketan, R. Rezgui, R. Rowshan, H. Du, N.X. Fang, R.K.A. Al-Rub, Microarchitected stretching - dominated mechanical metamaterials with minimal surface topologies, *Adv. Eng. Mater.* 20 (9) (2018) 1800029.
- [16] O. Al-Ketan, R. Rowshan, R.K.A. Al-Rub, Topology-mechanical property relationship of 3D printed strut, skeletal, and sheet based periodic metallic cellular materials, *Addit. Manuf.* 19 (2018) 167–183.
- [17] L. Yang, C. Yan, W. Cao, Z. Liu, B. Song, S. Wen, C. Zhang, Y. Shi, S. Yang, Compression–compression fatigue behaviour of gyroid-type triply periodic minimal surface porous structures fabricated by selective laser melting, *Acta Mater.* 181 (2019) 49–66.
- [18] W. Van Grunsven, E. Hernandez-Nava, G.C. Reilly, R. Goodall, Fabrication and mechanical characterisation of titanium lattices with graded porosity, *Metals* 4 (3) (2014) 401–409.
- [19] S. Li, M. Hu, L. Xiao, W. Song, Compressive properties and collapse behavior of additively-manufactured layered-hybrid lattice structures under static and dynamic loadings, *Thin-Walled Struct.* 157 (2020) 107153.

5. Hybrid lattice structures composed of different unit cells

5.1 Introduction

The topologies and arrangements of unit cells are the key factors to control the mechanical performances of lattice structures. The improved weight-to-strength efficiency and energy absorption capacity as well as suppressed detrimental shear band formation can be achieved by varying unit cell types and strut geometry. Nevertheless, new designs of lattice structure solely relying on changing unit cell types limit the boundary of various mechanical responses. Heterogeneous lattice structures consisting of different unit cells or grade relative densities have been explored for the improvement of mechanical performances compared to homogeneous lattice structures. Mirzaali et al. [1] reported that the patterned randomness of auxetic and conventional unit cells was applied to yield high elastic modulus and negative Poisson's ratio. Kang et al. [2] suggested that the multi-lattice structures with two unit cell types of BCC and octet exhibit superior stiffness and strength than uniform lattice structures. Alberdi et al. explored the multi-morphology lattice structures composed of different unit cells to enhance the energy-absorbing property. Hybrid structures of auxetic-strut and honeycomb proposed by Ingrole et al. exhibited better mechanical properties than the regular lattice structures [3]. Xue et al. [4] designed the dual scale hybrid lattice structures consisting of three kinds of unit cells and investigated their mechanical properties. The results of experiment and FEM revealed the improved specific strength, stiffness and energy-absorbing capacity. Lei et al. [5] proposed the heterogeneous lattice structures with hybrid arrangement patterns based on natural biology, indicating that the arrangement patterns significantly influenced the load-bearing capacities and deformation behaviors. The layered-hybrid lattice structures composed of octet-truss and modified re-entrant hexagon unit cells exhibiting distinctive deformation mode demonstrated the potential application as protective components [6]. Pham et al. [7] demonstrated the possibilities to enhance the functionality and performance of lattice structures with the combination of multiple unit cell architectures from the inspiration of crystal microstructure. In Chapter 4, C15 lattice structure was identified as a hybrid consisting of crisscross and deltahedron units. Under compression, crisscross units preferentially exhibited a bending-dominated deformation behavior in 1st plateau, and subsequently deltahedron units exhibited a stretch-dominated deformation behavior in 2nd plateau, demonstrating a combined

deformation mode. More unique properties like the C15 lattice structure should be uncovered by designing hybrid lattice structures. For the C15 lattice structure as a hybrid, the crisscross and deltahedron units were alternately arranged in three dimensions. The influences of spatial arrangement patterns on the mechanical property and deformation behavior are required to be further investigated.

The lattice structures consisting of BCC unit cells (common bending-dominated counterpart) normally exhibit stable post-yield plateau stress, but less mechanical efficiency with lower strength compared to stretch-dominated lattice structure, such as octet truss (also referred to as FCC according to the design strategy by connecting the first-nearest-neighbor nodes). However, FCC stretch-dominated lattice structure often collapsed in an unfavorable behavior with localized shear band along a specific plane, as indicated in **Fig. 3-11** in Chapter 3. It is believed that heterogeneous strut arrangement on the potential shear band plane may restrain the shear band formation [7], which can be achieved by hybrid structure with heterogeneous spatial layout of different unit cell. The hybrid lattice structure composed of bending- and stretch-dominated unit cells may also guarantee the enhancement in stress level of bending-dominated structure. Therefore, the hybrid lattice structure was proposed in this chapter by combining bending-dominated BCC and stretch-dominated FCC unit cells to take advantage and avoid disadvantage of each. The effect of four spatial distribution patterns of the different unit cells on the mechanical property and deformation behavior in hybrid lattice structure were investigated. L-PBF process was applied for the fabrication of Al–12Si lattice structure. Full and interrupted compression tests, X-ray CT observations and FEM analysis were conducted.

5.2 Materials and methods

Figure 5-1 presents the schematic illustrations and photographs of L-PBF fabricated BCC and FCC lattice structures as well as their hybrid lattice structures. These lattice structures were manufactured and compression loaded along Z direction. The half pieces of both BCC and FCC lattice structures were combined with the interface parallel to the Z direction, resulting in the hybrid lattice structure referred to as Parallel hybrid 1. The second hybrid composed of layers of BCC and FCC unit cells in an alternate and parallel arrangement pattern, which was denoted as Parallel hybrid 2. Similarly, the vertical arrangement of BCC and FCC unit cell layers revealed the Vertical hybrid. The classic mixture rules for predicting the properties of composite

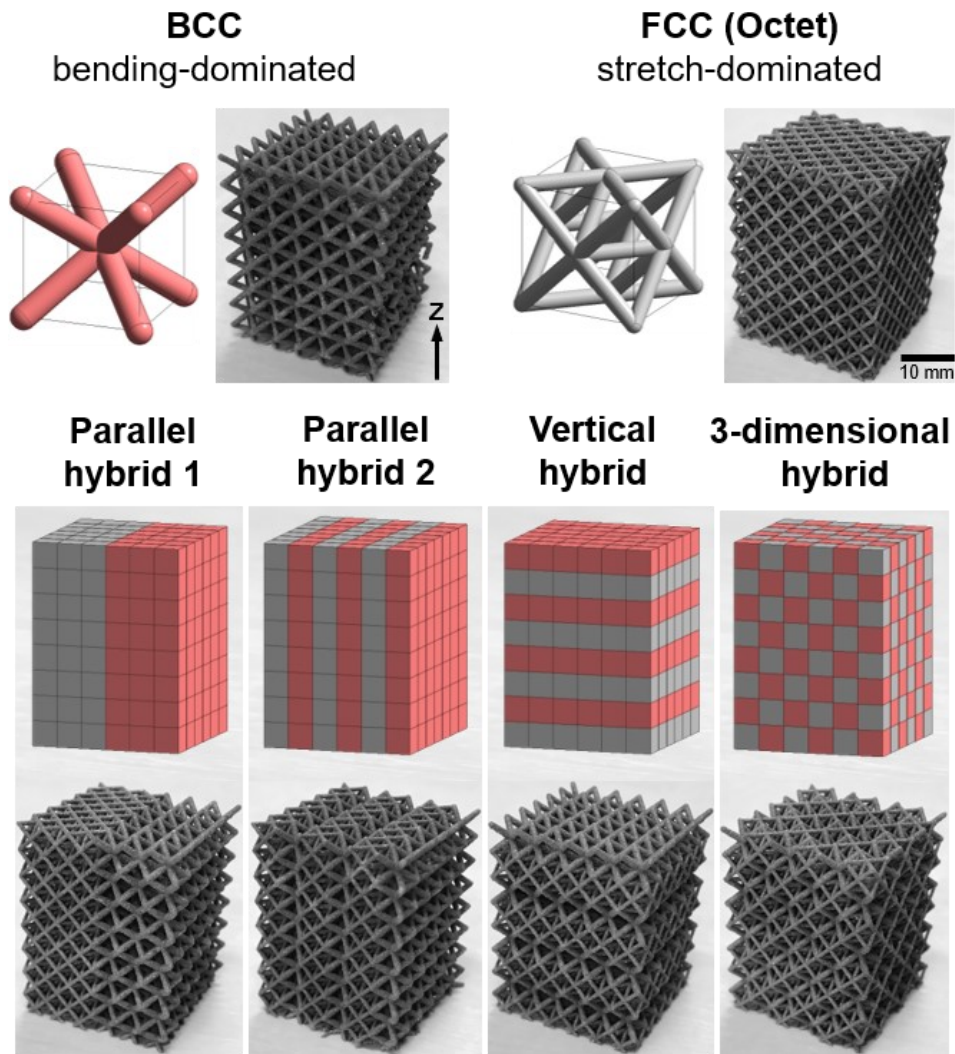


Fig. 5-1 Schematic diagrams and photos of L-PBF fabricated lattice structures of parallel hybrid 1, parallel hybrid 2, vertical hybrid, and 3-dimensional hybrid compared with BCC and FCC control lattice structures.

materials including Voigt model (axial loading) [8] and Reuss model (transverse loading) [9] corresponded to the parallel and vertical hybrid lattice structures. The 3-dimensional hybrid has the spatial patterns of BCC and FCC unit cells arranged alternately in three dimensions. The mixing ratio of BCC to FCC unit cells was 1:1 for all hybrid lattice structures. The diameters of struts in BCC and FCC unit cells were determined to be 0.46 mm and 0.28 mm, respectively, to ensure the same relative density of BCC and FCC unit cell. The L-PBF process using Al-12Si alloy raw powder was applied to fabricate lattice structures. These lattice structures have the same cuboid geometry of $28 \times 28 \times 35 \text{ mm}^3$. The detailed processing conditions and

post-treatment are same as used in Chapter 3. The measured relative densities of built specimens were approximately 0.19. Compression tests and X-ray CT scan were carried out, as the details indicated in Chapter 3. FEM was conducted by establishing a reduced C15 lattice model consisting of 96 unit cells ($x \times y \times z = 4 \times 4 \times 6$), as shown in **Fig. 5-2**. The forced displacement corresponding to 1% height of lattice models were applied on the top plane along the Z direction. The input material properties, mesh, boundary conditions have been shown in Chapter 3.

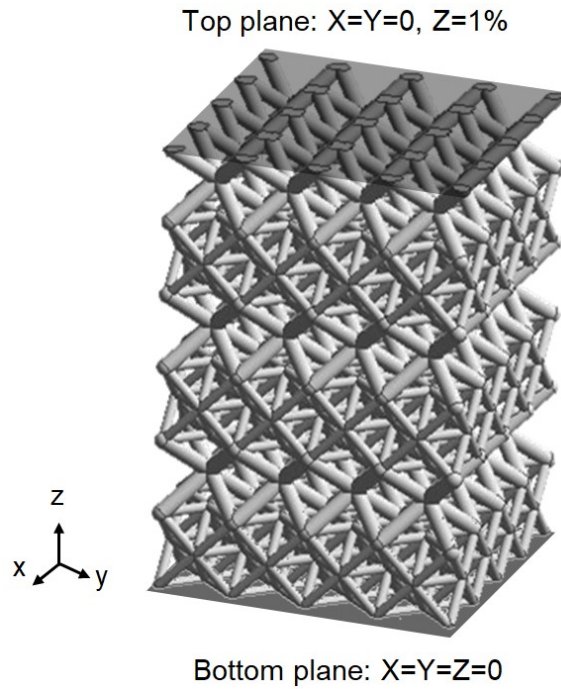


Fig. 5-2 An example of hybrid lattice model for FEM and applied boundary conditions.

5.3 Results and discussion

Figure 5-3 presents the normalized stress–strain responses of homogeneous BCC and FCC lattice structures, and heterogeneous hybrid lattice structures. Homogeneous BCC and FCC lattice structures exhibited typical stress–strain responses of bending- and stretch-dominated lattice structures [10]. The BCC lattice structure had a flat plateau region, while the FCC lattice structures experienced post-yield softening after reaching the initial peak stress and subsequent plateau region with stress fluctuations. In the four hybrid lattice structures, the distinct difference in stress–strain curves indicates that the spatial arrangement patterns play an important role in mechanical properties of hybrids. The stress levels of plateau regions for all

the hybrids seem to be between the plateau stresses of BCC and FCC lattice structures. The curves of both Parallel hybrid 1 and 2 experienced prominent stress drop, the overall trend of them is similar to the FCC lattice structure. It is noteworthy that the Parallel hybrid 2 underwent the decrease of stress only once and maintained almost constant stress level in the nominal strain range of 16.5~43.3%. In the Vertical hybrid and 3-dimensional hybrid, the stress–strain curves were relatively smooth, indicating more stable mechanical behavior in the plateau regions.

The test appearances showing the deformation behavior of compressed lattice structures at 30% nominal compressive strain are illustrated in **Fig. 5-4**. The shear band-like localizations of

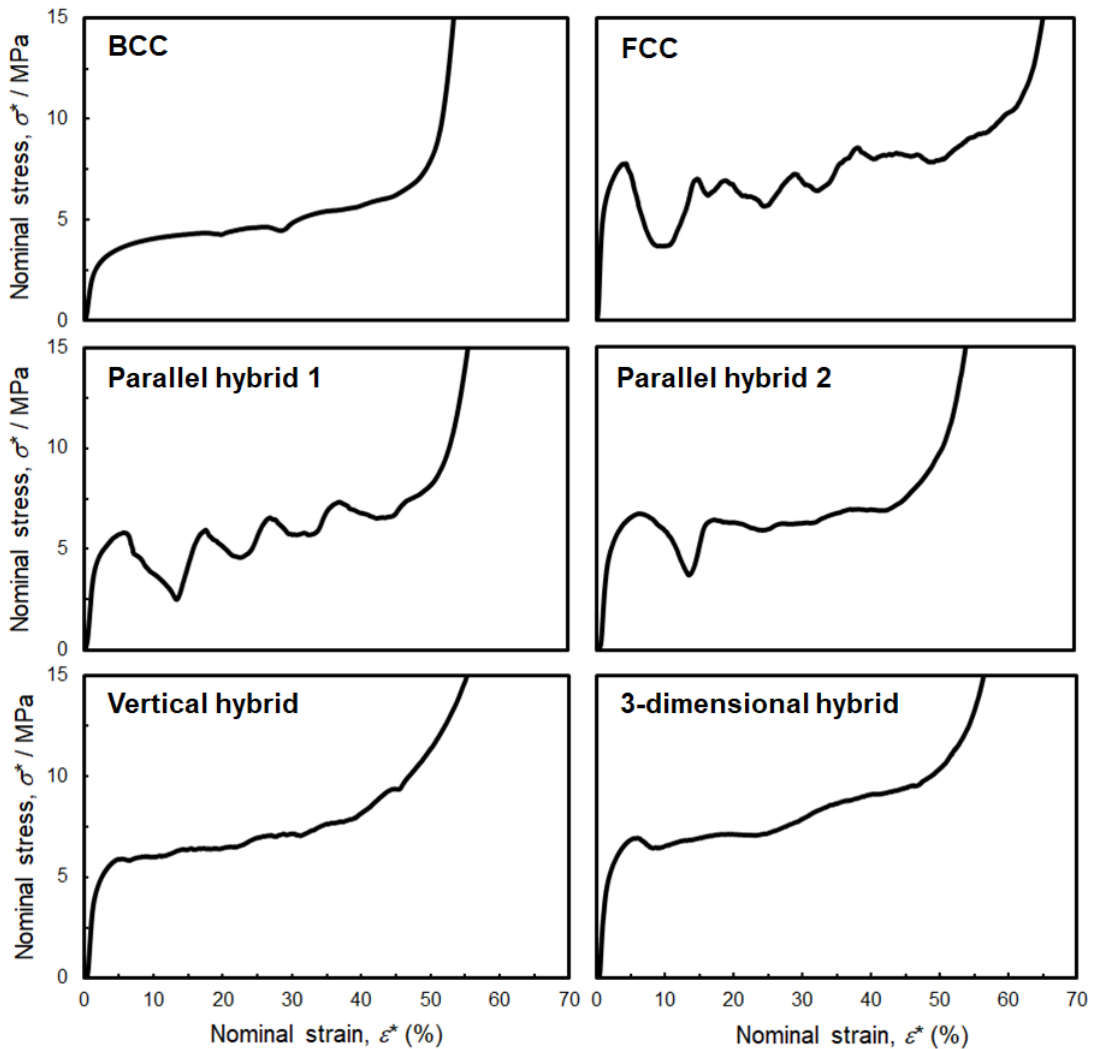


Fig. 5-3 Compressive stress–strain responses of BCC, FCC, and their hybrid lattice structures.

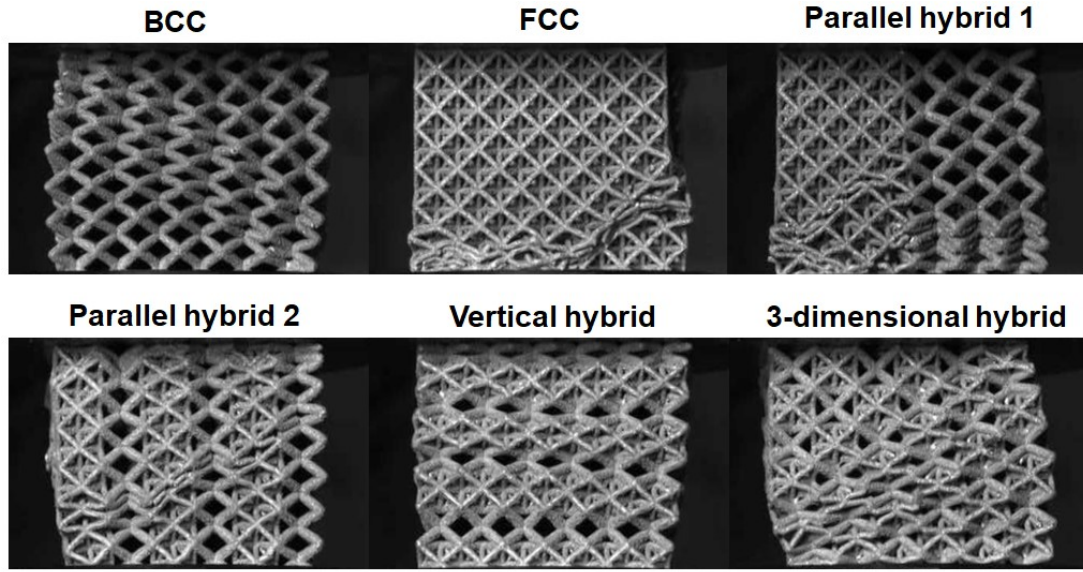


Fig. 5-4 Test appearance of the lattice structures at 30% nominal strain.

struts were visible in FCC and the two Parallel hybrid lattice structures, which caused the stress instability in plateau regions as shown in **Fig. 5-3**. BCC and 3-dimensional hybrid lattice structures slightly inclined as a result of ununiform but gentle deformation of struts. For the Vertical hybrid, it seems that the deformation concentrated at the top layers of unit cells, whereas the large deformation was less noticeable in lower layers. However, the test appearances cannot provide comprehensive understanding of deformation behavior of lattice structures, due to that the most struts are invisible inside the lattices. Further investigations by performing X-ray CT scan on the lattice structures subjected to compression loading which was interrupted at different strain levels were carried out and discussed later.

According to the rule-of-mixture of composite materials, the theoretical properties such as elastic modulus and yield strength are given by Voigt upper bound and Reuss lower bound. The performances of the hybrid lattice structures in this study composed of BCC and FCC unit cells were predicted using the mixture rule. The Voigt upper bounds corresponding to the Parallel hybrid lattice structures are expressed as follows.

$$E_{\text{hybrid}} = E_{\text{BCC}} \cdot V_{\text{BCC}} + E_{\text{FCC}} \cdot V_{\text{FCC}} \quad (5.1)$$

$$\sigma_{\text{hybrid}} = \sigma_{\text{BCC}} \cdot V_{\text{BCC}} + \sigma_{\text{FCC}} \cdot V_{\text{FCC}} \quad (5.2)$$

The Reuss lower bounds corresponding to the Vertical hybrid lattice structures are given by

$$E_{\text{hybrid}} = (V_{\text{BCC}} / E_{\text{BCC}} + V_{\text{FCC}} / E_{\text{FCC}})^{-1} \quad (5.3)$$

$$\sigma_{\text{hybrid}} = (V_{\text{BCC}} / \sigma_{\text{BCC}} + V_{\text{FCC}} / \sigma_{\text{FCC}})^{-1} \quad (5.4)$$

where E and σ represent the elastic modulus and yield strength of hybrid lattice structure and homogeneous BCC and FCC lattice structures, and V denoted the volume fractions of BCC or FCC unit cells in hybrid lattice structures. As the mixing ratio of BCC to FCC unit cells is 1:1, the volume fraction for both BCC (V_{BCC}) and FCC (V_{FCC}) is 0.5.

The quantified elastic modulus and yield strength of all lattice structures obtained by experiments are compared to the predicted values based on rule-of-mixture according to **Eq. 5.1-4**, as shown in **Fig. 5-5**. The yield strength is calculated by the apparent 0.2% proof stress. It is apparent that the experimental elastic moduli of three hybrid lattice structures were generally in the range of upper- and lower-bounds by the rule-of-mixture. However, the Parallel hybrid lattice structures corresponding to the Voigt model exhibited lower elastic modulus than the

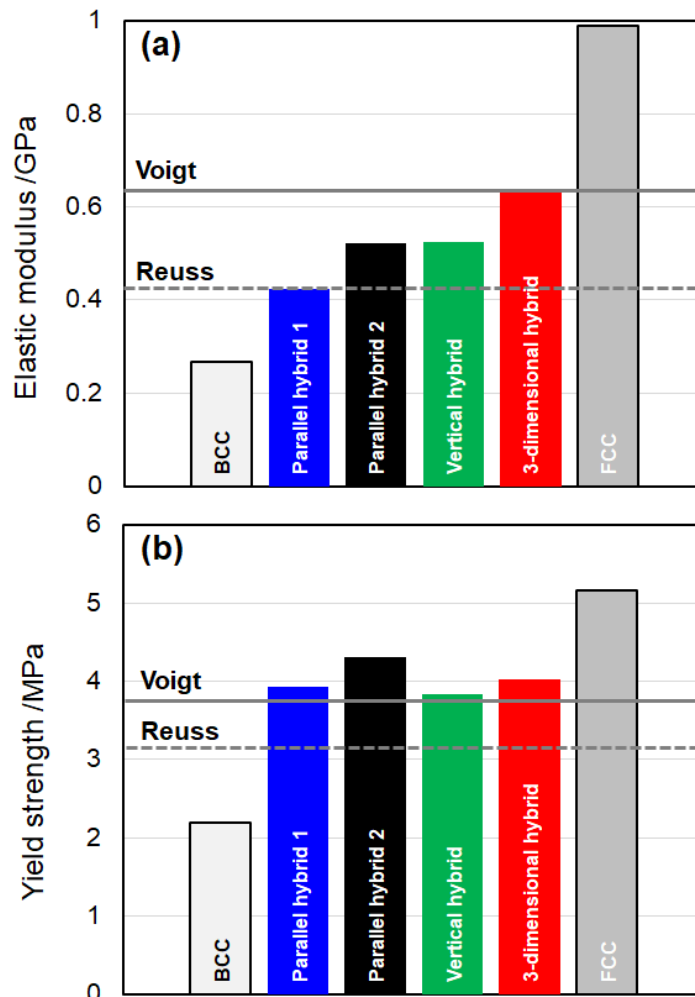


Fig. 5-5 Elastic modulus and yield strength compared with Voigt upper bound and Reuss lower bound.

upper-bound, especially the elastic modulus for the Parallel hybrid 1 met the Reuss lower-bound. Additionally, Vertical hybrid corresponding to the Reuss model showed higher elastic modulus than the lower-bound, and 3-dimensional hybrid had the elastic modulus reaching the upper-bound. In terms of yield strength (**Fig. 5-5 (b)**), all the experimental values exceed the upper-bound of prediction value, as also indicated by Alberdi et al. [11]. The yield strength of Parallel hybrid 2 was approximately 17% higher than the upper-bound value. The discrepancy between the experimental and predicted values demonstrates that the traditional rule-of-mixture is not suitable for evaluating the mechanical properties of hybrid lattice structures. The parallel result is found in reported study [5]. The reason attributed to the deviation by rule-of-mixture needs to be further investigated.

The energy absorption capacity of lattice structure is usually quantified by integrating the compressive stress–strain curve. **Figure 5-6** shows the changes in energy per unit volume of tested lattice structures with the nominal strain up to 50%. At the early compression stage with the nominal strain less than 10%, the FCC lattice structure had the highest energy per unit volume as a result of large elastic modulus and yield strength (**Figs. 5-3 and 5-5**). The hybrid

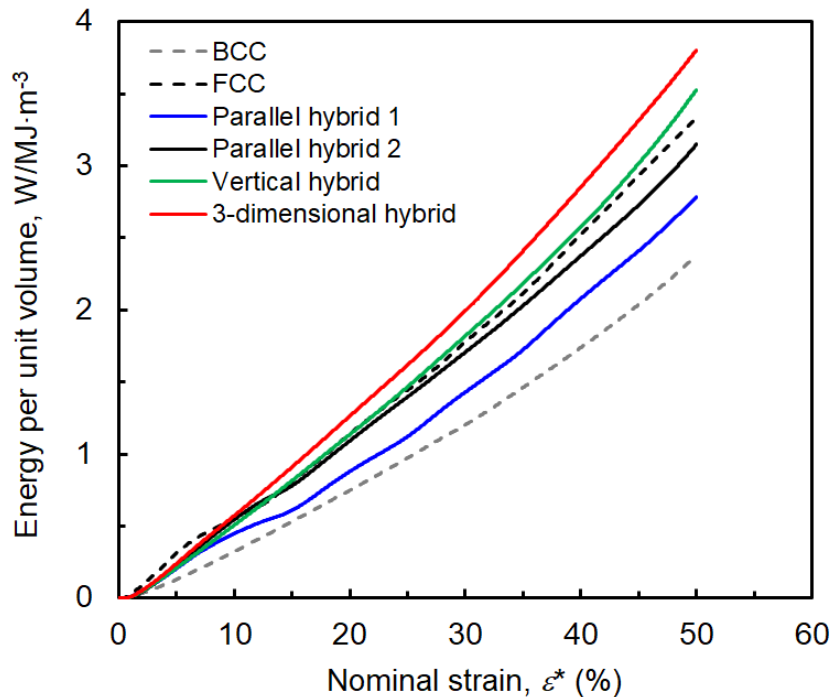


Fig. 5-6 Relationships between the energy absorption capacity and nominal strain of lattice structures.

lattice structures exhibited lower capacities than FCC but higher than BCC lattice structure. With an increase in nominal strain, the energy absorption capacities of Vertical hybrid and 3-dimensional hybrid gradually exceeded that of FCC lattice structure. While the two Parallel hybrids still showed lower energy absorption capacity, especially for Parallel hybrid 1, although their yield strengths were higher than those of Vertical hybrid and 3-dimensional hybrid. This phenomenon is due to that the unstable stress–strain curves with drops significantly deteriorated the absorbing energy. The 3-dimensional hybrid lattice structure with stable high plateau stress exhibited the highest energy absorption capacity of $3.8 \text{ MJ}\cdot\text{m}^{-3}$ at the 50% nominal strain, experiencing a 14% increase compared to the homogeneous FCC lattice structure. Therefore, the designs of hybrid lattice structures are beneficial to energy absorption improvement by maintaining high stress level and stable plateau region. The stable plateau region is achieved by the moderate deformation behavior suppressing drastic shear band failure. Thus, the effect of spatial arrangement patterns of BCC and FCC unit cells on the deformation behavior contributing to the mechanical performance of hybrid lattice structure should be clarified.

Figure 5-7 shows the interrupted stress–strain responses and the X-ray CT cross-sectional images of (a) BCC and (b) FCC lattice structures before compression and compressed at different nominal strains, for a better understanding of detailed deformation behavior. The observed cross-sections for BCC and FCC lattice structure were (110) and (010) planes, respectively. In the cross-sectional images of BCC lattice structure (**Fig. 5-7 (a)**), the struts in central unit cells suffered preferential bending deformation behavior. Shear band was not formed due to the fact that significant crack initiations and propagations were not generated on struts at large compressive strain, leading to steady plateau region (**Fig. 5-3**). This result corresponds to the BCC lattice structure with R_d equal to 1 in Chapter 3. In contrast, a distinct shear band formation was identified on the (111) plane in the FCC lattice structure, which is the densest plane of struts, as indicated in **Fig. 3-10 (a)** in Chapter 3.

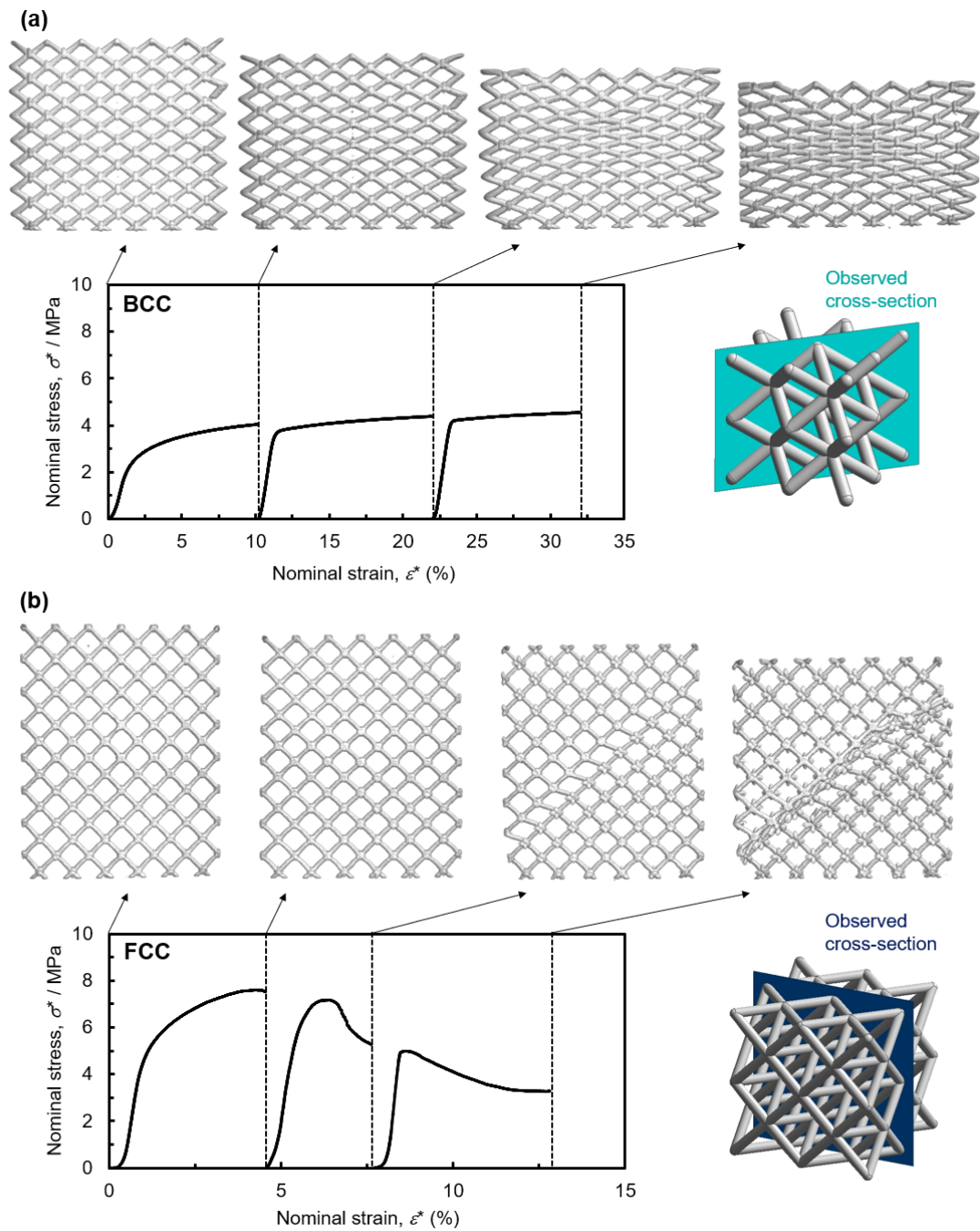


Fig. 5-7. Stress–strain curves derived from the interrupted compression tests and X-ray CT cross-sectional images before compression and compressed at different nominal strains of (a) BCC and (b) FCC lattice structures.

Figure 5-8 shows the X-ray CT images of interruptedly compressed Parallel hybrid 1 lattice structure observed on different cross-sections. The observed cross-sections 1 and 2

included the most struts present in BCC and FCC unit cells, respectively. The struts in BCC unit cells exhibited uniform deformation behavior, no crack or fracture was observed. However, the shear band formation appeared on the FCC half part in the hybrid lattice structure as illustrated in cross-section 2 images. The large deformation on the shear band plane led to the fracture of red circle-marked regions by shearing the horizontal struts. Based on these images of Parallel hybrid 1 lattice structure, it is clear that the shear band formation in FCC unit cells was not suppressed by the presence of BCC unit cells and did not trigger the shear behavior in BCC unit cells either at this compression stage.

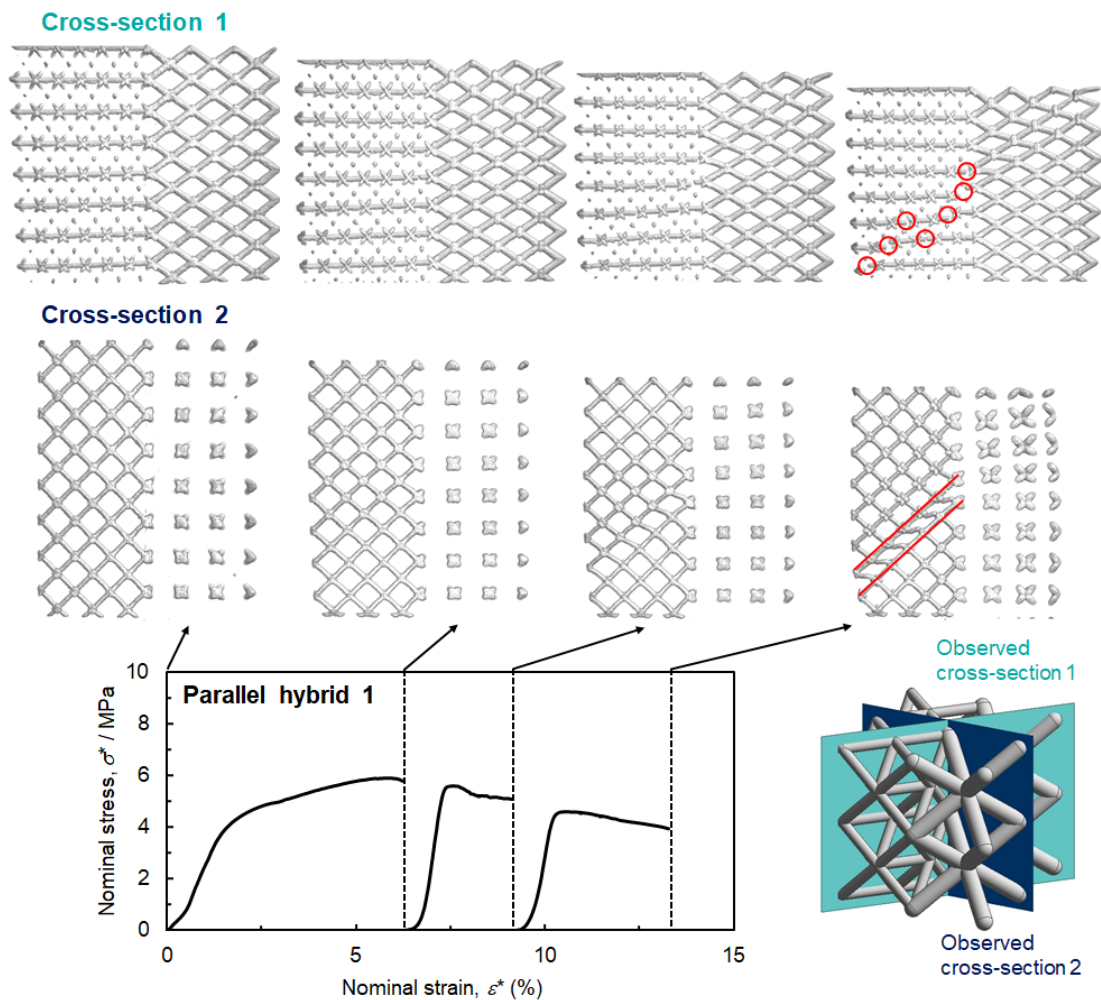


Fig. 5-8 Stress–strain curves derived from the interrupted compression tests and X-ray CT cross-sectional images of Parallel hybrid 1 lattice structure before compression and compressed at different nominal strains.

For Parallel hybrid 2 lattice structure, both cross-section 1 and 2 showing the BCC and FCC struts exhibited obvious shear band formations (**Fig. 5-9**). The homogeneous BCC lattice structure deformed without the occurrence of shear band. It can be deduced that the shear behavior in BCC unit cells was caused by the deformation of FCC unit cells. In addition, the plane shear band occurred in the X-ray CT images of cross-section 1 of this hybrid was not in accordance with the potential shear band plane with the densest strut arrangement (**Fig. 3-5 (a)** in Chapter 3), further suggesting that the shear band in BCC unit cell was not driven by itself. In

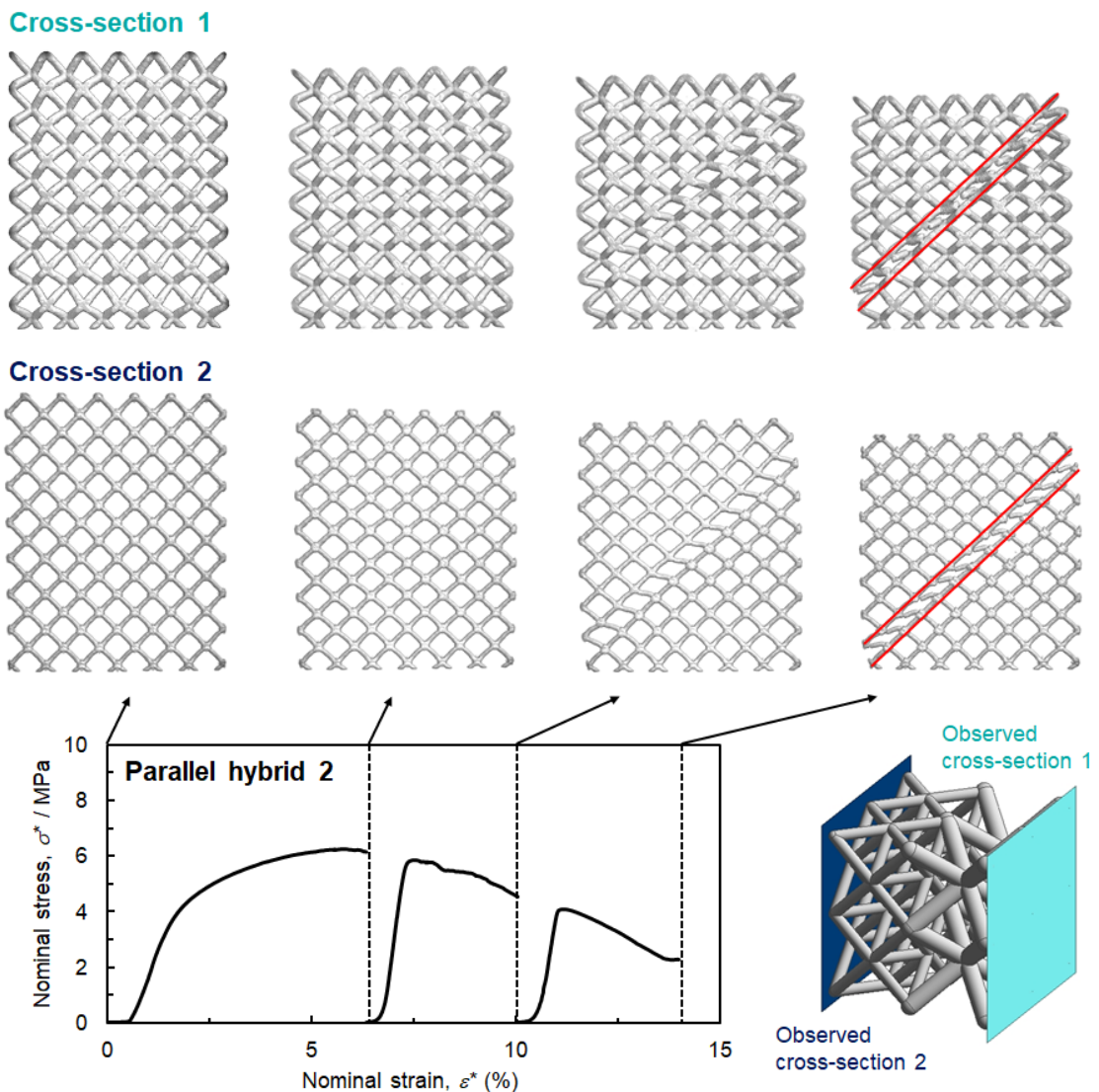


Fig. 5-9 Stress–strain curves derived from the interrupted compression tests and X-ray CT cross-sectional images of Parallel hybrid 2 lattice structure before compression and compressed at different nominal strains.

comparison to the Parallel hybrid 1, the Parallel hybrid 2 lattice structure with alternate arrangement pattern displayed stronger interactions between the BCC and FCC unit cells. As a result, the stress drops were much significantly reduced in Parallel hybrid 2 (with higher energy capacity) than the Parallel hybrid 1 lattice structure (**Fig. 5-3**), despite the fact that shear band was induced in the BCC unit cells in Parallel hybrid 2 rather than Parallel hybrid 1 lattice structure (**Figs. 5-8 and 5-9**).

For Vertical hybrid lattice structure, it is well recognized from the two cross-sections that the struts deformed in a localized behavior but not in a shear band pattern (**Fig. 5-10**). When the compression test was firstly interrupted at 6.1% nominal strain, the X-shaped struts

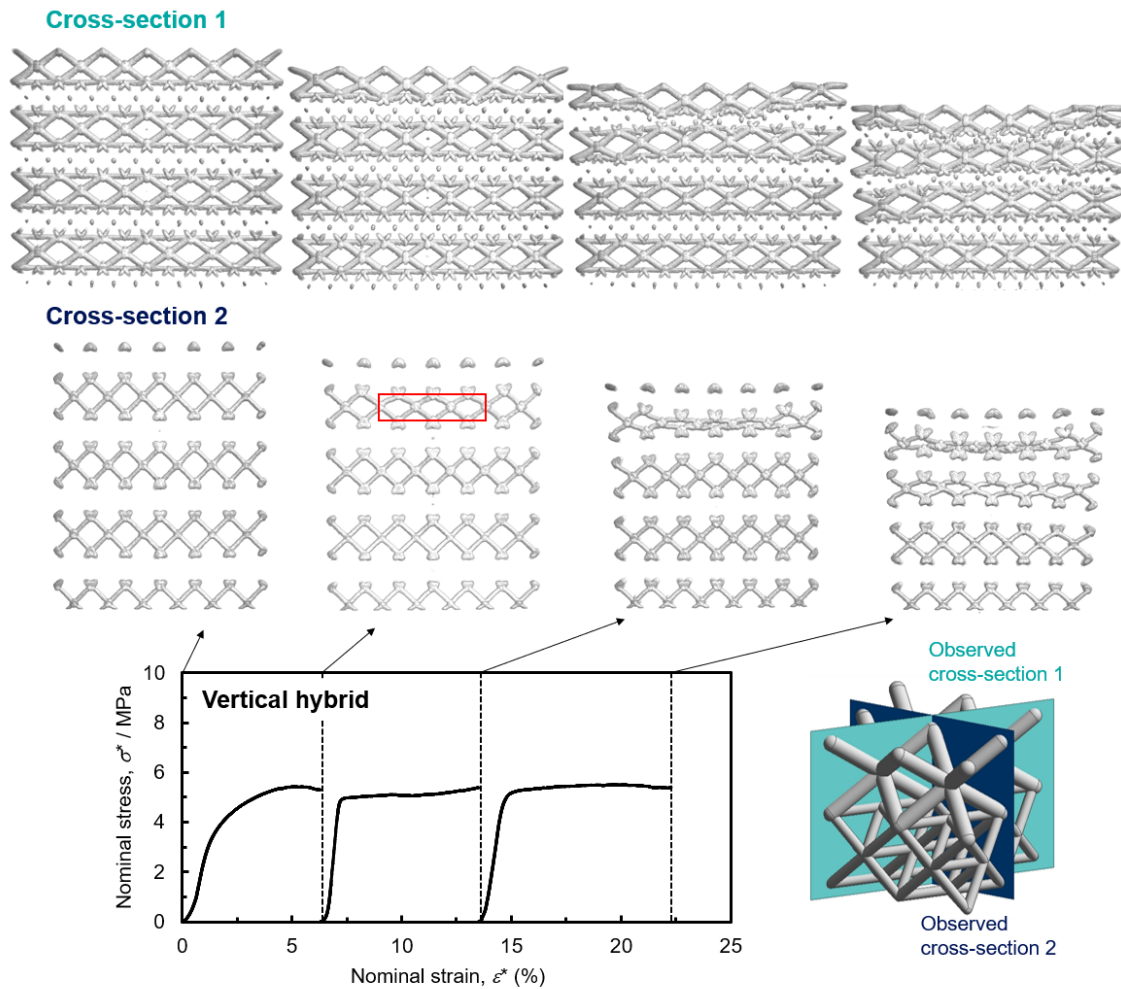


Fig. 5-10 Stress–strain curves derived from the interrupted compression tests and X-ray CT cross-sectional images of Vertical hybrid lattice structure before compression and compressed at different nominal strains.

(square-marked) aligned in (100) or (010) plane in FCC unit cells were bended at the upper layers of Vertical hybrid lattice structure. Because the applied loading transferred to FCC unit cells through the nodes of BCC unit cells, which differed from the uniform load distribution on FCC struts in (001) plane in the case of Parallel hybrid lattice structures. The moderate deformation in BCC unit cells indicated that the BCC struts were more rigid than the X-shaped struts in FCC unit cells. At the 13.5% nominal strain, X-shaped struts in FCC unit cells at the upper center region in the hybrid suffered severe bending failure (cross-section 2). As a result, the node of FCC struts in (001) plane contacted its upper central node of BCC unit cells (cross-section 1). Meanwhile, the lower layers of BCC and FCC unit cells did not exhibit large

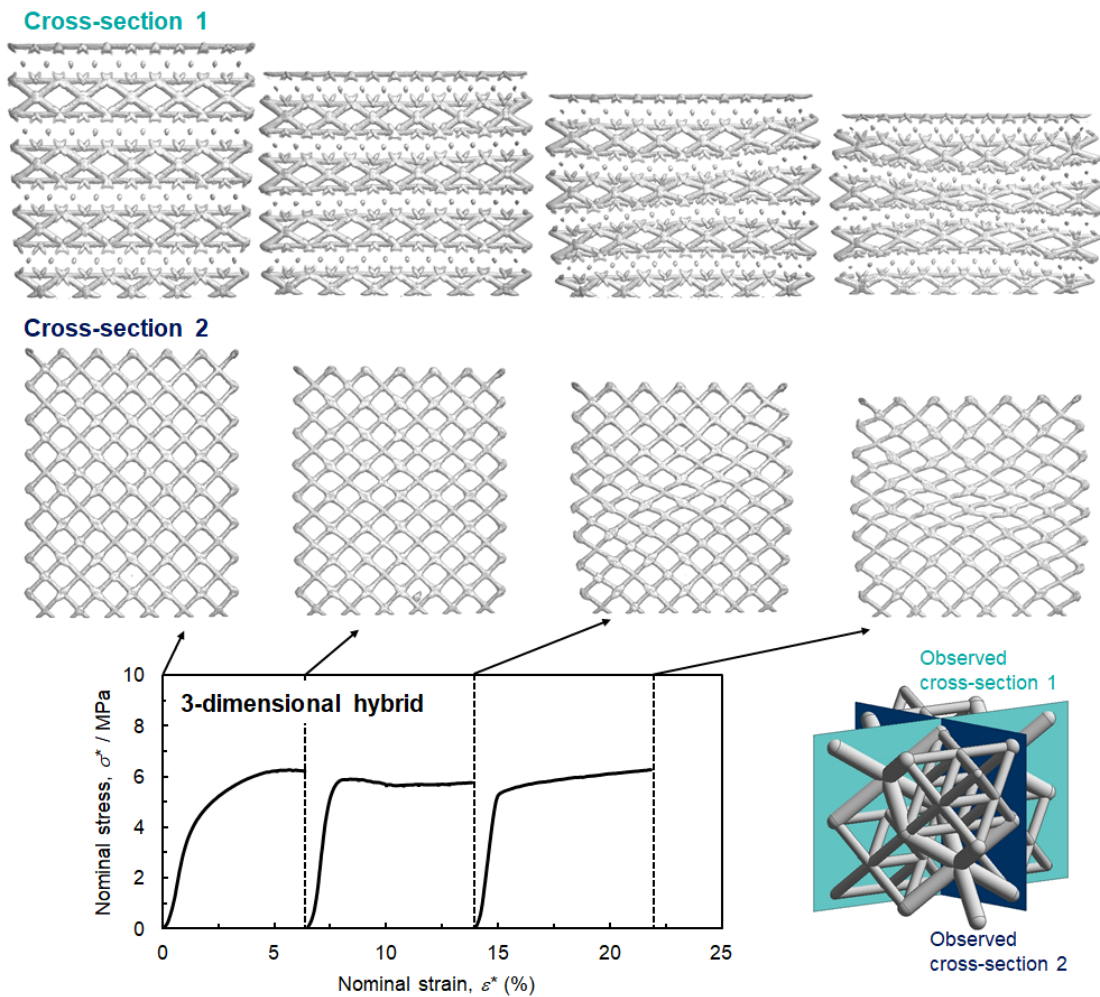


Fig. 5-11 Stress–strain curves derived from the interrupted compression test and X-ray CT cross-sectional images of 3-dimensional hybrid lattice structure before compression and compressed at different nominal strains.

deformation. Continuous compression rendered a gradual spread of concentrated deformation from upper to lower layers (22.2% nominal strain). It is believed that the sequential layer-by-layer collapse without shear band formation was of benefit to the stability of plateau region and energy absorption capacity (**Figs. 5-3 and 5-6**).

In the case of 3-dimensional hybrid lattice structure, a barrel-like deformation pattern was observed (**Fig. 5-11**). The X-shaped struts aligned in (100) or (010) plane in FCC unit cells displayed a preferential bending deformation behavior at the central region, as shown in the cross-sectional 2 images, which were similar to the deformation mode of struts in BCC lattice structure (**Fig. 5-7 (a)**) but different from the that in FCC lattice structure (**Fig. 5-7 (b)**). The images of cross-sectional 1 showing the (110) plane in the 3-dimensional hybrid also indicated the contact between the BCC and FCC nodes at middle height region. Importantly, the 3-dimensional hybrid lattice structure exhibited a relatively uniform global deformation behavior without shear instability, which contributed to the high energy absorption capacity (**Fig. 5-6**).

According to the X-ray CT observations showing the deformation behaviors of lattice structures in **Figs. 5-(7-11)**, it is clear that the spatial arrangement pattern of FCC and BCC unit cells affected the mechanical behaviors associated with distinct deformation modes. The most noteworthy difference among the hybrid lattice structures is that the shear band localization appeared in Parallel hybrid and did not appear in Vertical and 3-dimensional hybrid. This can be ascribed to the parallel (or other) arrangement of FCC unit cells with higher (or lower) tendency to initiate shear behavior. The Parallel hybrids have the diagonal plane in FCC parts corresponding to the preferential shear band plane of homogeneous FCC lattice structure, and has consecutive struts in the shear band direction. In contrast, the existence of BCC unit cells arranged in Vertical and 3-dimensional hybrid obstructed the continuity of strut on the preferential shear band plane of FCC, resulting in the difficulty in the shear band initiation and propagation. Therefore, appropriate arrangement pattern of different unit cells can suppress the shear band formation and simultaneously maintain high plateau stress level, which consequently enhance the capacity of energy absorbing in hybrid lattice structure. In addition, the 3-dimensional hybrid lattice structure with the BCC and FCC unit cells arranged alternately in three dimensions exhibited successive deformation behavior without struts localization and had the highest energy capacity compared to the other lattice structures, indicating that optimized arrangement in the hybrid lattice structure may render superior mechanical property.

FEM analysis was carried out to quantify and visibly estimate the mechanical behavior of the lattice structures. The Mises stress distributions of 8 unit cells located at the center of lattice models with the nominal strain of 1% are illustrated in **Fig. 5-12**. The struts in the unit cells of BCC lattice structure exhibited non-uniform stress distribution, where high stress was concentrated near the node region and the low stress was distributed at the central region of strut. This is in accordance with the result in **Fig. 2-14 (a)** in Chapter 2. The FCC lattice structure displayed relatively uniform high stress distribution, thus resulting in higher strength compared to the BCC lattice structure. In the case of Parallel hybrid 1 and 2 lattice structures, the stress in BCC and FCC unit cells were not noticeably varied when comparing to that in the homogeneous BCC and FCC lattice structure. The two different unit cells did not significantly affect each other in the Parallel hybrid at the early compression. Differently, the BCC unit cells in Vertical hybrid exhibited less stress concentration around the node region, and the X-shaped outside struts in FCC unit cells showed increased stress. It is considered that the severely bended FCC struts were attributed to the high distributed stress (**Fig. 5-10**). It is found that the FCC unit cells in 3-dimensional hybrid lattice structure exhibited unique behavior with high stress located in

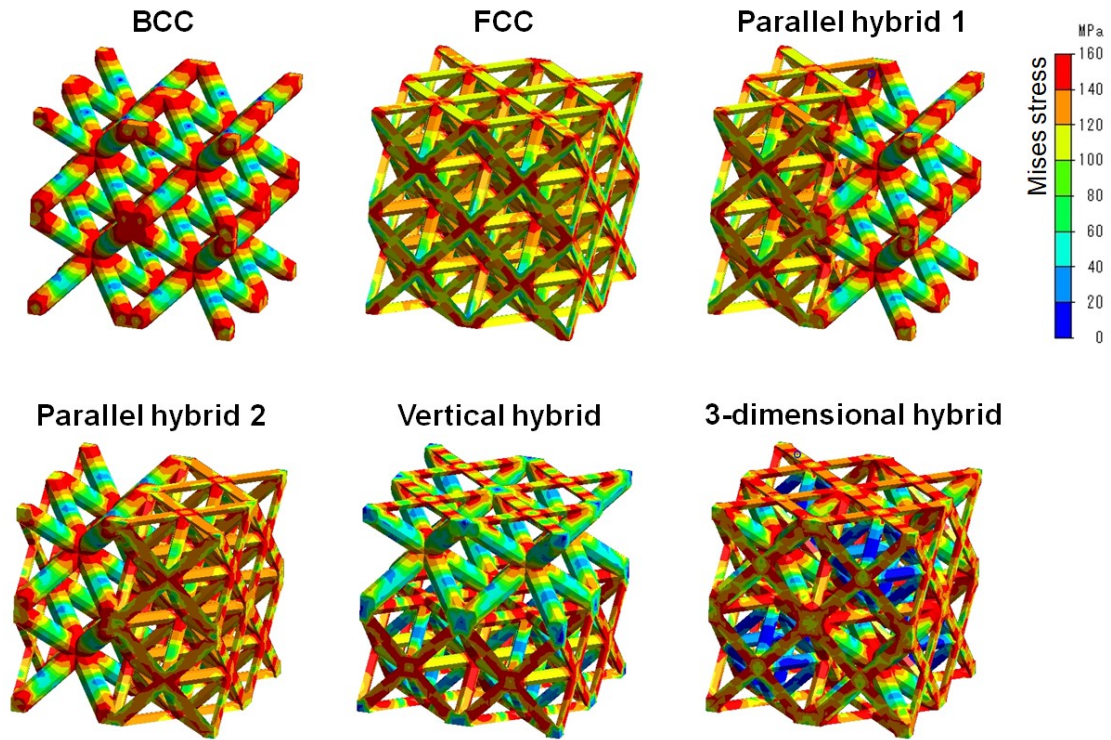


Fig. 5-12 Mises stress distribution of unit cells in lattice models at 1% compression strain.

X-shaped outside struts and extremely low stress distributed in the inside struts. At early compressive stage, the inside struts hardly contributed to the load-bearing of the hybrid lattice. After the outside struts collapsed and the node of FCC contacted its upper central node of BCC unit cells, the inside struts of FCC may start to carry high stress. This insight is thought to be the reason that the plateau stress of 3-dimensional hybrid increased slightly from 23.8% nominal strain (**Fig. 5-3**). It is noted that the result of increased stress during plateau derived from sequentially loaded struts is similar to the compressive behavior of C15 lattice structure with two plateau regions in Chapter 4. Furthermore, thickening the outside struts and pruning the inside struts of FCC unit cells in 3-dimensional hybrid may lead to the improvement of yield strength, and the converse may lead to the appearance of two plateau regions. The FCC unit cell with diameter adjustment on the outside and inside struts is analogous to the L_{12} crystal structure. The above deduction needs to be verified in the future through the compression experiments on the hybrid lattice structures composed of BCC and L_{12} -inspired unit cells.

It has been suggested that shear band occurred in lattice structure is triggered by the crack initiation and propagation at the tensile stressed regions in struts (**Fig. 3-7** in Chapter 3). To compare the tendency of shear band initiation in hybrid lattice structure from the point of view

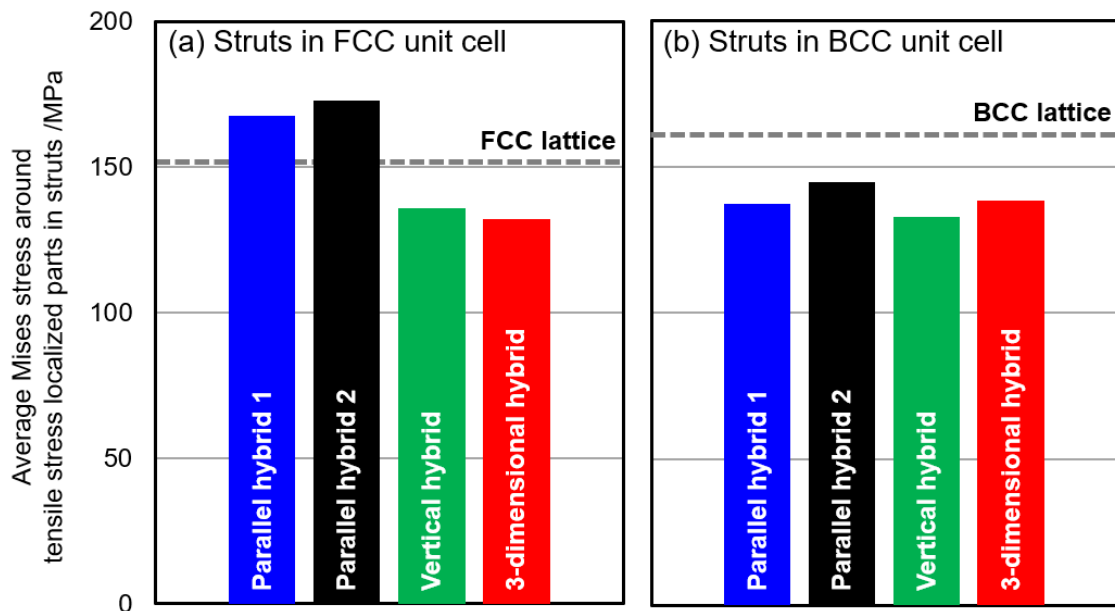


Fig. 5-13 Average Mises stress at the tensile stress localized parts in struts in (a) FCC and (b) BCC unit cell at 1% nominal strain of lattice structures.

of stress concentration, the average Mises stress around the tensile stress localized parts in struts (corresponding to the crack initiation region in the case of FCC, Parallel hybrid 1 and 2 lattice structures shown in **Figs. 5-7 (a), 5-8, 5-9**) in FCC and BCC unit cells at 1% nominal strain are plotted in **Fig. 5-13**. The FCC lattice structure exhibited higher average Mises stress around the tensile stress localized parts than the Vertical and 3-dimensional hybrids, but lower value than the Parallel hybrid lattice structures (**Fig. 5-13 (a)**). This result indicates that cracks related to shear band formation has higher tendency to generate in Parallel hybrid and lower tendency in Vertical and 3-dimensional hybrid, compared to the FCC lattice structure with actual occurrence of shear band. In fact, shear band formed in Parallel hybrids and did not form in Vertical and 3-dimensional hybrid lattice structures according to the X-ray CT observation. For the struts in BCC unit cell (**Fig. 5-13 (b)**), all the hybrid lattice structures have lower average Mises stress around the tensile stress localized parts, i.e. lower tendency for shear band formation than the BCC lattice structure, where the shear band did not occur. The shear band in BCC unit cells was actually not observed in the hybrid lattice structures except Parallel hybrid 2. The occurrence of shear band in Parallel hybrid 2 was driven by the shear behavior of FCC unit cells at large strain. As discussed above, shear band formation can be suppressed in hybrid lattice structures with appropriate arrangement pattern of different unit cells, as a result of reduced Mises stresses at tensile stressed regions.

5.4 Conclusions

In this chapter, the hybrid lattice structure composed of bending-dominated BCC and stretch-dominated FCC unit cells with four different arrangement patterns was designed and fabricated by L-PBF process. The mechanical properties, deformation behaviors, and energy absorption capacities of heterogeneous hybrids and homogeneous BCC and FCC lattice structures were investigated. Full and interrupted compression tests, X-ray CT scan, and FEM analysis were carried out. Based on the results, the following conclusions were drawn:

- (1) The spatial arrangement patterns of BCC and FCC unit cells in hybrid lattice structures significantly influenced the mechanical properties and deformation behavior.
- (2) The experimental yield strengths of all hybrid lattice structures exceeded the upper-bound of prediction value of the Voigt model. Traditional rule-of-mixture is not suitable for evaluating the mechanical properties of hybrid lattice structures.

- (3) Shear bands associated with stress drops were formed in Parallel hybrids rather than Vertical and 3-dimensional hybrid lattice structures, due to higher concentrated Mises stresses at tensile stressed regions in Parallel hybrids. The discontinuity of struts on the preferential shear band plane caused by the presence of different unit cell contributed to avoid shear band formation in hybrid lattice structures.
- (4) Appropriate arrangement pattern of different unit cells can achieve high plateau stress level without the stress loss by shear band formation. The 3-dimensional hybrid lattice structure with high level of mixture of BCC and FCC unit cells exhibited the highest energy capacity of $3.8 \text{ MJ}\cdot\text{m}^{-3}$.

References

- [1] M. Mirzaali, R. Hedayati, P. Vena, L. Vergani, M. Strano, A. Zadpoor, Rational design of soft mechanical metamaterials: independent tailoring of elastic properties with randomness, *Appl. Phys. Lett.* 111 (2017) 051903.
- [2] D. Kang, S. Park, Y. Son, S. Yeon, S.H. Kim, I. Kim, Multi-lattice inner structures for high-strength and light-weight in metal selective laser melting process, *Mater. Des.* 175 (2019) 107786.
- [3] A. Ingrole, A. Hao, R. Liang, Design and modeling of auxetic and hybrid honeycomb structures for in-plane property enhancement, *Mater. Des.* 117 (2017) 72–83.
- [4] R. Xue, X. Cui, P. Zhang, K. Liu, Y. Li, W. Wu, H. Liao, Mechanical design and energy absorption performances of novel dual scale hybrid plate-lattice mechanical metamaterials, *Extreme Mech. Lett.* 40 (2020) 100918.
- [5] H. Lei, C. Li, X. Zhang, P. Wang, H. Zhou, Z. Zhao, D. Fang, Deformation behavior of heterogeneous multi-morphology lattice core hybrid structures, *Addit. Manuf.* 37 (2021) 101674.
- [6] S. Li, M. Hu, L. Xiao, W. Song, Compressive properties and collapse behavior of additively-manufactured layered-hybrid lattice structures under static and dynamic loadings, *Thin-Walled Struct.* 157 (2020) 107153.
- [7] M.S. Pham, C. Liu, I. Todd, J. Lertthanasarn, Damage-tolerant architected materials inspired by crystal microstructure, *Nature* 565 (2019) 305–311.
- [8] W. Voigt, Über die beziehung zwischen den beiden elasticitätsconstanten isotroper körper,

Ann. Phys. 274 (12) (1889) 573–587.

- [9] A. Reuss, Berechnung der fließgrenze von mischkristallen auf grund der plastizitätsbedingung für einkristalle, *Z. Angew. Math. Mech.* 9 (1929) 49–58.
- [10] M. Kaur, S.M. Han, W.S. Kim, Three-dimensionally printed cellular architecture materials: perspectives on fabrication, material advances, and applications, *MRS Commun.* 7 (1) (2017) 8–19.
- [11] R. Alberdi, R. Dingreville, J. Robbins, T. Walsh, B.C. White, B. Jared, B. L. Boyce, Multi-morphology lattices lead to improved plastic energy absorption, *Mater. Des.* 194 (2020)108883.

6. Conclusions and future work

6.1 Conclusions

In the present study, the mechanical properties of additive-manufactured metallic lattice structures, which were fabricated by laser powder bed fusion using aluminum alloy powders, were investigated, and methods to enhance the mechanical performance of lattice structures were proposed and evaluated through experimental and numerical approaches. First, the AlSi10Mg lattice structures consisting of three different unit cell types were studied to elucidate the effect of geometrical features the static and high-speed compressive properties, including plateau stress, initial strain for densification, and deformation behavior. The energy absorption capacities of the three kinds of lattice structures were compared with reported lattice structures made of other metallic materials. The shear band formation often occurring in lattice structures, which prompts an unstable stress–strain response and reduced energy absorption capacity, was then focused on. The mechanism, evolution process and preferential formation planes and directions of shear band were explored. Also, an approach by adjusting strut diameter ratios to suppress the shear band formation was proposed on the basis of finite element analysis and demonstrated numerically. The improvement in the compressive performance of lattice structures was further attempted using novel design strategies. The mechanical responses of new lattice structures designed by mimicking topologically close-packed structure of C15 Laves phase were investigated. The deformation modes of C15 lattice structures were characterized using Gibson-Ashby equation. Finally, the hybrid lattice structure was proposed by combining bending-dominated BCC and stretch-dominated FCC unit cells. The effect of four spatial arrangement patterns of the two kinds of unit cells on the mechanical properties and deformation behavior of hybrid lattice structure were studied. The main conclusions in each chapter of the present thesis are summarized separately as follows.

In Chapter 1, the significance of enhancement in the mechanical properties of lattice structures for practical application were stated. The categorizations, designs, fabrication processes, and mechanical properties of lattice structures were detailed. The reported literatures were conducted for a better understanding of state-of-art researches and current issues of lattice structures. Accordingly, the purpose of the present study was proposed and main objectives have

been specified.

In Chapter 2, the effect of different unit cell morphology including body-centered cubic (BCC), truncated octahedron (TO) and hexagon (Hexa) on the mechanical properties and deformation behaviors of the AlSi10Mg lattice structures were elucidated. TO lattice structure exhibited higher yield strength and plateau stress than the BCC and Hexa lattice structures. Shear band formation occurred in BCC and TO lattice structures during compression, resulting in the fluctuation of stress–strain curves. Continuous deformation behavior was observed in Hexa lattice structure without cracking of struts, which could be attributed to the low distributed Mises stress at tensile stress parts quantified by FEM analysis. Hexa lattice structure exhibited small initial strain for densification. A large number of struts in compression direction led to the struts overlapping and early densification. The TO lattice structure exhibited superior energy absorption capacity reaching the level of previously reported titanium alloy lattice structures. In addition, the results of high-speed indentation tests indicated that the practical energy absorption properties of TO and Hexa lattice structures can be estimated by static indentation tests.

In Chapter 3, the formation mechanism and process of shear band based on BCC lattice structure were clarified. It has been suggested that the shear band was triggered by the crack initiation and propagation at the tensile stressed regions in struts. Shear bands were preferentially formed on the densest plane including the most struts when the loading axis was not parallel or perpendicular to this plane. The family of shear bands in BCC and FCC (octet-truss) lattice structure were in accordance with the slip system of the corresponding crystal lattices. Through the method by adjusting strut diameter ratios, the localized tensile stress in struts can be relieved according to the FEM, suggesting a low tendency of shear band formation. The effectiveness of this shear band suppression approach was demonstrated by the experimental results. The compressive strength and energy absorption capacity of the BCC lattice structures were substantially enhanced by optimized strut shape.

In Chapter 4, the lattice structures with a new configuration of C15 unit cell inspired by topologically close-packed structure of C15 Laves phase were established, on the basis of the consideration that the node and strut in lattice structure are analogous to the atom and atomic

bond in crystal structure. The C15 lattice structures with various relative densities exhibited two plateau regions with graded stress level, enabling the structure to absorb high energy of $5.0 \text{ MJ} \cdot \text{m}^{-3}$. The two plateau regions in C15 lattice structures were attributed to the two different units of crisscross and deltahedron with graded relative density. Crisscross units preferentially exhibited a bending-dominated deformation behavior in 1st plateau, and subsequently deltahedron units exhibited a stretch-dominated deformation behavior in 2nd plateau, suggesting the hybrid deformation mode of C15 lattice structures.

In Chapter 5, the hybrid lattice structure composed of differently arranged BCC and FCC unit cells were examined with comparison to homogeneous BCC and FCC lattice structures. The spatial arrangement patterns of BCC and FCC unit cells in hybrid lattice structures significantly influenced the mechanical properties and deformation behavior. The experimental yield strengths of all the hybrid lattice structures exceeded the upper-bound of prediction value of the Voigt model. Shear bands associated with stress drops appeared in Parallel hybrids, due to higher concentrated Mises stress at tensile stressed parts. The discontinuity of struts on the preferential shear band plane caused by the presence of different unit cell contributed to avoid shear band formation in Vertical and 3-dimensional hybrid lattice structures. Therefore, appropriate arrangement pattern of different unit cells can achieve high plateau stress level without the stress loss by shear band formation, indicating high energy absorption capacity.

6.2 Future work

The changes in energy absorption capacities as a function of bulk density of all the aluminum alloy lattice structures investigated in the present study are plotted in **Fig. 6-1**. A continuous improvement in energy absorption capacity (approximate one order of magnitude in the case of the lattice structures with close relative density) is achieved by the proposed design strategies in Chapter 2 to 5. The strut shape optimizing in Chapter 3 leads to significant enhancement in low capacity of BCC lattice structures. The novel C15 lattice structures in Chapter 4 designed on the basis of the analogy with crystal structure further extend the level of energy absorption capacity. The hybrid deformation mode of C15 lattice structures attributed to the two different units opens up new opportunity for performance improvement using hybrids. The BCC lattice structure hybridized by FCC unit cells with various arrangement patterns,

indicating hybrid lattice structure in Chapter 5, has demonstrated obvious capacity enhancement. The unit cell types exhibit remarkable effect on the performance of lattice structure, as fact that the TO lattice structure shows the highest energy absorption capacity in this study compared to the lattice structures with other unit cell types. The applicability of strut shape optimization and hybrid approaches to various lattice structures implies potential mechanical improvement of TO or other high-performance lattice structures, which should be demonstrated in the future work to extend the boundary of used materials.

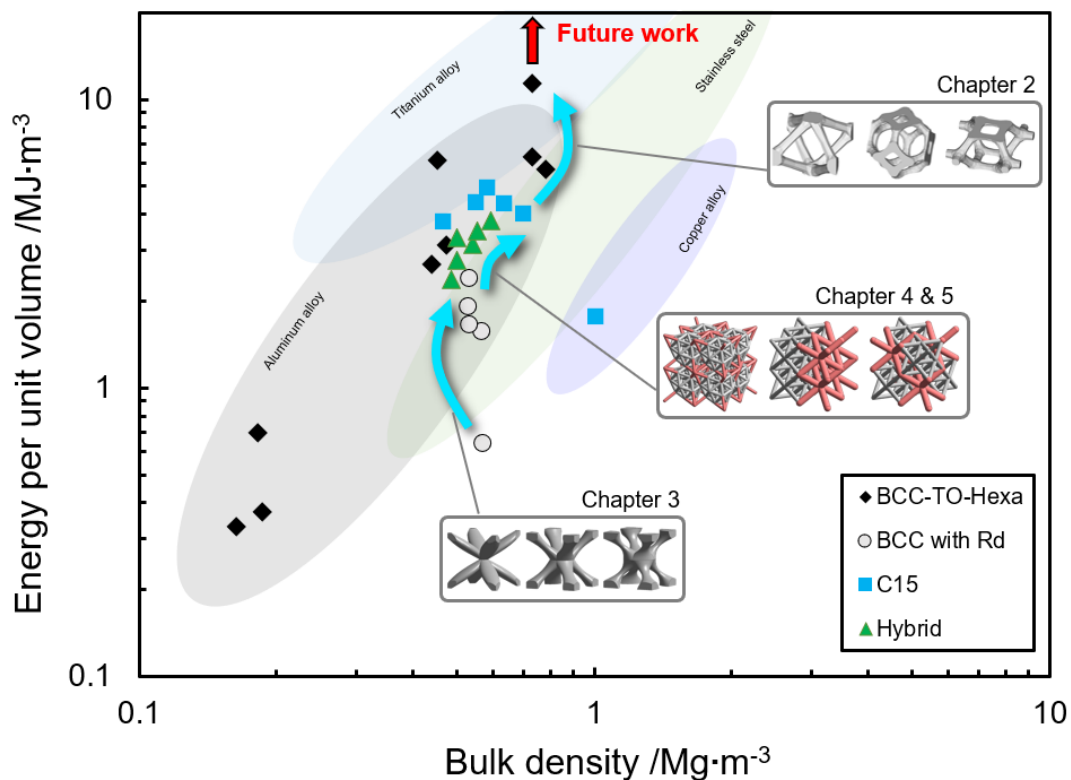


Fig. 6-1. The changes in energy absorption capacities as a function of bulk density of all the aluminum alloy lattice structures investigated in the present study.

By integrating the presented approaches, a multi-scale lattice design strategy is put forward to take advantage of functionality and performance of lattice structures, as shown in **Fig. 6-2**. In the strut scale, the shape optimization contributes to both the strengthening and suppressing of shear band formations. Adequate existing unit cells and those to be discovered offer the possibilities to render high energy absorption, for lattice structures designed in unit cell scale. The lattice structures with tailored arrangement and distributions of unit cells, relative densities,

orientations, and mixture ratios can exhibit novel compressive behavior, such as C15 lattice structure with characteristic features of two plateau regions and hybrid deformation mode. The integration of multi-scale design strategies as future prospects and potential extension of the current research, gives rise to the opportunities to maximize the mechanical properties and broaden the functionalities of lattice structures.

Multi-scale Lattice Design

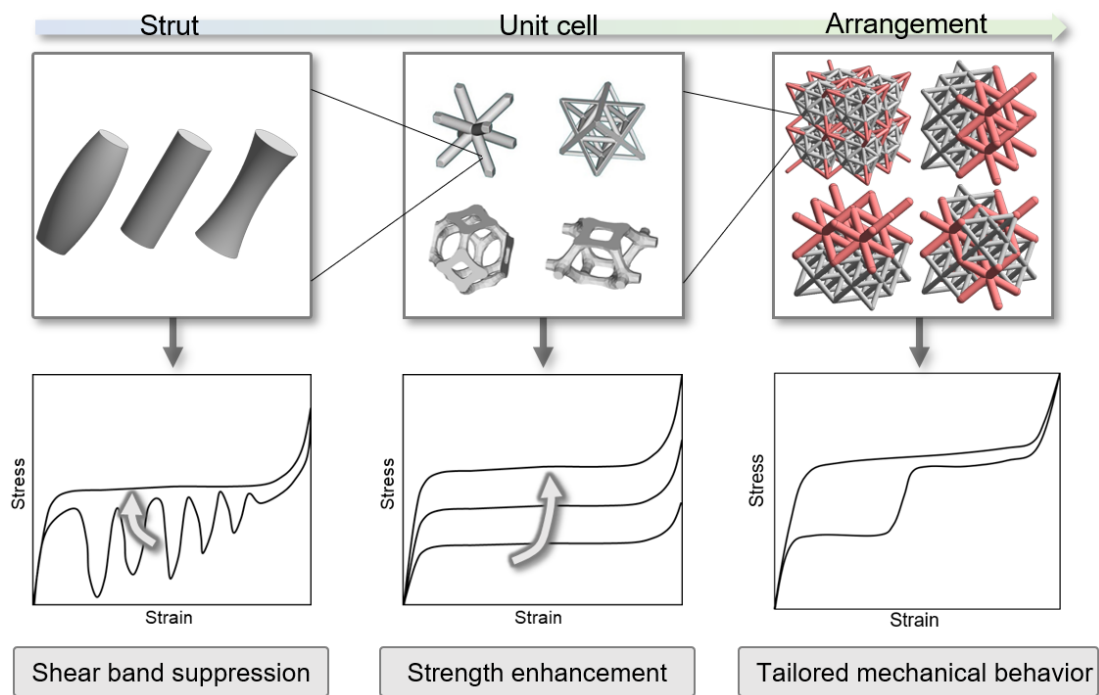


Fig. 6-2. The multi-scale lattice design integrated on the basis of studied approaches.

Published journal papers

1. Liu, X., Suzuki, A., Takata, N., Kobashi, M., Kato, M. Dual plateau stress of C15-type topologically close-packed lattice structures additive-manufactured by laser powder bed fusion. *Scripta Materialia* 202 (2021) 114003.
2. Liu, X., Wada, T., Suzuki, A., Takata, N., Kobashi, M., Kato, M. Understanding and suppressing shear band formation in strut-based lattice structures manufactured by laser powder bed fusion. *Materials & Design* 199 (2021) 109416.
3. Liu, X., Sekizawa, K., Suzuki, A., Takata, N., Kobashi, M., Yamada, T. Compressive properties of Al-Si alloy lattice structures with three different unit cells fabricated via laser powder bed fusion. *Materials* 13(13) (2020) 2902.

Acknowledgements

This doctoral study was conducted within three years in Department of Materials Process Engineering, Graduate School of Engineering, Nagoya University, under the supervision of Prof. Kobashi Makoto. During this period, I have been fortunate to be supported and inspired by many people. They provide constant support, encouragement and goodwill, without whom this work would have never been possible. To all of them, I would like to express my most sincere gratitude and appreciation.

First and foremost, I would like to express my heartfelt acknowledgement to Prof. Kobashi Makoto for offering me the opportunity to do this research, for his support, guidance and recommendations, and for his trust in me right from the beginning. I would like to sincerely thank Prof. Suzuki Asuka for the time and effort he devoted to supervising and strongly supporting me. All the insightful suggestions, fruitful discussions, and patience from Prof. Kobashi Makoto and Prof. Suzuki Asuka are extremely grateful. My sincere thanks also go to Prof. Takata Naoki for the constructive suggestions about this study and journal papers. I would like to sincerely acknowledge the jury members of the thesis defense committee, Prof. Kato Junji and Prof. Yukawa Nobuki for the extensive review of the manuscript. I would like to acknowledge Prof. Hoshiba Hiroya for the collaborative work. I am deeply grateful to Dr. Kato Masaki, Mr. Wada Takafumi, Mr. Sekizawa Keito for their valuable contributions to published journal papers.

My deep thanks are also due the members in this group, their friendships, assistance and encouragement helped me go through my study and life. I greatly appreciate all my friends in China and met in Japan, who encouraged and supported me all the times.

I wish to acknowledge the financial support for my daily life from the China Scholarship Council (No. 201908050220).

Last but not least, I would like to express my appreciation to my parents and sisters for their unconditional love and commitment they have always shown towards me; to my girlfriend Li Yamei for always standing by me, believing in me and loving me.